Plasmon Waveguiding in Nanowires

Hong Wei,[†] Deng Pan,[‡] Shunping Zhang,[‡] Zhipeng Li,[§] Qiang Li,[‖] Ning Liu,[⊥] Wenhui Wang,[∇] and Hongxing Xu*,[‡,#]

[†]Institute of Physics, Chinese Academy of Sciences, Beijing 100190, China

[‡]School of Physics and Technology, and Key Laboratory of Artificial Micro- and Nano-structures of Ministry of Education, Wuhan University, Wuhan 430072, China

[§]Beijing Key Laboratory of Nano-Photonics and Nano-Structure (NPNS), Department of Physics, Capital Normal University, Beijing 100048, China
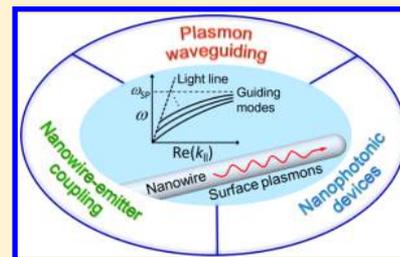
[‖]Guangdong Provincial Key Laboratory of Nanophotonic Functional Materials and Devices, School of Information and Optoelectronic Science and Engineering, South China Normal University, Guangzhou 510006, China

[⊥]Department of Physics and Bernal Institute, University of Limerick, Limerick, Ireland

[∇]School of Science, Xi'an Jiaotong University, Xi'an 710049, China

[#]Institute for Advanced Studies, Wuhan University, Wuhan 430072, China

ABSTRACT: Nanowires supporting propagating surface plasmons can function as nanowaveguides to realize the light guiding with field confinement beyond the diffraction limit, providing fundamental building blocks for nanophotonic integrated circuits. This review covers the recent developments of plasmon waveguiding in nanowires, mainly including plasmon waveguiding in metal nanowires, coupling of nanowire plasmons and emitters, hybrid nanowire waveguides and plasmonic gain, and nanowire photonic devices. We first introduce the main techniques for fabricating metal nanowires, the plasmon modes in metal nanowires and the excitation/detection methods. We then discuss the fundamental properties of plasmon propagation and emission, including zigzag, chiral and spin-dependent propagation, mode conversion, loss and propagation length, group velocity, terminal emission, and leaky radiation. Then the interactions between nanowires and emitters are reviewed, especially the coupling of single nanowires and single quantum emitters. Finally, we briefly introduce the hybrid nanowire waveguide composed of a semiconductor nanowire and a metal film with an intervening thin insulator and highlight a few nanophotonic devices based on plasmonic nanowire networks or plasmonic-photonic hybrid nanowire structures.

CONTENTS

1. INTRODUCTION

Light waveguiding in optical fibers lays the foundation for modern optical communications. Applying light for optical information processing in on-chip integrated photonic circuits requires that the confinement of light is higher than that in optical fibers. This means decreasing the size of the waveguide down to the subwavelength scale. The diffraction limit of light sets the restriction for the size of dielectric waveguides. Fortunately, metal nanostructures can support surface plasmons (SPs), collective oscillations of free electrons at the metal-dielectric interface, which can confine light far beyond the diffraction limit. When light couples to metal nanostructures, due to the excitation of SPs, the free-space light can be transformed to optical modes confined at the metal surface. Because of the ability of SPs to confine light into subwavelength spatial dimensions, as well as their large bandwidth (thus high speed) for processing and transmitting information, plasmonics is regarded as one of the most promising candidates for next generation information and communication technology.[1,2] Plasmonic devices and components can either be used as building blocks to realize all-optical integrated photonic chips, or they can be integrated with the silicon electronics in a compatible manner to solve some critical issues in current computer architectures, such as high speed interconnects at both inter- and intrachip level.

Depending on the dimensions of the confinement, the SPs are classified as localized SPs and propagating SPs (the latter is also usually called surface plasmon polaritons; for simplicity, we use SPs or plasmons in this review).[3] In metal films, and metal−insulator−metal or insulator−metal−insulator sandwiched films, propagating SPs can be supported at the metal-dielectric interfaces. For better directing the light propagation with higher field confinement, one-dimensional (1D) waveguide structures are desired. There are multiple 1D plasmonic waveguides, for example, metal nanowires (NWs),[4−8] metal stripes,[9,10] grooves or slots in metal films,[11−13] dielectric NWs on metal films,[14,15] etc. Metal NWs attract much interest for their particular optical properties due to the excitation of SPs. The light can be coupled into metal NWs as propagating SPs

with the electric field tightly confined at the metal surface. The materials of plasmonic NWs are mainly silver and gold. Ag NWs are preferred as plasmonic waveguides due to their better performances determined by the dielectric constant of Ag. A metal NW can support multiple SP modes with different propagation constants and polarization characteristics, and these modes can be excited by light of different polarizations. The excitation of multiple modes and the control of these modes lead to the extraordinary properties of the propagating SPs. On the basis of the control of SP propagation, different nanophotonic functionalities can be realized, for example, plasmonic routers[16] and logic gates.[17,18]

The field confinement and waveguiding properties of metal NWs make their coupling with quantum emitters attractive. The enhanced electric field and local density of states (LDOS) on the NW can strongly alter the excitation and emission of nearby emitters. The coupling of single quantum emitters with metal NWs can generate single quantized SPs.[19−21] This coupling system can be explored for single photon and single plasmon nanophotonic devices, which may be integrated into quantum nanophotonic circuitry. The coupling of metal NWs with gain materials may be used to compensate for the loss of plasmons during propagation to keep the signal strength. Aiming for decreased SP propagation loss, a hybrid NW waveguide was proposed, which is composed of a dielectric NW over a metal film with a low-refractive-index spacer between them.[15] By employing gain material for the NW, the SP loss can be fully compensated.[22]

In this review, we mainly summarize the developments of plasmon waveguiding in silver and gold NWs, and the interactions of NW plasmons and quantum emitters. The hybrid NW waveguides are also concisely discussed. We start with a brief introduction to the approaches for fabricating metal NWs in section 2, followed by the discussions on the plasmon modes in metal NWs in section 3. In section 4, we introduce the methods for exciting and detecting SPs, including both optical and electrical methods. Section 5 covers the fundamental properties of SP propagation and emission, including zigzag, chiral and spin-dependent propagation, mode conversion, loss and propagation length, group velocity, terminal emission, and leaky radiation. Section 6 is focused on the coupling between metal NWs and emitters. Both the coupling between NWs and emitter films and the coupling of a single NW and a single emitter are discussed. The NW plasmon-assisted entanglement and energy transfer and remote excitation/detection are introduced at the end of this section. In section 7, we briefly discuss hybrid NW waveguides and plasmonic gain in this system. In section 8, we highlight a few nanophotonic devices realized on the basis of propagating SPs in metal NWs and hybrid structures of metal NWs and photonic NWs. Finally, we conclude this review and give perspectives on the future development of this field.

2. METHODS FOR FABRICATING METAL NANOWIRES

Metal NWs can be prepared by both bottom-up and top-down approaches. Ag NWs can be conveniently synthesized by using a polyol process with ethylene glycol (EG) serving as both solvent and reducing agent and poly(vinylpyrrolidone) (PVP) as the coordination reagent.[23] In a typical synthesis process, an EG solution of silver nitrate and an EG solution of PVP were injected into preheated EG refluxed at 160 °C. After injection, the reaction mixture was kept at 160 °C for about 60 min. Magnetic stirring was continuously applied throughout the
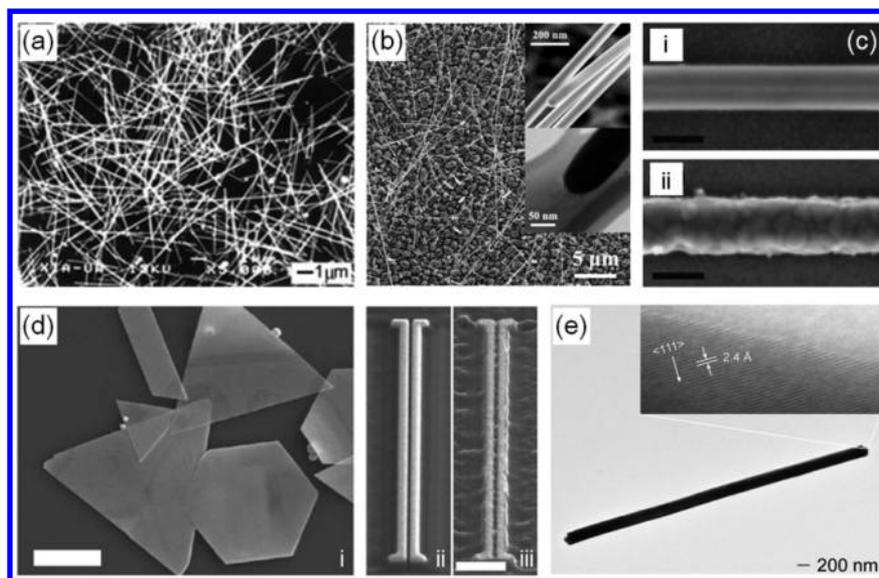
Figure 1. Silver and gold NWs produced by different methods. (a) SEM image of chemically synthesized Ag NWs. Reprinted with permission from ref 23. Copyright 2002 Wiley. (b) SEM and TEM images of Ag NWs by vapor-phase synthesis. Reprinted from ref 27. Copyright 2007 American Chemical Society. (c) SEM images of a chemically synthesized Ag NW (top) and an EBL fabricated Ag NW (bottom). The scale bars are 100 nm. Reprinted from ref 29. Copyright 2012 American Chemical Society. (d) SEM images of gold microplates (i), and gold NWs by FIB milling of a chemically synthesized microplate (ii) and deposited metal film (iii). The scale bars in (i) and (iii) are 5 μm and 500 nm, respectively. Reprinted with permission from ref 30. Copyright 2010 Nature Publishing Group. (e) TEM images of a gold NW cut from a gold microplate by nanoskiving. Reprinted from ref 32. Copyright 2008 American Chemical Society.

entire process of the chemical reaction and NW growth. The yield, diameter, and aspect ratio of the NWs could be tuned by tuning the experimental parameters, such as the molecular weight of PVP and the molar ratio of its repeating unit relative to silver nitrate, temperature, injection rates, and reaction time. Figure 1a shows the scanning electron microscope (SEM) image of Ag NWs obtained in a typical synthesis. The chemically synthesized Ag NWs have a pentagonal shape of the cross sections.[24] These NWs are bicrystals with the {111} twin planes parallel to the longitudinal axes of the NWs, and each half divided by the twin plane in a NW is single-crystalline. Gold NWs can be obtained by the solution-phase synthesis as well.[25,26]

Ag NWs can also be prepared by vapor-phase synthesis, in which only a single reactant, Ag_2O, is used. The Ag_2O powder was placed in an alumina boat in a quartz tube furnace.[27] By heating the Ag_2O powder, the precursor vapor was carried downstream by a flow of Ar to a low temperature zone, where Ag NWs were grown on a silicon substrate. Figure 1b shows the SEM and transmission electron microscope (TEM) images of Ag NWs generated by this method. As can be seen from the insets, the NWs have clean surfaces and diameters of 80−150 nm. Further experimental characterization reveals that the Ag NWs are single-crystalline with round cross sections. The epitaxial growth of gold NWs was reported,[28] with the gold NWs growing vertically or horizontally depending on the atom flux.

Chemical synthesis can produce silver and gold NWs of monocrystalline structures with smooth surfaces, but it is hard to precisely control the geometry of the NWs. Lithography based top-down methods, such as electron beam lithography (EBL) and focused ion beam (FIB) milling can fabricate metal NWs of designed dimensions at well-defined positions. However, the metal film deposition results in NWs of polycrystals with rough surfaces, which largely increase the

scattering loss of propagating SPs. Moreover, in the standard fabrication process, an adhesive layer of metal, such as Cr, introduced between the silver or gold and the substrate to increase the adhesion of the metal to the substrate surface, introduces additional plasmon loss. Figure 1c shows SEM images of a chemically synthesized Ag NW and an EBL fabricated Ag NW.[29] The grains and rough surface of the latter can be seen clearly.

By combining bottom-up and top-down methods, single-crystalline metal NWs with smooth surfaces and well-defined geometries can be fabricated. By synthesizing metal microplates first (Figure 1d, i) and using FIB milling, smooth metal NWs can be obtained.[30,31] The NWs etched on chemically synthesized metal microplates have much smoother surfaces compared with the NWs etched on the vapor-deposited metal films, as shown in Figure 1d, ii, iii. Metal NWs can also be fabricated out of chemically synthesized microplates by nanoskiving. Figure 1e shows TEM images of a gold NW obtained by nanoskiving.[32] The inset shows defect-free (111) lattice fringes at the edge of the NW, indicating that the NW maintains the crystalline structure of the microplate.

Metal NWs can also be prepared by using templates, for example, porous anodized aluminum oxide templates and polycarbonate membrane templates.[33−35] The dimensions of the NWs are determined by the templates. The NWs obtained by these methods are usually polycrystalline structures. Studies have shown that the crystallinity strongly influences the waveguiding properties of the metal NWs, and polycrystalline NWs suffer larger propagation loss.[29,36,37] In most experimental studies of plasmon waveguiding, chemically synthesized Ag NWs are used.

3. PLASMON MODES IN METAL NANOWIRES

3.1. General Properties of Plasmon Modes in Metal Nanowires

A metal NW is a kind of quasi-one-dimensional structure with translational symmetry, which can serve as a waveguide with subwavelength confinement of light, as schematically shown in Figure 2a. In this section, we discuss the general properties of
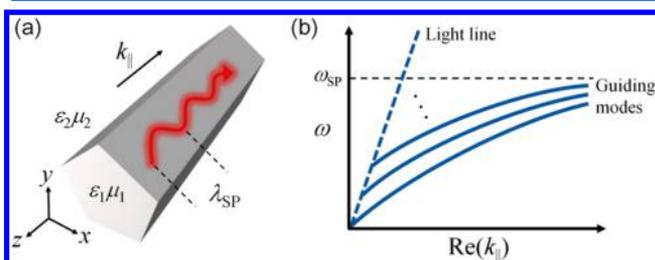
Figure 2. (a) Schematic of SPs propagating on a metal NW (a pentagonal NW as an example). (b) Illustration of the dispersion relations of different order SP modes in a metal NW.

plasmon modes in metal NWs, which are the bases of the various phenomena and versatile applications shown in the following sections.

Due to the translational symmetry of the NW, the electric field distributions of the guiding modes in the NW structures can be expressed as $\mathbf{E}(\mathbf{r}) = \mathbf{E}(x,y)e^{i(k_\parallel z - \omega t)}$, and the governing Helmholtz equation can be simplified as a two-dimensional problem

$$\nabla_\perp^2 \mathbf{E}(x, y) = (k^2 - k_\parallel^2)\mathbf{E}(x, y) \qquad (1)$$

where $\nabla_\perp^2$ is the two-dimensional Laplace operator in the traverse plane, $k_\parallel$ is the wave vector parallel with the NW of the mode, and k is defined by $k_i^2 = \varepsilon_i\mu_i k_0^2$ in respective regions (ε_i and μ_i are the permittivity and permeability of the materials, respectively, and k_0 is the wave vector in vacuum). The corresponding transverse wave vectors can be obtained by $k_{\perp,i}^2 = k_i^2 - k_\parallel^2$. The guiding plasmon wave is illustrated by a pentagonal NW in a homogeneous medium in Figure 2a, where $i = 1$ and 2 label the metal core region and the dielectric cladding region, respectively. The guiding plasmon eigenmodes of this NW are defined by the eigenfunctions of eq 1 with imaginary transverse wave vectors $k_{\perp,i}$ in both the core ($i = 1$) and cladding ($i = 2$) regions [i.e., $k_{\perp,i}^2 = (k_i^2 - k_\parallel^2) < 0$], which indicates that the fields decay exponentially on both sides of the metal-dielectric interface. However, it is also possible that the propagation constant $\mathrm{Re}(k_\parallel)$ of the plasmon mode is smaller than the wave vector of light in some part of the cladding. For example, the plasmon mode for a NW deposited on a substrate with a refractive index n_s, as will be discussed in sections 3.2.2 and 5.8, might have a propagation constant $\mathrm{Re}(k_\parallel)$ smaller than $\mathrm{Re}(n_s k_0)$, so that the field in the substrate is not an evanescent wave. This extending wave in the cladding causes the leakage of energy from the plasmon mode, and this kind of leaky plasmon mode suffers damping during propagation, even when ignoring the material loss. For an ordinary dielectric waveguide, the transverse wave vector inside the core region is real (i.e., $k_{\perp,1}^2 = (k_1^2 - k_\parallel^2) > 0$, where k_1 is the wave vector in the core of the dielectric NW), and the field is an extending wave in the transverse plane. The width of the extending wave inside the core is therefore constrained by the diffraction limit, which indicates that simply shrinking the diameter of the dielectric

waveguide cannot increase the mode confinement but only leads to more power extending widely outside the core region. This constraint does not hold for a metal NW, since the plasmon modes are evanescent waves on both sides of the metal−dielectric interface. As a result, the fields of plasmon modes are squeezed near the surface of the metal NW. The plasmon field highly confined near the surface accounts for the strong light-matter interaction, as shown by the applications of NW-emitter coupling and plasmonic gain, discussed in sections 6 and 7.

A thick NW can support several modes of different orders, with the symmetry of the mode distributions determined by the geometrical symmetry of the NW. Since most NWs have mirror symmetry (e.g., in the x direction as shown in Figure 2a), the plasmon modes are symmetric or antisymmetric in this direction. The superposition of these plasmon modes with different symmetry shows a zigzag propagation route, leading to applications in plasmon routers and logic gates, as will be discussed in sections 5.1 and 8. The real part of the wave vector parallel with the NW $k_\parallel$ is determined by the wavelength of the plasmon modes $\mathrm{Re}(k_\parallel) = 2\pi/\lambda_{\mathrm{SP}}$. An effective refractive index can be defined for the eigenmode as $n_{\mathrm{eff}} = \mathrm{Re}(k_\parallel)/k_0$ using the wave vector in vacuum k_0. Like the refractive index of a medium, n_{eff} also describes the decrease of the wavelength, $n_{\mathrm{eff}} = \lambda_0/\lambda_{\mathrm{SP}}$, when photons enter the waveguide from the vacuum. The effective refractive indices n_{eff} and wave vectors $k_\parallel$ of the plasmon modes vary for different frequencies. Their dependence on frequency is described as the dispersion relations, as schematically illustrated in Figure 2b. The universal trade-off between confinement and loss of SPs indicates that the effective refractive indices also correlate with field distributions of the modes—larger n_{eff} corresponds to higher confinement with more fields distributed inside the metal region, while this field concentration in the metal leads to a higher ohmic loss.[38]

The dispersion of the guiding modes includes the contribution of the material dispersion of the metal and the waveguide dispersion resulting from geometry constraints. These two kinds of dispersion mechanisms can be understood from eq 1: the eigenvalue problem and $k_\parallel$ are determined by the distribution of material and the cross-sectional geometry of the NW. The latter factor contributes to the waveguide dispersion, which implies that the larger the wavelength is, the more the mode field spreads from the core into the cladding. For thicker NWs, multiple modes can be supported, and their dispersion relations are schematically shown in Figure 2b. For all plasmon modes in a NW, when the frequency approaches the plasmon resonance frequency ω_{SP}, the dispersion is dominated by the metal material and plasmon resonance behavior. While for lower frequencies, only the lowest and second-order modes show no theoretical cutoff threshold.[39] For metal NWs with radii ranging from about 50 to 100 nm, both of the two modes are important and their superposition leads to various propagation behaviors and phenomena.

The dispersion relations also reflect the phase velocity and group velocity of the plasmon modes. The phase velocity corresponds to the speed of the phase front and is equal to c/n_{eff}, while the group velocity corresponds to the speed of a pulse formed by light over a range of frequencies, with the constructive interference located at the center of the pulse. The group velocity is thereby determined by the differential of the frequency components as $d\omega/d\mathrm{Re}(k_\parallel)$, which corresponds to the tangents of the dispersion curves in Figure 2b. The group velocities of all plasmon guiding modes are smaller than c and

decrease sharply when the frequency approaches the plasmon resonance frequency. The details of the group velocity of plasmons on NWs and the experimental results will be discussed in section 5.6.

3.2. Plasmon Modes in Cylindrical Nanowires

3.2.1. Cylindrical Nanowires in a Homogeneous Medium.
Although most experimentally prepared metal NWs are pentagonal or rectangular, a cylinder is the simplest geometry to effectively illustrate the general properties of plasmon modes in the NW and describes the phenomena observed for other geometries. Here we use a cylindrical NW to explain the general behavior of SPs on metal NWs, and NWs with different cross sections are discussed in section 3.3.

The electric field distribution of the modes in a cylindrical NW can be expressed as $\mathbf{E}(x,y,z) = \mathbf{E}(r)e^{im\varphi+ik_\parallel z}$, where r is the distance to the center of the NW $r = \sqrt{x^2 + y^2}$; $\mathbf{E}(r)$ is the radial distribution, decaying in both metal and dielectric regions expressed by modified Bessel functions; $e^{im\varphi}$ is the angular distribution, which corresponds to a helical wavefront considering the total phase distribution $e^{im\varphi+ik_\parallel z}$, and the handedness is determined by the sign of m. Except the fundamental mode ($m = 0$), higher-order plasmon modes are doubly degenerate ($m = \pm 1, \pm 2, ...$) with different handedness. In this expression, the angular term $e^{im\varphi}$ only introduces a phase distribution, and the field amplitude of the mode is cylindrically symmetric. It is also possible to recombine the two degenerate modes in new representations with angular terms expressed by $\cos(m\varphi)$ and $\sin(m\varphi)$, where the field amplitude is not cylindrically symmetric but shows mirror symmetry. As an example, the bottom panel of Figure 3a shows one of the two degenerate second-order modes, which are the recombinations of $m = \pm 1$ modes. The representations by trigonometric functions provide a more intuitive picture of specific collective oscillations of electrons, and we use this form in the following discussions.

Figure 3 (panels a–c) clearly shows a complete depiction of the two lowest-order plasmon modes in a cylindrical metal NW, including the distributions of field amplitude, field polarization, and surface charges. Different from the dielectric fiber, the fundamental plasmon mode ($m = 0$) in the metal NW is a transverse magnetic mode (denoted as TM_0) with the field polarized radially (upper panel of Figure 3a). For NWs with small radii, the TM_0 mode can be viewed as a chain of oscillating dipoles oriented along the NW with relative phase delays (upper panel of Figure 3b). This plasmon mode is a transverse magnetic mode because the instant current is always along the NW and the induced magnetic fields are perpendicular to the NW. The second-order modes of a cylindrical NW are hybrid modes of HE type (denoted as HE_1) and are doubly degenerate, which can be regarded as a chain of dipoles oriented perpendicular to the NW (lower panel of Figure 3b). As seen in the field distribution shown in the lower panel of Figure 3a, the polarization of the HE_1 mode is aligned nearly in the same direction and its field is distributed separately accumulating on the two sides of the NW. As the experimentally observable quantity is the field intensity, the field amplitudes of the TM_0 mode and HE_1 mode are plotted in Figure 3c, where the TM_0 mode produces a uniform distribution while the HE_1 mode distributes separately on two sides of the NW. This difference of field distributions between the TM_0 mode and HE_1 mode can be experimentally observed in the quantum dot (QD) fluorescence images shown
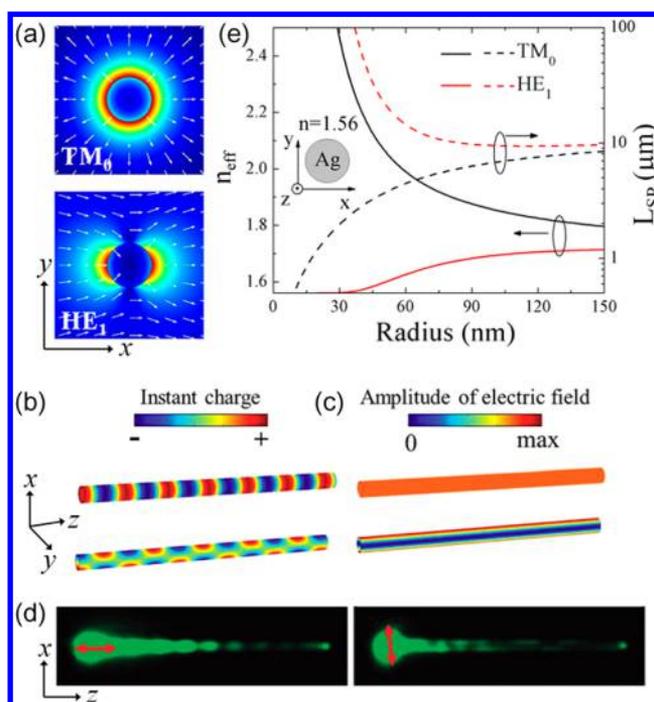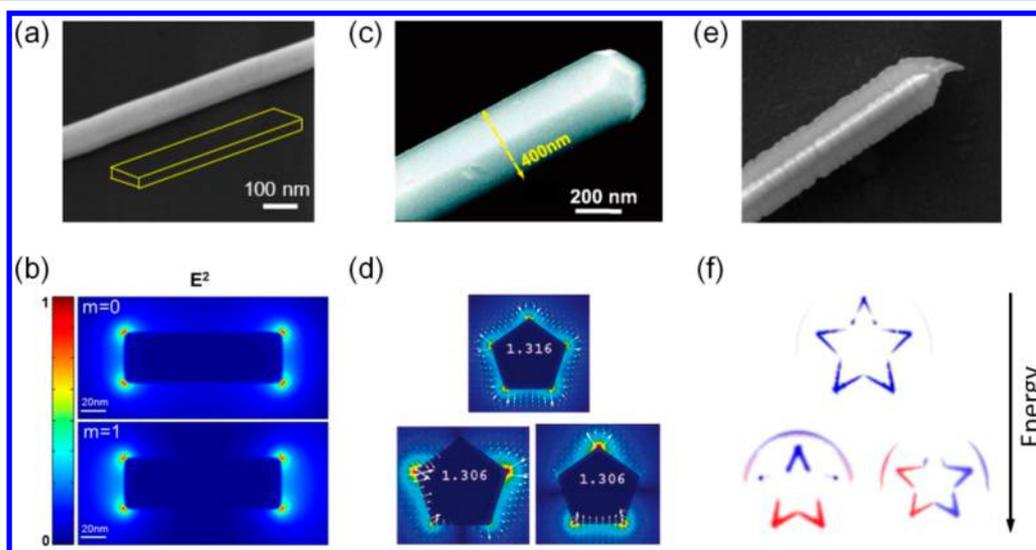

Figure 3. (a) Electric field distributions of TM_0 and HE_1 modes in a cylindrical Ag NW. The arrows denote the instant directions of the electric field in the transverse plane. (b and c) Distributions of (b) instant surface charges and (c) electric field amplitude of plasmons on a cylindrical Ag NW, for input with TM_0 (upper) and HE_1 (lower) modes. (d) QD fluorescence images of plasmons on a Ag NW excited by laser light with polarizations shown as red arrows. (e) Effective refractive indices and propagation lengths of the TM_0 and HE_1 modes as a function of the NW radius. The wavelength is 633 nm. (a and e) Reprinted with permission from ref 40. Copyright 2014 Nature Publishing Group. (b and c) Reprinted with permission from ref 41. Copyright 2014 Royal Society of Chemistry. (d) Reprinted from ref 17. Copyright 2011 American Chemical Society.

in Figure 3d, where the TM_0 mode and HE_1 mode are selectively excited by laser beams with linear polarization parallel (left panel) and perpendicular (right panel) to the NW, respectively (see discussion in section 4.1). Although the NW in the experiment is deposited on a glass substrate without a uniform environment as in the simulations, the main features of the plasmon modes are retained due to the mirror symmetry in the x direction, as will be discussed in section 3.2.2.

Figure 3e shows the dependence of the effective refractive indices n_{eff} of TM_0 and HE_1 modes on the NW radius, which agrees with our general discussion in section 3.1. For large radii, the n_{eff} of both of the two plasmon modes approach the value of the plasmons on a flat metal surface because the small curvature of the NW surface makes it resemble a flat surface. For small radii, n_{eff} of HE_1 mode decreases and nearly reaches the refractive index of the medium, which implies this mode is almost nonconfined with the field expanding and evolving into linearly polarized waves in free space. In contrast, the n_{eff} of the TM_0 mode increases sharply, which indicates that this mode becomes highly confined. As an example of the limit, the TM_0 mode can survive in a carbon nanotube with an ultraconfined field and strong coupling with matter.[42,43] Figure 3e also shows the dependence of the propagation length, defined as the distance for the plasmon intensity to decay to $1/e$ of the initial intensity, on the NW radius. This result is in accordance with the general principle that a higher confinement of the plasmon
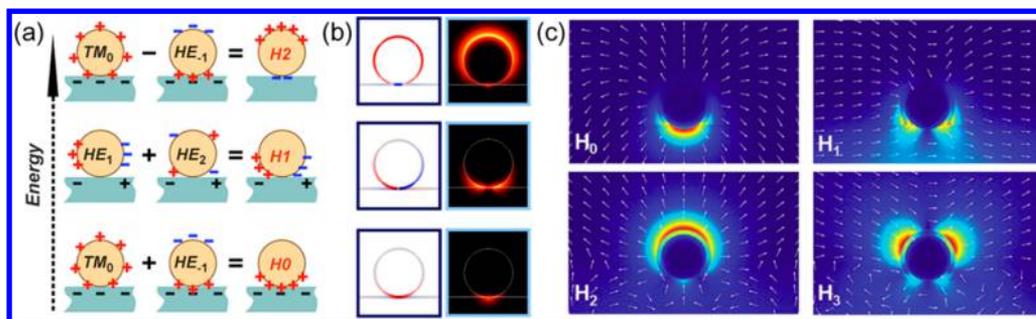
Figure 4. (a) Schematic illustration of the hybridization of plasmon modes in a cylindrical NW induced by a substrate. (b) Calculated charge and power distributions of the hybridized plasmon modes in a Ag NW on a glass substrate. The NW radius is 100 nm. The energy is 3.432 eV for H_2, 3.359 eV for H_1, and 2.988 eV for H_0. (a and b) Reprinted from ref 44. Copyright 2012 American Chemical Society. (c) Electric field distributions of the four lowest-order modes supported by a Ag NW on a glass substrate. The NW radius is 160 nm and the Al_2O_3 thickness is 30 nm. The wavelength is 633 nm. Reprinted with permission from ref 41. Copyright 2015 Royal Society of Chemistry.


Figure 5. (a, c, e) SEM images and (b, d, f) plasmon modes of metal NWs with (a, b) rectangular, (c, d) pentagonal, and (e, f) five-pointed star cross sections. (b and d) show the electric field distributions of the modes and (f) shows the charge distributions. (a and b) Reprinted from ref 50. Copyright 2013 American Chemical Society. (c and d) Reprinted from ref 51. Copyright 2011 American Chemical Society. (e and f) Reprinted from ref 52. Copyright 2014 American Chemical Society.

mode leads to larger damping of propagation, as discussed in section 3.1. For all values of NW radii, the n_{eff} of TM_0 mode is higher than HE_1 mode, due to the higher confinement of the TM_0 mode, and therefore the TM_0 mode has a shorter propagation length. For large radii, two plasmon modes show similar confinement and propagation length. The increase in n_{eff} of the TM_0 mode for smaller radii of the NW means more fields are concentrated into the metal region, which results in higher ohmic damping in the metal. According to the above discussion, the NWs with considerable mode confinement and propagation length for practical use are multimode waveguides.

3.2.2. Cylindrical Nanowires on Substrates. In experiments and applications, the NWs are usually deposited on a dielectric substrate, where the inhomogeneity of the environment modifies the supported eigenmodes of the NW.[44−46] Due to the reduced symmetry of the NW-substrate system compared with the NW in a homogeneous medium, the plasmon modes become rather complicated. Some examples of the plasmon modes of a cylindrical NW on a substrate are shown in Figure 4. These plasmon modes can be understood as the hybridization of the original plasmon modes in the NW induced by the dielectric substrate, which can be denoted as H_0,

H_1, H_2, etc.[44] The hybridization of plasmon modes is facilitated by the induced charges in the substrate, as schematically shown in Figure 4a.

However, the induced charges can only lead to coupling between two plasmon modes of the same lateral symmetry, and the resulting hybridized modes are still symmetric or antisymmetric in the lateral direction. As specifically shown in Figure 4a, the TM_0 mode mainly interacts with the vertically polarized HE_1 mode. The in-phase and out-of-phase coupling of the TM_0 mode and HE_1 mode result in the hybridized H_0 mode and H_2 mode, respectively. The energy of the H_0 mode is lower than the H_2 mode, which agrees with the hybridization theory that in-phase coupling leads to lower energy than the out-of-phase coupling. The in-phase coupling results in cancellation of the charges and the field distributed on the upper surface of the NW, while the out-of-phase coupling enhances the field on the upper surface. This is schematically illustrated in Figure 4a and further demonstrated by the distributions of charges and power obtained by simulations shown in Figure 4b. Similarly, the horizontally polarized HE_1 mode can couple with the HE_2 mode, and the in-phase coupling leads to a field distribution concentrated at the bottom
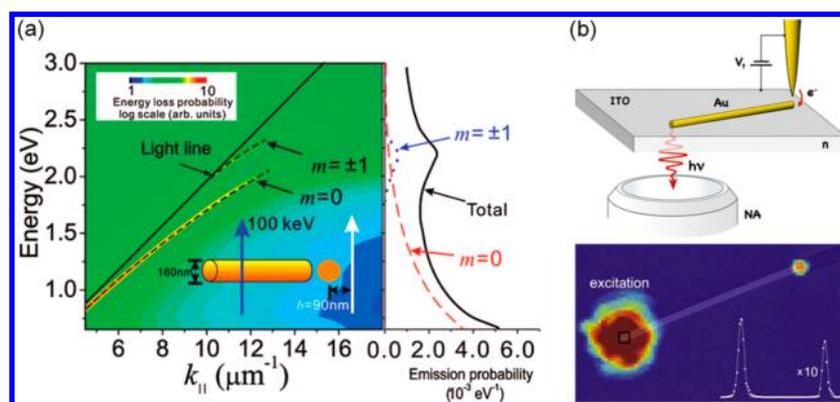
Figure 6. Excitation of NW plasmons by electrons. (a) Excitation of SPs on a Au NW by high-energy electrons (100 keV). (Left) Energy-loss probability of electrons passing at a distance of 10 nm from the surface of an infinitely long free-standing Au NW of 160 nm in diameter. The probability exhibits maxima corresponding to excitation of plasmon modes with $m = 0, \pm 1$ azimuthal symmetry. The dispersion relation of $m = 0$ and $m = \pm 1$ guided plasmons is superimposed for comparison (dashed curves). (Right) EELS probability integrated over parallel momentum (solid curve), and partial contributions of $m = 0$ and $m = \pm 1$ plasmon modes (dashed and dotted curves, respectively). Reprinted from ref 57. Copyright 2009 American Chemical Society. (b) Excitation of SPs on a Au NW by low-energy tunneling electrons (bias voltage 2 V) in a STM. (Top) Illustration of the experiment. (Bottom) Photon emission map superimposed to the SEM image of a Au NW. The tunneling current is 1 nA. The radius of the Au NW is 87 nm and the length ~5 μm. Reprinted with permission from ref 58. Copyright 2011 American Physical Society.

of the NW. This coupling can also be out-of-phase and the resulting field is distributed above the NW. Figure 4c shows more details of the field distributions of the four lowest order hybridized modes for a Ag NW on a glass substrate for a 633 nm wavelength. These modes account for the near-field distributions of the propagating plasmons on the substrate-supported NWs and show similar properties as TM_0 and HE_1 modes for a cylinder in a uniform environment since the mirror symmetry is maintained. In the following discussions of the plasmon propagation properties, we may generally refer to the TM_0 and HE_1 modes without specifying the substrate-induced modifications.

It should be noted that the hybridized modes in a NW on a substrate are not always bound guiding modes but can become leaky modes for lower frequencies. Using the H_2 mode as an example, most of the power of the mode is distributed on the upper surface of the NW, so its dispersion relation is similar to that of plasmons on a flat air−metal interface with an effective refractive index n_{eff} larger than 1. However, this n_{eff} of the H_2 mode can be less than the refractive index of the substrate, especially for lower frequencies far away from the plasmon resonance frequency. In this case, as discussed in section 3.1, the $\mathrm{Re}(k_{\parallel}) < \mathrm{Re}(n_s k_0)$ indicates that the field in the substrate is not evanescent but an extending wave, where n_s is the refractive index of the substrate. The H_1 and H_2 modes are both leaky modes for lower frequencies.[44] The H_0 mode resembles the plasmons on a flat substrate−metal interface and is a bound guiding mode for a broader frequency range. The leaky radiation causes additional energy loss for the waveguiding of plasmons, but it is useful for highly directional optical antennas.[47−49] In addition, the leaky radiation from the leaky modes of the NW can be collected by an optical microscope from the side of the substrate for optical imaging of the plasmon field, and the wave vector $k_{\parallel}$ of the leaky mode can be extracted from Fourier imaging, which will be discussed in section 5.8.

### 3.3. Plasmon Modes in Nanowires with Different Cross-Sectional Geometries

The most commonly used NWs in experiments are chemically synthesized, which may show various geometries of cross

sections depending on the conditions for crystallization. NWs of specific geometries can also be fabricated elaborately using different techniques of nanofabrication. Figure 5 shows SEM images and supported plasmon modes of chemically synthesized NWs of three different cross-sectional geometries, including rectangular, pentagonal and five-pointed star shapes. Although the symmetry of these NWs is reduced compared with the cylindrical NWs, the plasmon modes in these NWs are still similar to those in cylindrical NWs discussed in section 3.2. As shown in Figure 5 (panels b, d and f), the fundamental modes of these NWs resemble the TM_0 mode discussed in cylindrical NWs, where the sign of the charges is the same over the cross sections and the plasmon fields are basically in the radial polarization. For the second-order modes, the positive and negative charges are distributed on two sides of the NW and the fields are nearly linearly polarized. The fundamental and second-order modes in these NWs can be similarly understood from the dipole chain model used in section 3.2 (i.e., the fundamental mode and second-order modes correspond to dipole chains polarized along and perpendicular to the NW, respectively). The plasmon modes in these NWs also show similar dispersion relations as cylindrical NWs and similar dependence of n_{eff} on the diameter of the NW as shown in Figure 3e. Due to the simple geometry of cylindrical NWs, they are usually adopted for building theoretical models for the phenomena observed in the metal NWs used in experiments.

4. EXCITATION AND DETECTION OF SURFACE PLASMONS

4.1. Exciting Plasmons on Metal Nanowires

The scheme for exciting SPs can be classified into three different categories: by electrons (high-energy electron beams or low-energy tunneling electrons), by photons (free-space photons or guided photons), and by luminescent emitters (atoms, molecules, quantum dots/wires/wells, etc.). The optical excitation methods are most widely used for generating propagating SPs on metal NWs. Both the optical excitation using single photon sources[53] and the excitation by single quantum emitters[20] can generate single quantized plasmons.
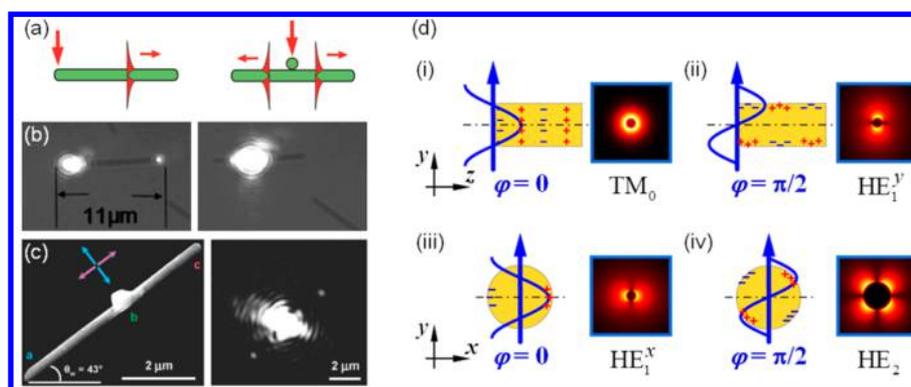
Figure 7. Optical excitation of NW SPs via scattering at points of broken symmetry. (a) Schematic of SP excitation by a focused laser beam via scattering by the NW end or by a scatterer on the NW. (b) Optical imaging of SP excitation on a Ag NW by the end-scattering method. SPs cannot be excited when the laser is positioned at the middle of the NW. Reprinted from ref 63. Copyright 2006 American Chemical Society. (c) Nanoparticle-mediated optical excitation of SPs on a Ag NW. Reprinted from ref 64. Copyright 2007 American Chemical Society. (d) Optical excitation of different SP modes via the end-scattering scheme for incident polarization parallel (i, ii) or perpendicular (iii, iv) to the NW axis. φ denotes the incident phase of the excitation beam. Reprinted with permission from ref 70. Copyright 2011 American Physical Society.

When a high-energy electron beam is focused onto or nearby a metal nanostructure, the electric field around the electron beam may induce collective oscillations of the free electrons in the metal (i.e., plasmons), due to the Coulomb interaction.[54] The electric field around the moving electrons contains Fourier components of all frequencies, and therefore plasmons at different frequencies can be excited simultaneously. Due to energy conservation, the high-energy electrons experience different energy losses during this process. The transmitted electrons are collected and spectrally analyzed, providing the information about the plasmon excitation in the specimen. The technique, called electron energy loss spectroscopy (EELS), can be available in a commercial TEM. EELS represents a versatile tool to study the plasmon behaviors on various metal nanostructures, including localized SPs on individual nanoparticles[55] and propagating SPs on NWs.[56] Theoretical calculation shows that both the TM_0 ($m = 0$) and HE_1 ($m = \pm 1$) modes can be excited by electrons passing at a distance of 10 nm away from the surface of an infinitely long gold NW, as shown in Figure 6a.[57] The energy-loss probability of electrons is about $1-5 \times 10^{-3}$ eV^{-1}, with the contribution of the TM_0 mode dominating in the low-energy region.

The excitation of plasmons by electrons can also be accomplished by inelastic quantum tunneling of electrons.[59] Briefly, when a bias voltage is applied across a tunneling junction, the electrons experience an energy drop when passing through the junction. This inelastic scattering of an electron may excite a plasmon, with a probability of 10^{-5} in a planar metal-isolator-metal junction. The energy of the excited plasmons is determined by the applied voltage (i.e., a higher bias can lead to a blue-shifted spectrum of the plasmons).[59] The excitation of plasmons in a tunneling junction was first observed in a scanning tunneling microscope (STM) via the radiative decay of plasmons into light emission.[60] Taking advantage of the confinement of the localized SPs in the tip–surface junction, the efficiency of the plasmon generation can be significantly improved.[61] The excitation of SPs on a gold NW was realized by using a gold tip on a STM.[58] As shown in Figure 6b, when the tip is located on top of one end of the NW, light emission from the other end of the NW can be detected by a CCD, indicating the excitation of propagating SPs.

Since the momentum of a plasmon is larger than that of light, optical excitation of SPs on a NW requires schemes for momentum compensation. In accordance with the coupling mechanisms, the schemes for optically exciting SPs on NWs can be divided into four types: (i) scattering of free-space photons at points of structural symmetry breaking, (ii) transverse evanescent coupling from guided photons in dielectric waveguides, (iii) mode transformation in a butt-coupling configuration, and (iv) grating assisted coupling of free-space photons.

As shown in Figure 7a, exciting SPs by scattering [scheme (i)] can be performed by using an objective to focus a laser beam directly onto a symmetry-broken point, such as one end of the NW, a kink or a cut in the NW or a nearby scatterer (nanoparticle, NW, scanning tip, etc.).[62−67] Incident light at these points can be scattered into components with a wide range of wave vectors, a small part of which can match with SPs on the NW and enable the excitation. This method is easy to realize using a commercial optical microscope and is widely used. For the example shown in Figure 7b, by focusing laser light with a wavelength of 830 nm onto the end of a Ag NW, SPs are excited as evidenced by the light emission spot at the other end of the NW (left panel). However, no SP excitation is observed when the laser is focused on the midsection of the same NW (right panel of Figure 7b). SP excitation was also reported when embedding one end of a Ag NW in a polymer photonic waveguide.[68] The main coupling mechanism in this objective-free configuration is also attributed to a scattering process at the NW ends, where the free-space photons were replaced by guided photons. The first experimental observation of SP propagation on gold and Ag NWs reported in 2000[69] was in principle accomplished by the end-scattering method, because the total internal reflection configuration used in the experiment does not provide enough momentum to launch the nonleaky TM_0 plasmon mode directly from the NW trunk. The scattering excitation of SPs on a NW can also be realized by a nearby nanoparticle, as shown in Figure 7c.[64] The coupling efficiency reaches maximum when the incident polarization is parallel to the nanoparticle-NW interconnecting line, namely, perpendicular to the NW axis.

The excitation of different SP modes using the end-scattering coupling scheme is dependent on the polarization of the incident light.[70,71] As illustrated in Figure 7d, for incident polarization parallel to the NW axis, both the TM_0 mode and the y-polarized HE_1 mode can be excited. For perpendicular
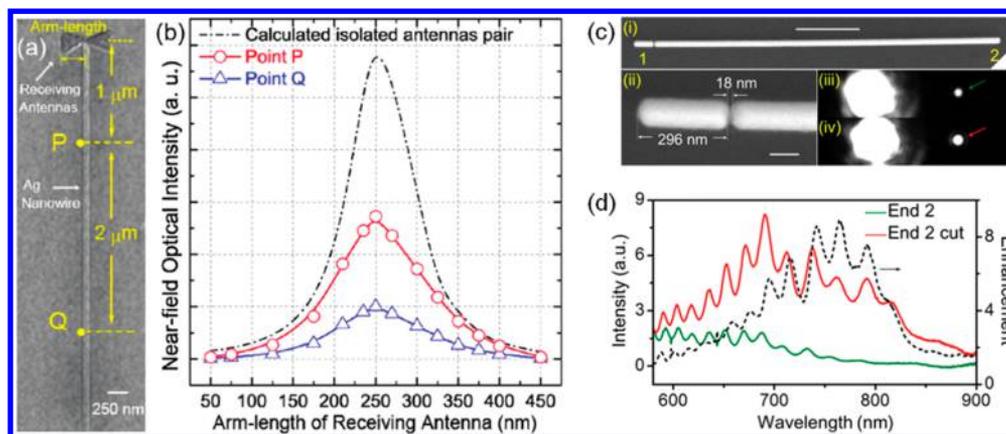
Figure 8. Increasing the coupling efficiency of NW SPs by nanoantenna couplers. (a) SEM image of a Ag NW transferred to a receiving bowtie antenna fabricated by EBL. (b) Near-field intensity as a function of the arm-length of the receiving antenna. The wavelength of the excitation laser is 672 nm. (c) (i, ii) SEM images of the self-aligned nanorod antenna fabricated by cutting a nanorod at the input end of a Ag NW by FIB. The scale bar is 1 μm in (i) and 100 nm in (ii). (iii, iv) Optical images of the NW under supercontinuum laser excitation (iii) before and (iv) after the FIB cutting. (d) Measured transmission spectra at the output end of the NW before (green) and after (red) cutting. The black dashed line is the ratio of the transmission with and without the cut. (a and b) Reprinted from ref 73. Copyright 2011 American Chemical Society. (c and d) Reprinted with permission from ref 74. Copyright 2014 Wiley.
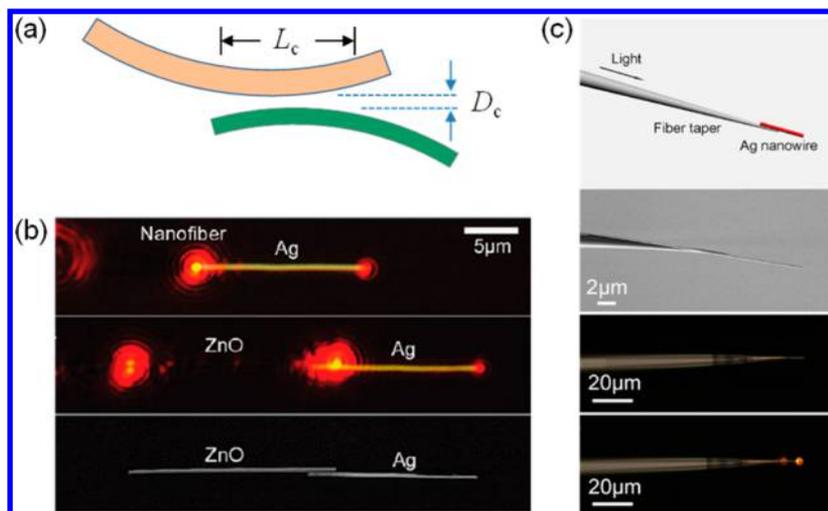
Figure 9. Optical excitation of NW SPs via transverse evanescent coupling from dielectric waveguides. (a) Schematic drawing of SP coupling using a directional coupler. (b) SP excitation by transversely attaching a tapered nanofiber or a ZnO NW to a Ag NW on a substrate. The diameters of the ZnO and Ag NWs are 340 and 320 nm, respectively. The wavelength of the excitation laser is 650 nm. Reprinted from ref 75. Copyright 2009 American Chemical Society. (c) Highly efficient SP excitation on a suspended Ag NW held by a sharp fiber taper. The diameter of the Ag NW is 280 nm and the wavelength of the laser is 785 nm. Reprinted with permission from ref 77. Copyright 2013 Optical Society of America.

polarization, the x-polarized HE_1 mode and a higher-order HE_2 mode can be excited. Consequently, for incident polarization with an angle with respect to the NW axis having both projected polarization components, the TM_0 mode and two degenerate HE_1 modes are excited on the NW simultaneously. Comparing Figure 7d (ii and iii), one can find that the excitation of the HE_1 mode in the x- and y-directions under linear polarization corresponds to an instantaneous profile with a phase delay of $\pi/2$. Therefore, the two HE_1 modes have a $\pm \pi/2$ phase difference under this excitation configuration. The amplitudes of the two HE_1 modes and the sign of the phase delay can be controlled by the incident polarization angle with respect to the NW axis.

For free-space photons, the diffraction limit imposes a lower bound on the spot size of the light beam. Therefore, the coupling efficiency of free-space photons into the tightly confined SPs is low, especially when the diameter of the NW is very small. To increase the coupling efficiency, a nanoantenna can be employed at the end of the NW. A simulation study shows that, by introducing a dipole nanoantenna at the entrance of a NW dimer waveguide, an enhancement of more than 200 times of the coupling efficiency can be achieved under optimized conditions.[72] By tuning the resonance frequency of a bowtie antenna at the NW end to match with the incident laser, a 32 fold increase in the coupling efficiency was achieved experimentally (Figure 8, panels a and b).[73] A simpler scheme of improving the coupling efficiency is introducing an antenna by a cut at the entrance end of the metal NW.[74] As shown in Figure 8 (panels c and d), a cut at the entrance improved the coupling efficiency over a broad band of the spectrum, with maximum enhancement of 7.7 times.

The optical excitation scheme (ii), transverse evanescent coupling from guided photons in photonic waveguides, is another frequently used method to launch SPs onto a metal

NW due to its high efficiency. As shown schematically in Figure 9a, the two waveguides are put side-by-side so that their evanescent fields overlap. The coupling mechanism is equivalent to the directional coupler in fiber optics and integrated photonics. Similarly, for given waveguides, the efficiencies of photons coupled to the two output ports of the junction are determined by two parameters, the length of the overlapping region L_c and the distance between the two waveguides D_c. A representative example of the evanescent coupling is the coupling between a tapered optical fiber and a metal NW (top panel of Figure 9b, and Figure 9c).[75] The coupling efficiency of photons in a tapered nanofiber to SPs on a Ag NW decreases as the angle between the fiber and the NW increases. Maximum coupling efficiency reaches 55% when the two waveguides are nearly parallel to each other.[76] For a NW on a dielectric substrate, a large portion of the field for the fundamental mode is distributed close to the substrate, which limits the coupling efficiency from the tapered fiber to the metal NW. For suspended NWs, the efficiency of coupling can be further improved. Figure 9c shows the excitation of SPs on a suspended Ag NW held by a fiber taper. The small scattering spot at the overlapping region indicates the high efficiency (92%) of this coupling scheme at 785 nm.[77] SPs on metal NWs can also be excited by the evanescent coupling of a dielectric NW and a metal NW (middle and bottom panels in Figure 9b).[75] For the coupling from the guided photons in a ZnO NW to SPs on a Ag NW, a coupling efficiency of 82% was obtained. A short coupling length of L_c = 200 nm was achieved since two NWs were close to each other.

For the butt-coupling geometry between a dielectric waveguide and a metal NW (Figure 10, panels a and c), a high conversion efficiency of 95% in the visible and close to 100% in the near-infrared can be reached, when the diameters of the two waveguides are matched so that a standing wave at the metal-dielectric interface appears.[78] The calculation results for the coupling of a focused radially polarized beam to the TM$_0$ mode in a metal NW shows that the coupling efficiency can reach as high as 90% when the distribution of the focus beam matches well with the radiation pattern of the TM$_0$ mode SPs at the NW terminal.[79] Adiabatic mode transformation is another efficient way of coupling guided modes onto SPs on metal NWs (Figure 10b). By this method, efficient launching of SPs on a gold NW was realized.[80] As shown in Figure 10d, SPs on a gold film of 77 nm thickness were first excited at a nanohole array on the left side of a taper, which was connected to a NW of 150 nm width on the right. The SPs propagated along the laterally tapered metal stripe and were adiabatically converted to the fundamental plasmon mode in the NW. For a NW of 90 nm width, the coupling efficiency of the taper coupler was measured to be ∼50%.

The grating-assisted optical excitation scheme is a very popular method to launch SPs on metal films. The excitation condition becomes $Re(k_{\parallel}) = k_0 \sin\theta + 2\pi/a$, where θ is the incidence angle relative to the surface normal and a is the grating constant. However, there is no experimental demonstration of the grating-coupled excitation of SPs on metal NWs. There are a few reports on fabricating grating structures on chemically synthesized metal NWs, either by FIB or EBL.[81−83] However, all of these works used the grating as a Bragg mirror for SPs rather than as a coupler. Experimental demonstration of a grating coupler on a metal wire was carried out in the THz range,[84] where spoof SP waves (also called Sommerfeld waves) rather than SPs are supported. The spoof SP wave is weakly bound on the metal surface since the dispersion curve is located close to the light line.[85]

In practical experimental realizations, the excitation of SPs may involve more than one mechanism. For example, the excitation of SPs on a metal NW by a photonic waveguide may contain the (i) scattering and (ii) evanescent coupling, if the photonic waveguide and the metal NW are not parallel to each other. The scattering mechanism can be dominant if the angle between two waveguides is large. For a fiber taper, as shown in Figure 9c, the coupling may also involve the scattering mechanism if the end of the taper is close to the metal NW, even if the two waveguides are parallel to each other. It also includes a mode conversion process as in the butt-coupling method if the end of the fiber taper is positioned right in front of the metal NW end. Therefore, the coupling mechanisms depend strongly on the exact geometries of the coupling structures.

SPs on metal NWs can also be excited by a nearby luminescent emitter (e.g., an atom, a molecule, a QD, etc). Theoretical calculations reveal that a dipole emitter can couple strongly to the TM$_0$ mode SPs on a metal NW.[19,39] A near unity coupling efficiency can be achieved when the dipole emitter is placed right at the tip of a NW, with its dipole orientated along the NW axis. For an emitter located at the side of a NW, this coupling efficiency depends sensitively on the distance between the emitter and the NW surface and the orientation of the dipole emitter. Small emitter-NW distance is usually favorable for high coupling efficiency. However, the nonradiative decay of the excited emitter increases as the emitter-NW distance decreases, which reduces the quantum efficiency of the SP generation for very small distances. The luminescent quantum transitions may be pumped electrically, for example, in a GaAs NW with a p-i-n junction and a carbon nanotube transistor,[86,87] which can also be applied for exciting

Figure 10. (a) Butt-coupling from a dielectric waveguide (orange) to a metal NW (green). (b) Exciting SPs on a metal NW by adiabatic mode transformation. (c) Theoretically optimized excitation of SPs on a Ag NW by a dielectric fiber. (Left) Calculation geometry, a light source is inserted at the dielectric fiber. (Right) Snapshot of the magnetic field distribution at the coupling junction. Reprinted from ref 78. Copyright 2009 American Chemical Society. (d) Experimental demonstration of SP excitation by adiabatic mode transformation onto a Au NW. Reprinted with permission from ref 80. Copyright 2009 American Physical Society.

Table 1. Excitation Efficiency of NW SPs

source	coupling scheme	structure	optimized coupling efficiency	ref
electrons	fast electrons	Au NW, diameter D = 160 nm, electron-NW distance d = 10 nm	~1% (calcd)	ref 57
photons	end-scattering	Ag NW, D = 98 nm, wavelength λ = 681 nm	~4% (calcd)	ref 74
	evanescent coupling	ZnO NW (diameter 270 nm), Ag NW, D = 240 nm, MgF$_2$ substrate, λ = 650 nm	~82% (exptl)	ref 75
		fiber taper (end diameter 300 nm), Ag NW, D = 280 nm, λ = 785 nm	92% (exptl)	ref 77
	butt-coupling	from a silica nanofiber (diameter 684 nm) to a Ag NW, D = 328 nm, λ = 633 nm	95% (calcd)	ref 78
		focused radially polarized light beam, Ag and Au NWs embedded in glass, D = 320 nm, λ = 633 nm	~90% (calcd)	ref 79
	adiabatic mode transformation	Au NW of 77 nm thick and 90 nm wide, λ = 1550 nm	~50% (exptl)	ref 80
emitters	—	emitter near a Ag nanotip, λ = 1000 nm, surrounding dielectric permittivity ε = 2	95% (calcd)	ref 19
	—	emitter on the side of a Ag NW, D = 100 nm, emitter-NW separation d = 10−100 nm, λ = 655 nm	~30%−55% (calcd)	ref 20
	—	CdSe/ZnS QD, Ag NW, D = 80 nm, Al$_2$O$_3$ spacer thickness T = 10 nm, λ = 650 nm	21% (exptl)	ref 88
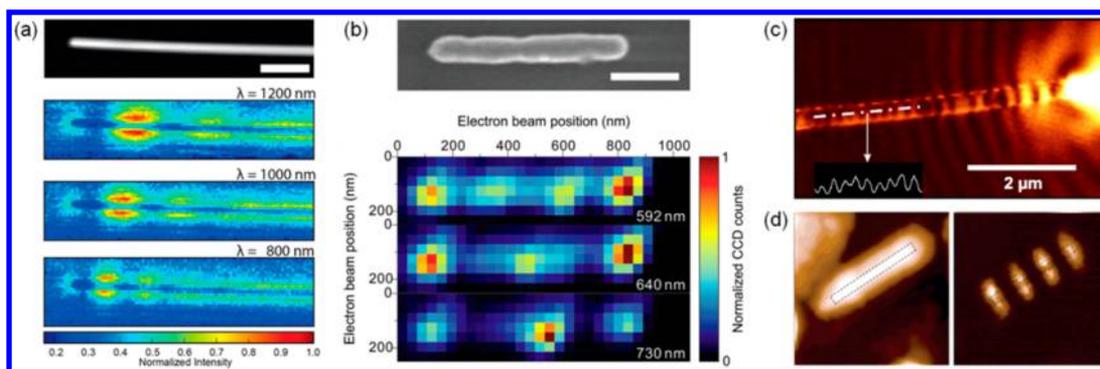
Figure 11. Imaging of NW SPs. (a) Excitation and spectrally resolved mapping of SPs on a Ag NW by high-energy electrons (accelerating voltage 300 kV) using EELS. (Top) Scanning TEM annular dark field image of a long Ag NW near one end. The scale bar is 500 nm. (Lower three panels) LDOS maps of the SPs on the NW taken at electron energy losses corresponding to three different free-space wavelengths of 1200, 1000, and 800 nm. Reprinted from ref 90. Copyright 2015 American Chemical Society. (b) (Top) SEM image of a Au NW. (Bottom) CL imaging of SPs on the Au NW at the wavelengths of 592, 640, and 730 nm. The scale bar is 250 nm. Reprinted from ref 94. Copyright 2007 American Chemical Society. (c) Imaging SPs on a Ag NW by SNOM. The NW diameter is 120 nm. The laser wavelength is 785 nm. Reprinted with permission from ref 36. Copyright 2005 American Physical Society. (d) Imaging SPs by TPPL excited by SNOM. (Left) Topographic image of the measured Au nanorod. (Right) TPPL imaging over a 700 × 700 nm region. Reprinted from ref 105. Copyright 2004 American Chemical Society.

propagating SPs. The electrical excitation benefits the on-chip integration of plasmon sources and waveguides. A more detailed review on the emitter-NW coupling is presented in section 6. Table 1 summarizes the efficiency of exciting SPs on metal NWs by different methods.

4.2. Detecting Plasmons on Metal Nanowires

As discussed in the previous section, SPs on NWs can be excited by electrons, photons, and emitters. The interactions with probe electrons/photons/emitters also allow the detection of SPs. For excitation by fast electrons, the probability for the electron losing the quanta of energy is proportional to the photonic LDOS at corresponding energy. Therefore, the EELS signal from scanning a focused electron beam over the sample provides an approach for high-resolution spatial mapping of the LDOS of the plasmons, enabled by the short wavelength of the high-energy electrons (typically, ~200 keV).[89] EELS has been used to map the spatial distribution of SPs on metal NWs.[56,90−93] By using a monochromated electron source, high-resolution imaging of Fabry-Pérot-type SP resonances of ten orders on single Ag NWs was reported, with a high-energy resolution of 0.1 eV.[56] The EELS spectrum shows discrete energy peaks corresponding to the longitudinal Fabry-Pérot resonances resulting from the reflections at the NW terminals. For a NW that is long enough compared with the propagation

length of SPs, interference ripples can only be seen close to the near end of the NW, as shown in Figure 11a. Because of the semi-infinite long feature of the NW, SPs of arbitrary frequency can be excited. The intensity maxima in the map correspond to the positions where electrons have a larger probability of losing energy at a given frequency. Therefore, the map directly relates to the LDOS of the plasmons.

The excitation of SPs by fast electrons can also be mapped out by collecting the emitted photons (cathodoluminescence, CL) instead of analyzing the transmitted electrons. CL analysis is usually an attachment on a commercial SEM. The spatial resolution of CL is several to tens of nanometers, depending on the accelerating voltage of the electron beam. CL imaging of SPs on a gold NW is shown in Figure 11b.[94] The spatial nodes along the NW axis show the Fabry-Pérot resonances at different energies. From these maps, the wavelengths of the SPs can be directly determined. Such energy and spatial resolved imaging enables the measurement of the dispersion relation of the SPs on gold NWs. Photoemission electron microscopy (PEEM) can also be used for high-resolution mapping of SPs. As opposed to CL, PEEM collects and analyzes the emitted electrons excited by intense light. SPs on a gold NW were mapped by PEEM imaging.[95] PEEM was also used to visualize the propagation and interference of SPs in a directional coupler made of two-wire transmission lines.[96] Time-resolved photon-induced near-
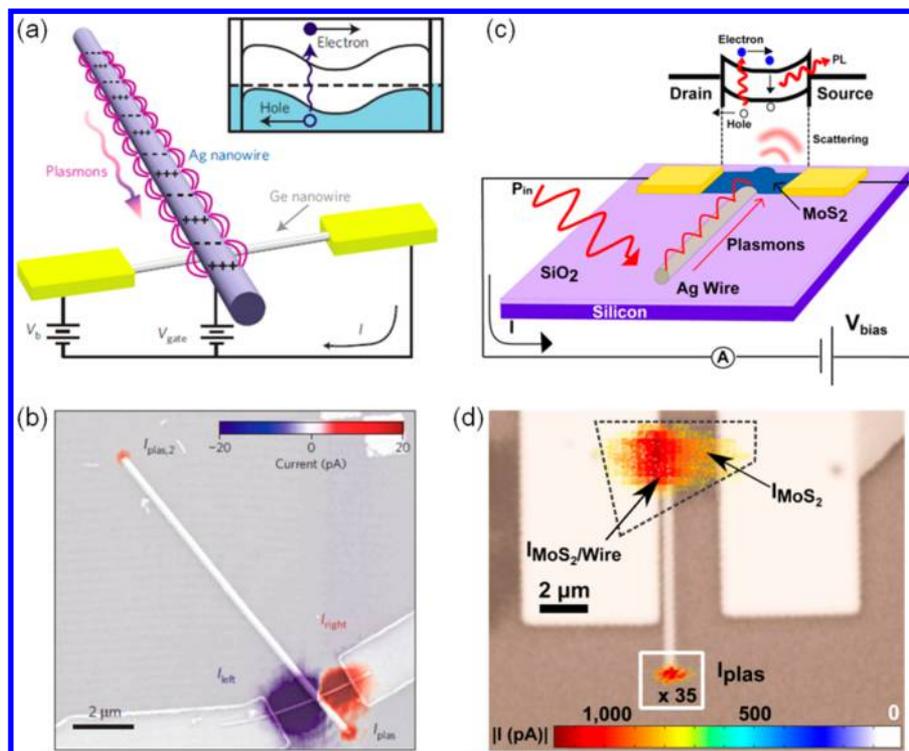
Figure 12. On-chip electrical detection of NW SPs. (a) Schematic diagram of a SP detector using a Ge NW field-effect transistor. (b) SEM image of the device overlaid with a photocurrent mapping with an excitation laser power of 2.0 μW and wavelength of 532 nm. (c) Schematic diagram of a NW SP detector using a single layer of MoS_2. (d) Photocurrent mapping overlaid on top of a SEM image of a SP detector using a monolayer of MoS_2. (a and b) Reprinted with permission from ref 108. Copyright 2009 Nature Publishing Group. (c and d) Reprinted from ref 109. Copyright 2015 American Chemical Society.

field electron microscopy, a recently developed technique, is capable of imaging SPs with high spatial, spectral, and time resolution. It uses a short laser pulse to excite SPs and subsequently images the near field of the SPs by the electrons excited by an ultraviolet pulse at a tunable delay. The interaction between the electrons and the SP standing wave in an isolated Ag NW was detected by this technique.[97]

SPs on metal NWs can be detected by optical means. One simple way of detection is to measure the emission intensity or spectrum at the output end of the NW. For short NWs, dark-field scattering spectroscopy or extinction spectroscopy can be used to measure the spectra.[98,99] Using the Fabry-Pérot model, important parameters such as group velocity, propagation length, and the reflectivity at the NW terminal can be obtained.[36,100] Complementary to far-field spectroscopy, near-field measurement can provide additional information. Direct mapping of SPs by scanning near-field optical microscopy (SNOM) can reveal the SP wavelength, near-field intensity, etc.[36,101−104] Similar to the excitation process by scattering, a nanotip close to the surface of a NW can scatter the near field of SPs into photons, either to guided photons in an apertured tip (aperture type SNOM) or to free-space photons collected by an objective (scattering type SNOM). By scanning the tip over the NW, the spatial distribution of the SPs can be mapped out. Figure 11c shows a SNOM image of SPs propagating along a Ag NW.[36] Clear Fabry-Pérot interference ripples can be identified along the NW. Typically, SNOM detects the elastically scattered light at the same frequency as the excitation beam. If the excitation light intensity is strong enough, SPs can be mapped by collecting the two-photon photoluminescence (TPPL). Figure 11d shows the SP mapping on a gold nanorod

using TPPL excited by a Ti: sapphire laser (λ = 780 nm, < 100 fs) through an apertured SNOM tip.[105] For the leaky plasmon modes in metal NWs, the leaky radiation enables direct optical imaging of these modes, as will be seen in section 5.8.

The quantum transitions (in molecules, QDs, semiconductors, etc.) excited by SPs can be used for the detection as well. As the reverse process of SP excitation by quantum emitters, the SPs on a NW can excite electronic transitions which can then be detected optically or electrically. The excitation rate of the emitters is proportional to the near-field intensity of the SPs. If the near field is not strong enough to saturate the emitters, the intensity of fluorescence (radiative decay of the emitters into photons) from the emitters is proportional to the excitation rate. Therefore, if the emitters cover the metal NW uniformly, the fluorescence image of the sample directly reflects the near-field intensity distribution of the SPs (Figure 3d).[17] To increase the brightness of the image, QDs and dye molecules with high emitting efficiencies are good candidates for fluorescence imaging. Compared with dye molecules, the QDs have the advantage of long fluorescence duration. By this method, the periodic near-field patterns formed due to plasmon beating and exponential decay of the near-field intensity can be mapped out using a normal optical microscope. By combining conventional SNOM and fluorescence lifetime imaging microscopy, scanning an emitter (dye molecules embedded in a polystyrene bead with a diameter of 100 nm) attached onto the tip of a tapered nanofiber can map the LDOS of SPs on a metal NW.[106] The measured fluorescence intensity and dynamics reveal information about the photonic environment with a resolution beyond the diffraction limit. Fluorescence lifetime imaging was also performed by scanning

a nitrogen vacancy (NV) center in a nanodiamond attached to the tip of an atomic force microscope (AFM) over a Ag NW.[107] Compared to the fluorescent nanobead, the NV center is more chemi- and photostable. More importantly, it can function at the single quantum emitter level with a specific dipole position and orientation.

The excitation of an electronic transition creates a "hot" electron in the conduction band (and a hole in the valence band) that can be converted to electrical signals. By applying a voltage, the generated free carries (electrons, holes, or both) can be driven to the electrodes resulting in a current. The advantage of this detection scheme is that it is capable of on-chip detection in integrated circuits. The electrical detection of plasmons on a Ag NW was reported by using a Ge NW field-effect transistor (Figure 12, panels a and b).[108] A detection efficiency of 0.1 electrons per plasmon was achieved. With a gating effect, the signal can be further increased by about 500 times. A similar scheme of on-chip detection of NW SPs has also been demonstrated by using a monolayer of MoS_2.[109,110] As shown in Figure 12c, an electron−hole pair is created when a plasmon is absorbed. The electrons (holes) are moved under the applied voltage, producing the current. Compared with the Ge NW transistor, the direct band gap nature of the monolayer of MoS_2 indicates a larger strength of light-matter interaction compared to the indirect band gap materials. Furthermore, the sheet nature of the semiconductor layer increases the contact area with the metal NW, increasing the produced electric current (Figure 12d). The flexible feature of the layered materials enables their integration with different types of substrates. Therefore, it is promising for future on-chip integrated nanophotonic circuits.

On-chip SP detection can also be realized by a super-conducting single-photon detector. The absorption of a single photon/plasmon produces a short-lived resistive state, which is detected as a voltage pulse. By using a superconducting single-photon detector consisting of a meandering NbN wire (∼100 μm long, 100 nm wide, 5 nm thin) cooled at 4 K, SPs on gold strip waveguides were detected.[111] A high sensitivity was demonstrated by detecting single plasmons generated by a QD. Using a metal quantum point contact, SP induced optical rectification can be used for on-chip electrical detection of SPs. Such a SP detector was demonstrated by fabricating a $1G_0$ quantum point contact via field induced adatom migration.[112] When SPs were generated at the grating structure, they propagated to the metal nanogap and excited localized SPs therein. The local electromagnetic field was enhanced at the junction so that the conductance of the junction was modulated. Monitoring the conductance of the junction provides a means for SP detection.

5. PROPAGATION AND EMISSION OF SURFACE PLASMONS

5.1. Beating and Zigzag Propagation

Although the field amplitudes of the TM_0 mode and HE_1 mode are both laterally symmetric and uniform along the NW (Figure 3), the interference of the two modes in a NW leads to an asymmetric, zigzag field distribution, as shown by the charge (Figure 13a, left) and field (Figure 13a, right) distributions. The asymmetry of the zigzag field distribution originates from the different lateral symmetries of the TM_0 mode and HE_1 mode that participate in the interference. As shown in Figure 3b, the sign of the charge distribution in the TM_0 mode is the
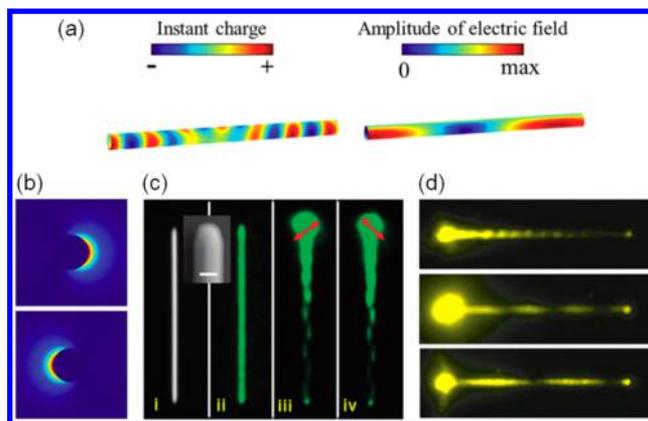
Figure 13. (a) Simulation results for distribution of instant charges (left) and electric field amplitude (right) of plasmons on a cylindrical Ag NW, with TM_0 mode and HE_1 mode input simultaneously. (b) Field distributions obtained by directly adding the TM_0 and HE_1 modes, with relative phase differences of 0 and π. The initial phase difference of 0 is defined by the distribution in Figure 3a. (c) Experimental observation of the zigzag field distribution on a Ag NW. Panels (i and ii) show the optical image and the QD florescence image with wide field excitation of the NW. The inset is a SEM image with the scale bar of 200 nm. Panels (iii and iv) show the QD florescence images of the plasmons generated by a linearly polarized laser beam, with the polarization indicated by the red arrows. (d) Periodic field distributions on a glass-substrate-supported Ag NW immersed in air (top), water (middle), and oil (bottom), excited by a laser beam polarized parallel to the NW. (a and b) Reprinted with permission from ref 41. Copyright 2015 Royal Society of Chemistry. (c) Reprinted from ref 17. Copyright 2011 American Chemical Society. (d) Reprinted with permission from ref 113. Copyright 2013 National Academy of Sciences of the USA.

same over the cross section of the NW, while for the HE_1 mode the charges show opposite signs on two sides of the NW. The superposition of the two modes yields net charges piling up on one side of the NW (Figure 13a, left). Figure 3a also shows that the polarization of the lateral electric field component E_x of the TM_0 mode and the HE_1 mode are different, so that their superposition shows destructive and constructive interference separately on two sides of the NW, leading to an asymmetric field distribution (Figure 13b).

The period of the zigzag distribution in Figure 13a is formed due to the plasmon beating effect. The TM_0 and HE_1 modes with different refractive indices accumulate different phases along the NW, leading to the maxima of the electric field periodically distributed on the NW. For the distributions of the TM_0 and HE_1 modes shown in Figure 3a, their interference field is asymmetric and the maximum is located on the right side of the NW (Figure 13b, top). Along the propagation direction, the two modes accumulate different phase changes and when the phase difference reaches π, the maximum of the field shifts to the left side of the NW (Figure 13b, bottom). The repetitive shifting of the field maxima along the NW leads to a zigzag propagation route, with the period Λ given by $\Lambda = \lambda/(n_0 - n_1)$, where n_0 and n_1 are the effective refractive indices of the TM_0 mode and the HE_1 mode, respectively. Considering the dependence of n_0 and n_1 on the radius of the NW shown in Figure 3e, the period of the zigzag field pattern is shorter in thinner NWs.

The zigzag propagation of plasmons on NWs can be proved experimentally by the QD fluorescence imaging technique, as shown in Figure 13c. By focusing a laser beam with linear

polarization at an acute angle (e.g., 45°), with respect to the NW, the TM_0 mode and the HE_1 mode polarized parallel to the substrate can be generated simultaneously. As revealed by the QD fluorescence image (Figure 13c, iii), the plasmons on the NW are in a zigzag route with a unique period due to the superposition of the TM_0 and HE_1 modes. When changing the polarization from 45° to −45° (0° corresponds to the polarization parallel to the NW), the zigzag distribution is reversed as a mirror image (Figure 13c, iv). This modulation of the plasmon field on the NW induced by the polarization direction can be utilized for plasmon routers, as will be elaborated in section 8.1. As clarified in Figure 7d, the laser beam can also generate a HE_1 mode polarized perpendicular to the substrate, which is not included in the discussion above. For a laser beam with the polarization parallel to the NW, this vertically polarized HE_1 mode and the TM_0 mode can be excited simultaneously, which also leads to a periodic near-field pattern. This periodic distribution also has a zigzag pattern, where the maxima shift periodically between the upper and bottom surface of the NW, with the field distribution on the upper surface captured by a microscope, as shown in Figure 13d (also see left panel of Figure 3d). Since the beat period of the zigzag distribution on the NW is determined by the effective refractive indices of the two modes, changing the environment of the NW can modulate the mode indices and consequently alter the beat period, as demonstrated in Figure 13d. This not only offers a way to flexibly tune the plasmon field but also provides an ultrasensitive platform for on-chip sensing.

Since the zigzag distribution results from the superposition of two modes with different lateral symmetry, it is not limited to cylindrical NWs. As discussed in section 3, for the NWs with different cross-sectional geometries, even if the NWs are deposited on a substrate or further covered by a coating layer (which is actually the case in Figure 13, panels c and d), as long as the mirror symmetry of the NWs is preserved, they can support symmetric and antisymmetric plasmon modes and sustain the zigzag field distributions.

5.2. Chiral Propagation

By the superposition of two degenerate HE_1 modes with a $\pi/2$ phase delay, a state with a helical phase distribution as $e^{\pm i\varphi}$ is formed. The interference of this helical mode with an additional TM_0 mode generates a helically distributed near-field energy flow along the metal surface. The helical distribution of SPs on a metal NW is clearly revealed by the distributions of the instant charge and electric field amplitude (Figure 14a), which are obtained by numerical superposition of the three mode components with the required phase.

The simultaneous excitation of two degenerate HE_1 modes with $\pi/2$ phase delay and a TM_0 mode in a metal NW can be achieved by the end-scattering scheme with a light beam polarized at an angle with respect to the NW axis (e.g., 45°), as discussed in Figure 7d. Since the excitation of the vertically polarized HE_1 mode is due to a retardation effect, it is less efficient, especially for thin NWs, than the excitation of the horizontally polarized HE_1 mode by the linearly polarized electric field of the light beam. Moreover, the substrate employed in the experiment can also lift the degeneracy of the two HE_1 modes. Therefore, only for a relatively thick NW in a homogeneous environment, the chiral plasmons can be directly excited by a linearly polarized light beam.
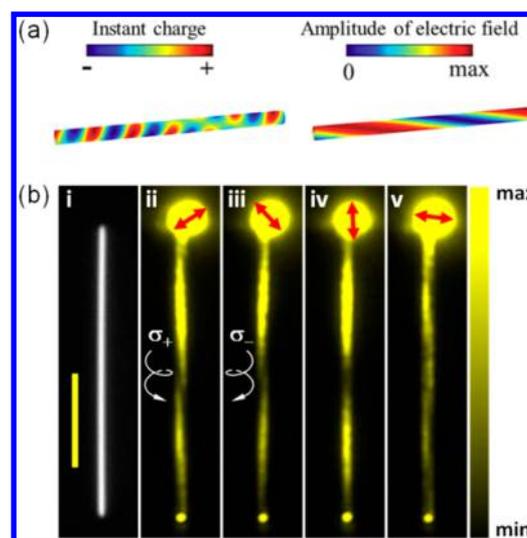

Figure 14. Chiral SPs on metal NWs. (a) Simulation results for distributions of instant charges (left) and electric field amplitude (right) of plasmons on a cylindrical NW, with the TM_0 mode and two degenerate HE_1 modes with a $\pi/2$ phase delay input simultaneously. Reprinted with permission from ref 41. Copyright 2015 Royal Society of Chemistry. (b) Experimental detection of chiral SPs by QD fluorescence imaging for a Ag NW of radius ~150 nm. The scale bar is 5 μm. Reprinted with permission from ref 70. Copyright 2011 American Physical Society.

Experimental verification of the chiral SPs on a chemically synthesized Ag NW was performed by fluorescence imaging using colloidal QDs, as shown in Figure 14b. In order to maintain the cylindrical (more exactly, pentagonal) symmetry, the Ag NW was immersed in refractive index matching oil. Fluorescence imaging clearly resolved the handedness of the chiral SPs. By changing the incident polarization angle from 45° to −45°, the handedness of the plasmon helix is reversed. The helical distribution disappeared for parallel and perpendicular incident polarizations. The period of the chiral SP pattern is the same as the zigzag distribution and determined by $\Lambda = \lambda/(n_0 - n_1)$, which increases with the increase of the NW diameter, as discussed in section 5.1. The incident polarization angle can alter the relative amplitude of the HE_1 mode in the x- and y-directions, which further determines the degree of circular polarization of the chiral SPs. Chiral SPs can also be generated from the superposition of the HE_1 mode and HE_2 mode, which yields triple-stranded spiral SPs.[114]

5.3. Spin-Dependent Propagation

In addition to the excitation approach using a laser beam with linear polarization as discussed in sections 5.1 and 5.2, launching plasmons on NWs by circularly polarized light is more profound, since the circular polarization of light is an intrinsic degree of freedom, which can be explored for binary signal encoding and routing. Recent research interests have been intensively devoted to the directional excitation of plasmons using circularly polarized light, where photons of opposite circular polarizations are directed to different spatial routes when coupled as plasmons.[115−119] This spin-dependent directional excitation is achieved by exploring the spin−orbit interaction (SOI) of light, which occurs when circularly polarized light moves along curved trajectories in a homogeneous medium, such as by scattering or reflection. Along these curved trajectories, the spin angular momentum (AM) of the photons couples to their orbital AM due to the
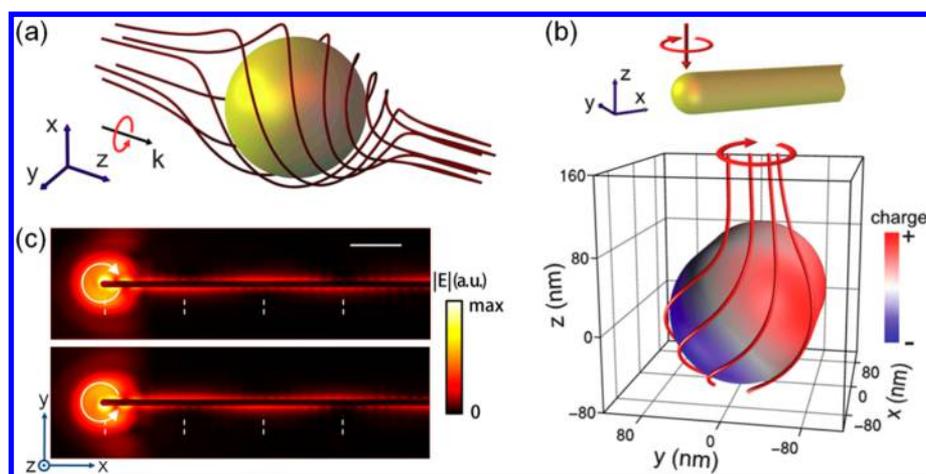
Figure 15. (a) A strong SOI in the scattering of circularly polarized photons on a Au nanosphere, revealed by the twisted trajectories of light. (b) The SOI on a Au NW tip for the excitation of SPs on the NW using circularly polarized photons. (Top) Schematic illustration. (Bottom) The distributions of surface charges and the streamlines of the orbital momentum density $\mathbf{p^o}$. (c) Sectional view of the electric field distributions in the $x-y$ plane across the center of the NW under excitation with opposite circular polarizations denoted by the circular arrows. The scale bar is 1 μm. The white dashed lines mark the nodes in the periodic zigzag patterns. The radii of the Au nanosphere and the Au NW are both 80 nm. The refractive index of the surrounding dielectric medium is 1.5. The wavelength is 785 nm. Reprinted with permission from ref 120. Copyright 2016 American Physical Society.

conservation of the total AM, which leads to a spin-dependent spatial deviation. This SOI effect of light is usually extremely weak in dielectric materials, but recent studies show the SOI resulted phenomena are significant in metal structures.[117] The strong SOI of light in a metal structure originates from the large gradient of the dielectric permittivity on the metal-dielectric interface and can be utilized to realize spin-dependent propagation of plasmons on metal NWs, as shown in Figure 15.[120]

The strong SOI of light in a metal structure can be clearly revealed in the scattering of a circularly polarized plane wave by a metal nanosphere, as shown in Figure 15a. The orbital AM of the electromagnetic field at a certain position $\mathbf{r}$ is revealed by the streamlines of the orbital momentum density $\mathbf{p^o}$,[120] as the orbital AM density is $\mathbf{r} \times \mathbf{p^o}$. Figure 15a shows the streamlines of $\mathbf{p^o}$ for a gold nanosphere with a radius of 80 nm illuminated by a circularly polarized plane wave of 785 nm wavelength. The incident light carries no orbital AM, since $\mathbf{p^o}$ is uniformly forward in the z direction. In the near field of the nanoparticle, the streamlines are drastically twisted with azimuthal components and form a vortex, which implies an efficient conversion from the spin AM of the incident photons to the orbital AM. A similar enhanced photonic SOI process can also occur in a metal NW, with its end illuminated by a circularly polarized Gaussian beam. In this case, drastically twisted trajectories of $\mathbf{p^o}$ are also observed as shown in Figure 15b, which indicates a strong SOI process on the tip of the NW. The twisted trajectories with transverse components in the $x-y$ plane lead to spin-dependent directional coupling of propagating SPs on the NW (Figure 15c, top), with the field distribution extending to a periodic zigzag pattern. For an excitation beam with opposite circular polarization, the field distribution is reversed as the mirror image (Figure 15c, bottom). Consequently, the incident photons with different spin AMs are separated into different spatial trajectories due to the SOI of light on the NW tip.
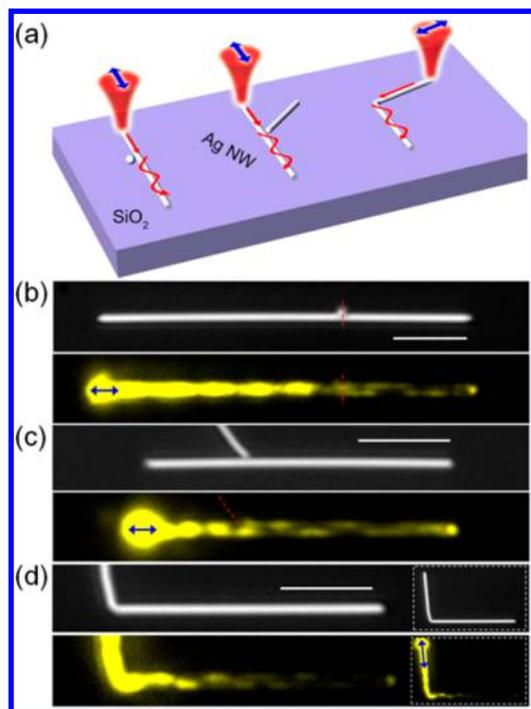
5.4. Mode Conversion

As discussed in sections 5.1 and 5.2, the zigzag and chiral propagation routes of plasmons on NWs, which are important

for constructing nanophotonic devices, are results of the superpositions of different plasmon modes with proper components and phase relations. The components of plasmon modes are usually tuned by the polarization of the incident laser beam, which is not suitable for more practical applications. To realize advanced functions, it is important to directly and locally control the components of plasmon modes in the NW by realization of mode conversions.

Since the TM_0 mode and HE_1 mode have different lateral symmetries, the mode conversion can be realized by introducing local structural symmetry breaking. Figure 16 shows three kinds of NW-based structures with structural symmetry breaking, including a nanoparticle-NW structure, a branched NW, and a bent NW, which can realize the conversion between the plasmon modes. In experiments, these structures can be prepared by depositing chemically synthesized Ag NWs and nanoparticles on a glass substrate, where the concerned structures are occasionally formed or elaborately constructed by using a micromanipulator.[18,40] The structures with symmetry breaking can also be prepared using nanofabrication techniques.[121]

The mode conversion processes in these symmetry-broken structures are schematically shown in Figure 16a and experimentally demonstrated in Figure 16 (panels b−d). The experimental images of the plasmon near field were obtained by the QDs based fluorescence imaging technique. As schematically shown in Figure 16a, only the TM_0 mode in the NW with a symmetric field distribution is launched by a linearly polarized laser beam focused on the end of the NW, with the polarization parallel to the NW. The field distribution changes into a zigzag shape after the local symmetry-breaking positions, which implies the coexistence of two modes in the NW with a new component of HE_1 mode generated by the mode conversion. This mode conversion process is demonstrated in all three experimental structures by the QD fluorescence images in Figure 16 (panels b−d), which show the changes of the near-field distributions from symmetric patterns to zigzag. These mode conversion processes are important for designing and building plasmonic circuits based on NW networks. By

Figure 16. (a) Schematic illustration of the mode conversions in three NW-based structures. (b–d) The optical images (top) and QD fluorescence images (bottom) of (b) nanoparticle-NW, (c) branched NW, and (d) bent NW structures. The scale bars are 5 μm. Reprinted with permission from ref 40. Copyright 2014 Nature Publishing Group.

elaborately controlling the mode conversion process, the routing and switch function can be actively controlled, which will be discussed in section 8.1.

5.5. Loss and Propagation Length

5.5.1. Losses of Plasmons on Metal Nanowires. SPs propagating on metal NWs suffer losses due to the inevitable ohmic damping of the metal that attenuates the intensity of the near field along their paths. In addition to ohmic loss, the propagation loss of SPs on NWs may also be caused by leaky radiation from the leaky plasmon modes, and the scattering by surface roughness in realistic structures, as schematically illustrated in Figure 17. All these loss mechanisms contribute
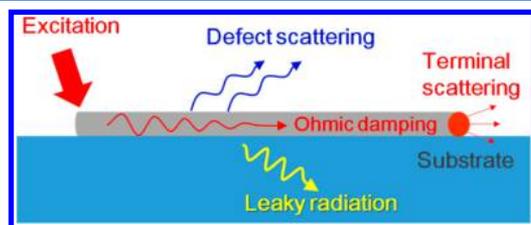
Figure 17. Losses of SPs propagating along a metal NW.

to the damping of the SP propagation and can be mathematically included by the imaginary part of the plasmon wave vector $k_{\parallel}$ with the field intensity

$$I_{SP}(z) = I_0 \, e^{-2\text{Im}(k_{\parallel})z} \qquad (2)$$

where I_0 is the initial intensity. The propagation length of SPs on NWs can then be defined as $L_{SP} = 1/[2\text{Im}(k_{\parallel})]$, which is the

propagation distance for the intensity decaying to 1/e of the original intensity.

Ohmic damping is usually the major reason for the plasmon loss and originates from the inherent absorption of the metal due to both interband and intraband transitions. The energy acquired by these transitions is further converted into heat via electron–electron, electron–phonon, and electron–surface scattering.[122] The electron–phonon scattering rate can be decreased at low temperature, reducing the damping of the propagating SPs and resulting in a longer propagation length.[123]

The ohmic damping rate is proportional to the electric field in the metal, so it is related to the confinement of the plasmon modes, which can be characterized by the effective mode area.[38,44,46,124−126] This determines the trade-off between propagation length and mode confinement as discussed in section 3. In general, the fundamental mode in NWs of various geometries (TM$_0$ mode in the cylindrical NW) is more confined than other higher-order modes, so it suffers higher propagation loss. The confinement of different plasmon modes varies with the wavelength and the NW diameter. Therefore, the ohmic loss depends on the wavelength and the NW diameter.[44,46,49,124] Longer wavelength and larger diameter correspond to smaller ohmic loss. The attempts to increase the confinement of the plasmon mode, for example by increasing the refractive index of the substrate or coating, inevitably decrease the propagation length of the modes.[45,49,124]

As discussed in section 3.1, the plasmon modes can be leaky (e.g., the H$_2$ mode in a NW deposited on a substrate for low frequency) and radiate energy along the propagation, which introduces further loss. To prevent the leaky radiation, an additional thin layer (∼30 nm) of high refractive index can be inserted between the NWs and the substrate to increase the wave vector of the SPs to be sufficiently larger than that of light in the substrate.[44] If the substrate or environment is absorptive at the SP frequencies, additional damping can arise from the absorption, leading to further damping of the SPs.[29,45]

Moreover, the scattering by surface roughness, defects, or bending corners of NWs also leads to plasmon loss. Taking lithographically fabricated nanowaveguides as an example, the scattering loss is mainly due to the roughness of the polycrystalline structures.[29,36] In addition, when the NW is bent sharply, scattering loss occurs at the bending corner due to geometrical symmetry breaking, and the SPs can be coupled to light at the corner position.[127]

5.5.2. Measuring Propagation Length. The most straightforward method to reveal the propagation loss and measure the propagation length of SPs on the NW is directly visualizing the electric field distribution through various techniques, such as imaging by SNOM, fluorescence, leaky radiation (as will be seen in section 5.8),[49,128] and transient absorption.[129,130] By fitting the measured intensity along the NW with an exponential decay, the propagation length can be obtained. Figure 18 shows two examples of near-field imaging of NW SPs based on fluorescence, including the two-photon fluorescence imaging method[131] (Figure 18a) and the fluorescence bleaching method[132] (Figure 18b). In these measurements, the NWs were covered by a polymer layer containing dye molecules, whose fluorescence can reveal information on the SP near field. In Figure 18a, the two-photon fluorescence intensity directly reveals the SP field distribution because the fluorescence intensity is proportional to the square of the SP near-field intensity. The measured two-
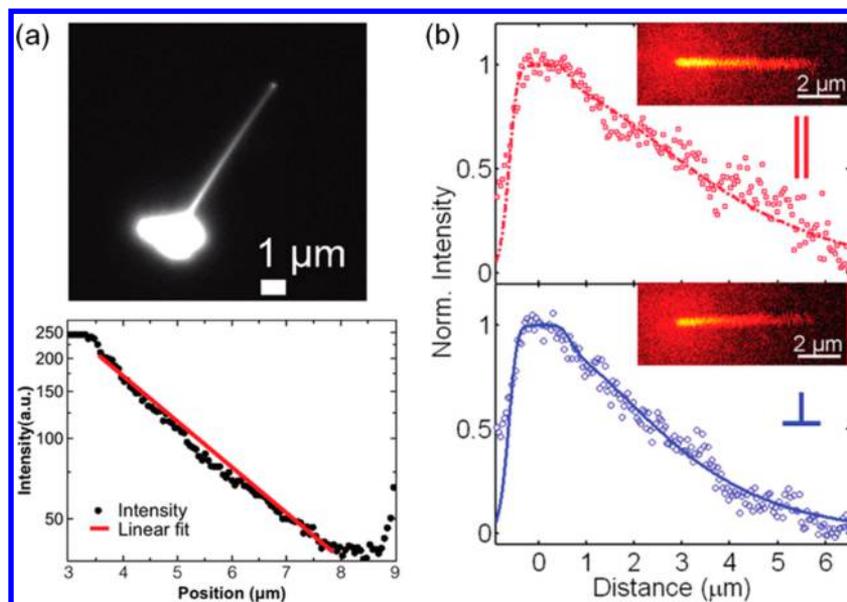
Figure 18. (a) (Top) Image of two-photon fluorescence excited by SPs propagating along a Ag NW. (Bottom) Two-photon fluorescence intensity in the top panel as a function of the position along the NW. Reprinted from ref 131. Copyright 2012 American Chemical Society. (b) Width-averaged intensity line sections and fits obtained from the fluorescence difference images shown in the insets for excitation polarization parallel (upper) and perpendicular (lower) to the Au NW. The difference images were obtained by subtracting the fluorescence image after the photobleaching by propagating SPs from the original fluorescence image. Reprinted from ref 132. Copyright 2010 American Chemical Society.

photon fluorescence image clearly reveals the attenuation of the SP intensity. The propagation length can be obtained by fitting the distribution of the intensity I on the NW using $I = I_0^2 e^{-2z/L_{SP}}$. In Figure 18b, the propagating plasmons on the NW cause photobleaching of the fluorescent polymer and the degree of bleaching is correlated with the near-field intensity. Higher field intensity leads to stronger photobleaching and therefore weaker fluorescence. Subtracting the confocal fluorescence image measured after photobleaching from the fluorescence image obtained before photobleaching provides an image of the field distribution of the SPs, as shown in the inset of Figure 18b. The damping of the SP propagation can be clearly seen from the difference images for both excitation polarizations parallel and perpendicular to the NW. The propagation lengths for both polarizations can be obtained by fitting the corresponding intensity decay along the NW using $I = I_0 e^{-z/L_{SP}}$.

The propagation length can also be extracted by measuring the SP emission intensity at the NW end as a function of the propagation distance. In experiments, this distance can be precisely controlled by tuning the position of the point source for exciting SPs. For example, by using a tapered nanofiber (Figure 9) at different positions along the NW to excite the SPs, the emission intensity as a function of propagation distance can be measured, as shown in Figure 19.[127,133−135] In addition, emitters coated on a NW excited by a focused laser beam can also serve as the point source, with the excitation positions determined by the laser spot.[136] The dependence of the emission intensity on the propagation distance can also be obtained by statistically measuring the SP emission intensities of NWs with similar diameter but different lengths.[45] In these methods, due to the propagation loss of the SPs, the emission intensity decays exponentially with respect to the propagation distance as $e^{-z/L_{SP}}$. By fitting the emission intensity using the exponential form, as shown in Figure 19b, the SP propagation length can be obtained.
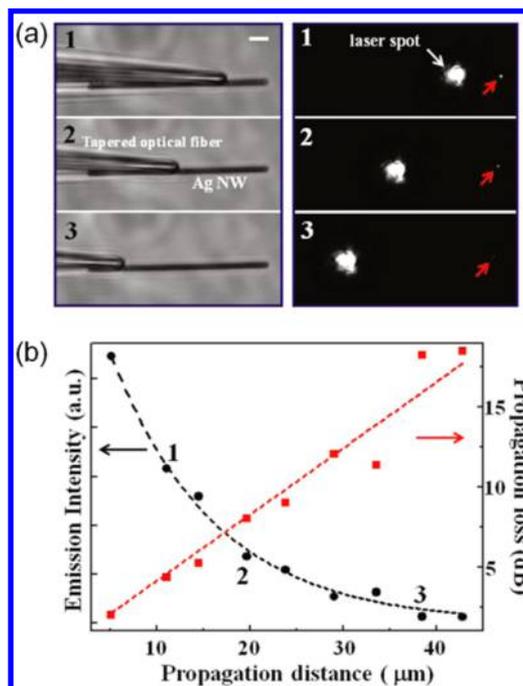
Figure 19. (a) Measuring propagation loss by exciting the SPs at different positions of a Ag NW using an optical nanofiber. The scale bar is 5 μm. (b) Emission intensity at the NW end and propagation loss for different propagation distances. Reprinted from ref 127. Copyright 2011 American Chemical Society.

The spectrum of SP emission at the NW end excited by white light contains information on propagation length for a wide range of frequencies. The spectrum is modulated by the Fabry-Pérot resonances (Figure 20a), and the modulation depth varies with both the wavelength and NW length.[36] The relative modulation depth $\Delta I/I_{min}$ is determined by $\Delta I/I_{min} = 4RA/(1-RA)^2$, where R is the reflectivity of the SPs at the end
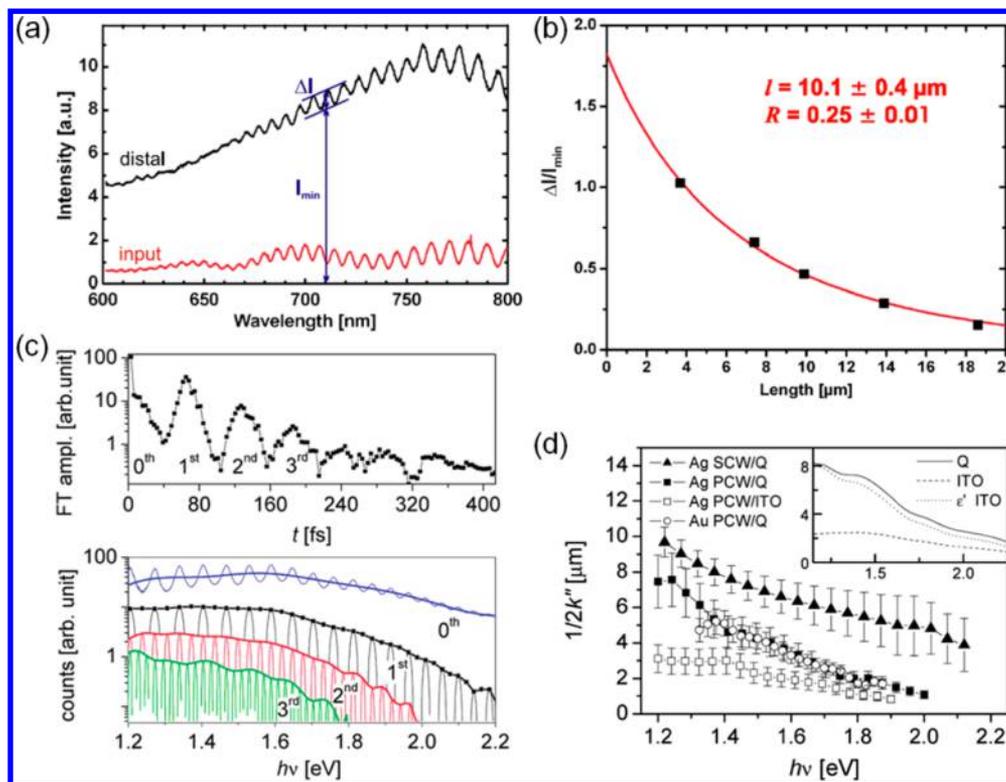
Figure 20. (a) Spectra recorded at the two ends of a Ag NW. The definition of modulation depth $\Delta I/I_{\min}$ is demonstrated by arrows. (b) Modulation depth at the wavelength 785 nm versus NW length. (c) (Top) Fourier transform amplitude of the spectrum from the distal end of a 5 μm long Ag NW. (Bottom) Inverse Fourier transform function for band-pass filtering the individual peaks in the top panel, marked by the corresponding peak number. (d) Propagation lengths obtained from Fourier analysis for Au and Ag NWs on quartz (Q) and ITO. SCW and PCW stand for single-crystalline NWs and polycrystalline NWs, respectively. Inset shows the propagation lengths calculated from the analytical NW dispersion. Different substrates are modeled by effective permittivities of the surrounding medium (ε' ITO, assuming a real permittivity). (a and b) Reprinted with permission from ref 36. Copyright 2005 American Physical Society. (c and d) Reprinted from ref 29. Copyright 2012 American Chemical Society.

of the NW, $A = e^{-L/L_{\mathrm{SP}}}$ is a parameter containing the propagation length L_{SP} and the NW length L. As a result, the reflectivity R and the propagation length L_{SP} at a certain frequency can be extracted by analyzing the measured values of $\Delta I/I_{\min}$ from NWs with different lengths. As shown in Figure 20b, the relative modulation depths at the wavelength of 785 nm from five NWs with diameters around 110 nm and different lengths were fitted using the equation above, from which a fitting value of the propagation length of 10.1 ± 0.4 μm was obtained.

By applying a Fourier transform approach to the spectra of the emitted light from the NW ends, the propagation length of NW SPs can also be extracted. The spectrum of the scattered light from the NW end was first transformed to the time domain (Figure 20c, top).[29] The resulting spectrum contains a series of peaks which imply round-trip propagation of a SP pulse as it is reflected at the two ends of the NW. Then, these separated peaks were transformed to the energy-dependent amplitudes with an inverse Fourier transform (Figure 20c, bottom).[137] The ratio of amplitudes of successive orders yields the information about the SP propagation length and the end face reflectivity of the NW. Figure 20d shows the propagation lengths extracted from the Fourier transform method. As can be seen, the propagation lengths decrease with the increase of the energy, which is caused by the tighter confinement of SPs of higher energy leading to larger loss. Figure 20d also shows that Ag NWs on ITO suffer larger propagation loss than the ones on quartz. The simulation results for NWs on quartz, ITO, and

ITO without considering absorption, as presented in the inset of Figure 20d, indicate that the absorption of the ITO plays a key role in reducing the propagation length.

We summarize the SP propagation lengths measured by different methods in Table 2.

If a metal NW is bent, additional scattering loss due to the bending can be introduced, which can also be quantitatively measured. The loss due to the bending of the NW can be analyzed by exciting the SPs using a fiber taper. Figure 21 shows the experimental measurement of the scattering loss of a bent NW. The Ag NW was bent using a tapered tip, as shown in Figure 21a. The SPs on the NW were excited by a tapered nanofiber, and the emission intensities from the NW end with different bending radii were recorded (Figure 21b). The intensity of the emission at the end of the NW decreases when the bending of the NW gets sharper, which implies a sharper corner of the NW leads to a larger scattering loss. The emission intensity from the NW end involving bending loss can be written as

$$I_{\mathrm{e}} = I_0 \, e^{-L/L_{\mathrm{SP}}} \, e^{-\alpha L_{\mathrm{bending}}} \qquad (3)$$

where I_0 is the initial input intensity, L is the NW length, L_{SP} is the SP propagation length without bending, L_{bending} is the length of the bending section, and α is the attenuation coefficient due to bending, which depends on the curvature radius. With the propagation length L_{SP} for the NW without

Table 2. Propagation Lengths of NW SPs Measured by Different Methods

wavelength	material	L_{SP}	diameter	excitation polarization	method[a]	ref
532 nm	silver	6.77 μm	260 nm	—	(d)	ref 133
		2.76 ± 0.30 μm	340 ± 20 nm	parallel (H$_2$ mode)	(a)	ref 49
		~2.7 μm	185 nm	parallel (H$_2$ mode)	(a)	ref 128
		~3.1 μm	224 nm	parallel (H$_2$ mode)	(a)	ref 128
	gold	1.9 ± 0.4 μm	average 400 nm	parallel	(b)	ref 132
		1.7 ± 0.2 μm		perpendicular	(b)	
633 nm	silver	4.9 ± 1.6 μm	90 ± 15 nm	parallel	(e)	ref 29
		10.56 μm	260 nm	—	(d)	ref 133
		3.67 ± 0.46 μm	340 ± 20 nm	parallel (H$_2$ mode)	(a)	ref 49
	gold	—	—	—	—	—
640 nm	silver	~2.8 μm	185 nm	parallel (H$_2$ mode)	(a)	ref 128
		3.3 μm	224 nm	parallel (H$_2$ mode)	(a)	
	gold	—	—	—	—	—
650 nm	silver	5.0 ± 1.6 μm	90 ± 15 nm	parallel	(e)	ref 29
	gold	3.4 μm	210 nm	—	(d)	ref 134
700 nm	silver	5.6 ± 1.2 μm	90 ± 15 nm	parallel	(e)	ref 29
	gold	—	—	—	—	—
740 nm	silver	10.3 ± 2.8 μm	average 70 nm	parallel	(b)	ref 131
		6.1 ± 1.1 μm	90 ± 15 nm	parallel	(e)	ref 29
	gold	—	—	—	—	—
760 nm	silver	—	—	—	—	—
	gold	2.3 ± 0.4 μm	average 120 nm	—	(b)	ref 131
770 nm	silver	6.3 ± 1.0 μm	90 ± 15 nm	parallel	(e)	ref 29
	gold	1.35 ± 0.54 μm	56 ± 10 nm	parallel	(c)	ref 130
785 nm	silver	10.1 ± 0.4 μm	110 ± 15 nm	parallel	(e)	ref 36
		12 ± 1.0 μm	average 70 nm	—	(b)	ref 131
		6.34 ± 0.51 μm	340 ± 20 nm	parallel (H$_2$ mode)	(a)	ref 49
		6.5 ± 0.9 μm	90 ± 15 nm	parallel	(e)	ref 29
	gold	3.1 μm	100 nm	—	(d)	ref 134
		3.2 μm	120 nm			
		3.8 μm	180 nm			
		4.9 μm	210 nm			
		6.5 μm	270 nm			
800 nm	silver	—	—	—	—	—
	gold	11.3 ± 3.1 μm	width 600 ± 220 nm, height 380 ± 140 nm	parallel	(c)	ref 129
		12.3 ± 4.1 μm		perpendicular		
810 nm	silver	6.9 ± 0.8 μm	90 ± 15 nm	parallel	(e)	ref 29
	gold	2.8 ± 0.3 μm	average 120 nm	—	(b)	ref 131
850 nm	silver	17.5 ± 3.0 μm	average 70 nm	—	(b)	ref 131
		7.2 ± 0.8 μm	90 ± 15 nm	parallel	(e)	ref 29
	gold	—	—	—	—	—
860 nm	silver	—	—	—	—	—
	gold	3.6 ± 0.5 μm	average 120 nm	parallel	(b)	ref 131
980 nm	silver	9.0 ± 0.7 μm	90 ± 15 nm	parallel	(e)	ref 29
		13.27 μm	260 nm	—	(d)	ref 133
	gold	5.6 μm	210 nm	—	(d)	ref 134

[a](a) Leaky radiation imaging, (b) fluorescence imaging, (c) transient absorption imaging, (d) measuring emission intensity, and (e) measuring emission spectra.

bending (see Figure 19), the bending loss for different bending radii can be calculated using eq 3 (Figure 21c).

5.6. Group Velocity

Light in vacuum is dispersionless as $\omega = ck$ (straight line in Figure 2b), with the group velocity equal to the phase velocity c. While in a metal NW, the SP dispersion relation curves are located at the right side of the light line (curves in Figure 2b). The group velocity of a plasmon mode of a certain frequency can be obtained from the tangent of the plasmon dispersion relation curve. It can be seen from Figure 2b that the group velocity of SPs is slower than that of light in vacuum.

The experimental measurements of the group velocity of the SPs are mainly based on the analysis of the characteristic emission spectra from the NW ends (as shown in Figure 20a). When the SPs on a metal NW were excited by a white light source, the emission spectrum from the NW end shows fringes originating from Fabry-Pérot cavity modes.[100] The group velocity of the SPs on the NW can be calculated from the modulated emission spectrum by

$$v_g = 2L\frac{\Delta\omega}{2\pi} = 2Lc\frac{\Delta\lambda}{\lambda^2} \tag{4}$$
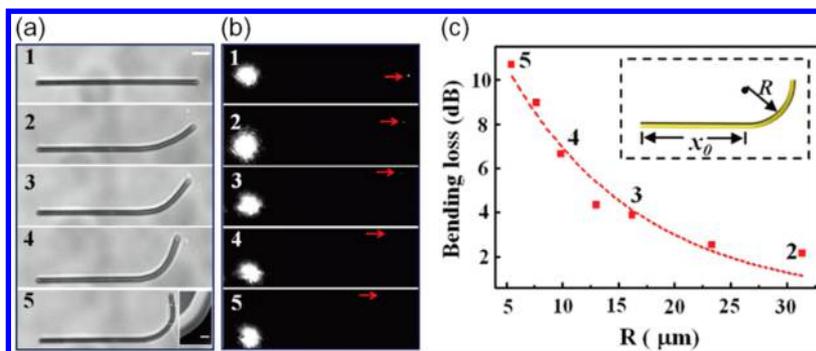
Figure 21. (a) Optical images for a Ag NW with different bending radii. The scale bar is 5 μm. (b) Optical images corresponding to (a) for excitation of the SPs by a tapered nanofiber. The spots of the emitted light at the bent end of the NW are indicated by the red arrows. (c) Bending loss as a function of bending radius. Inset: geometry of the bent wire. Reprinted from ref 127. Copyright 2011 American Chemical Society.
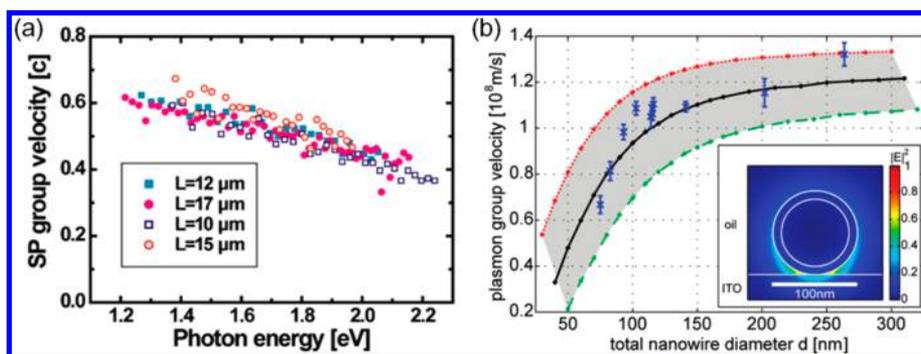
Figure 22. (a) Group velocities of propagating SPs on different Ag NWs obtained by applying eq 4 to the measured spectra. Reprinted from ref 100. Copyright 2008 American Chemical Society. (b) Diameter dependence of SP group velocity in Ag NWs. Blue crosses indicate experimental results. Simulation results without a corrosion layer and with a 5 nm and a 10 nm corrosion layer of silver sulfide are plotted by red, black, and green curves, respectively. (Inset) Two-dimensional near-field intensity distribution of the fundamental plasmon mode for a Ag NW immersed in index-matching oil on a 200 nm thick ITO layer on top of glass. The NW diameter is 100 nm, including a 10 nm silver sulfide corrosion layer. Reprinted from ref 140. Copyright 2012 American Chemical Society.

where L is the NW length, $\Delta\omega = 2\pi c\Delta\lambda/\lambda^2$ is the frequency interval between two neighboring peaks in the emission spectrum, and λ is the central wavelength between the two peaks.[138,139] Figure 22a shows the SP group velocities obtained by this method. It demonstrates that the group velocity of SPs is well below the light speed and decreases monotonically from $0.6c$ at 1.2 eV to $0.4c$ at 2 eV. Alternatively, the group velocity can be obtained by performing a Fourier-transform based algorithm for the emission spectra, which produces results consistent with the calculations using eq 4.[100]

Far-field interference induced spectral modulations can also be used to derive the group velocity of SPs on NWs.[131,140] In a typical measurement, a femtosecond pulsed laser beam was focused onto the end of a Ag NW to launch propagating SPs. Meanwhile, a reference pulsed beam was used to interfere with the reflected and emitted light from the input and output ends of the NW, respectively. By performing Fourier transform on the measured spectral interferograms of the reflected and emitted light, the temporal positions of reflection and emission signals relative to the reference pulse were reconstructed, from which the time difference Δt between reflection and emission pulses was obtained.[141] Further correction was carried out for Δt to offset the time delays due to the geometrical path difference of the reflected and emitted light caused by the different detection positions. The group velocity of the SPs was given by the NW length L and the corrected Δt as $L/\Delta t$. It was found that the group velocity of the SPs is highly dependent on the NW diameter (Figure 22b). When the diameter is smaller

than 100 nm, the group velocity decreases drastically with decreasing diameter. This trend was well reproduced by simulations considering a corrosion layer (silver sulfide, 5 nm in thickness) caused by the reactivity of silver at ambient condition.

5.7. Nanowire Terminal Emission

The propagating SPs on the NW can be converted to photons by scattering at the NW end, where the structural symmetry is broken. Figure 23a shows the emission characteristics of the TM_0 mode and HE_1 mode for a Ag NW of 200 nm radius in a homogeneous dielectric medium.[142] The emission fields maintain the polarization symmetry of the two modes shown in Figure 3a. For the TM_0 mode, the emission field is radially polarized with an axial symmetry, and for the HE_1 mode, the emission field is linearly polarized. In accordance with the theory of vector beams, the radial polarization implies a singularity in the beam center. Therefore, the emission of the TM_0 mode is dark in the center, with the maximum intensity at about $30°$ from the NW axis. In contrast, the maximum emission intensity of the HE_1 mode is along the NW with a small spreading angle.

When a NW supports multiple plasmon modes, the emission at the NW end is the superposition of the emissions from the individual modes described in Figure 23a. The field distribution of the emission from the simultaneously excited TM_0 and HE_1 modes in a NW is asymmetric due to the different symmetries of the two modes, similar to that discussed for the zigzag
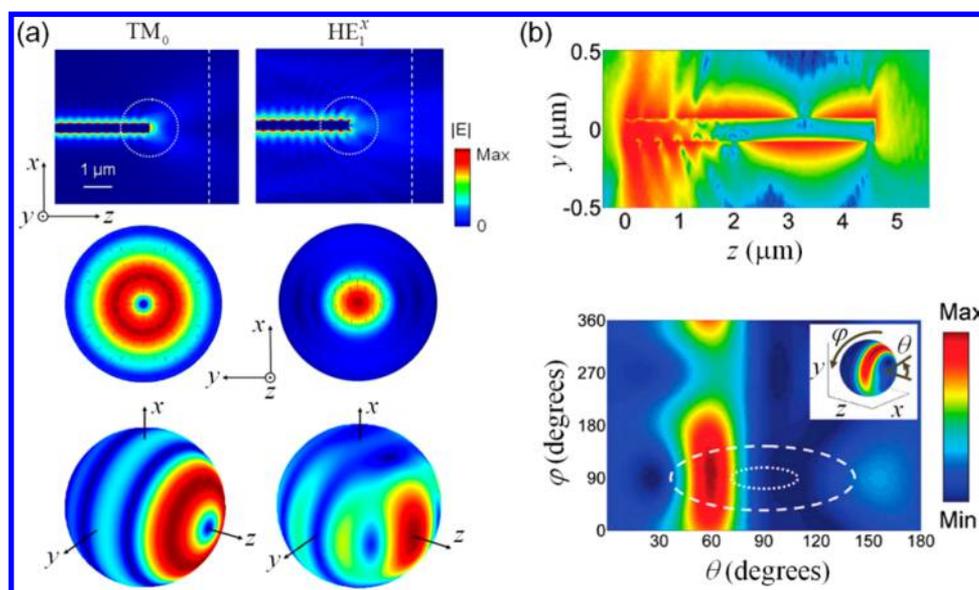
Figure 23. (a) Emission characteristics of the TM_0 and HE_1 modes for a Ag NW in a homogeneous dielectric environment. (Top) Electric field amplitudes on the cut plane across the axis of the wire. (Middle) Electric field on the cut plane 2 μm away from the output terminal marked by dashed lines in the top row. (Bottom) Far-field angular emission distributions transformed from the spheres marked by the dot circles in the top row. The NW radius is 200 nm. The excitation wavelength is 633 nm. The refractive indices of the surrounding medium and silver are 1.56 and 0.0562 + 4.2776i, respectively. Reprinted with permission from ref 142. Copyright 2013 Chinese Physical Society and IOP Publishing Ltd. (b) (Top) Poynting intensity distribution around a Ag NW. (Bottom) Spatial distribution of the emission from the wire end. The inset shows the corresponding angular distribution on the integration sphere. The angles θ and φ are defined in the inset. The z axis corresponds to $\theta = 0°$, and the x axis corresponds to $\varphi = 0°$. Reprinted from ref 143. Copyright 2009 American Chemical Society.

pattern on the NW. As shown in Figure 23b, for a Ag NW excited by light polarized parallel to the NW, the intensity distribution around the NW shows a zigzag shape (top panel of Figure 23b), indicating the excitation of the TM_0 mode and one HE_1 mode. The angular distribution of the light emitted from the NW end demonstrates that the emission intensity is azimuthally asymmetric (φ direction). The intensity peak is at an angle around $\theta \sim 60°$ (bottom panel of Figure 23b) with respect to the NW axis. More calculations show that, for NWs with different diameters smaller than 200 nm, the light emission always peaks in the range of $\theta \sim 45-60°$.[143]

The superposition of the emissions from multiple plasmon modes also determines the polarization of the emitted light at the NW end. The emission of the HE_1 mode is linearly polarized with good directionality. The superposition of emissions from the two degenerate HE_1 modes with the same amplitude and a $\pi/2$ phase difference therefore has circular polarization. This is demonstrated by the emission of a NW excited by a laser beam with a polarization angle of 45° with respect to the NW, where the two degenerated HE_1 modes are generated with the required $\pi/2$ phase difference as discussed in section 5.2. Figure 24a shows the calculated degree of circular polarization C in a vertical plane 200 nm away from the output end of the NW. The degree of circular polarization C is defined as $C = 2\langle E_x E_y \sin(\delta_x - \delta_y)\rangle/(\langle E_x^2\rangle + \langle E_y^2\rangle + \langle E_z^2\rangle)$, where < > denotes time average, and $\delta_x - \delta_y$ is the phase difference between the two transverse electric field components E_x and E_y. As shown in Figure 24a, the C value of the emission can be as high as 0.9. The asymmetry of the distribution is due to additional emission from the TM_0 mode excited by the laser. The high degree of circular polarization of the optical field at the output end of the NW is further confirmed by the figure of merit in Figure 24b, where the figure of merit is defined as $f = IC^2$ ($I = |\mathbf{E}(\mathbf{r})|^2/|\mathbf{E}_0(0)|^2$, and $\mathbf{E}_0(0)$ is the incident electric field
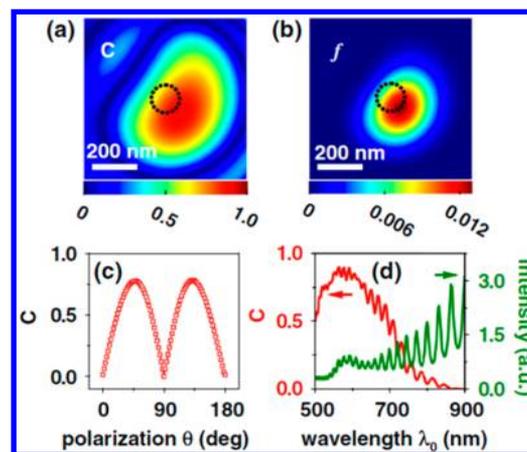
Figure 24. (a and b) Calculated maps of (a) degree of circular polarization C and (b) figure of merit f in a vertical plane 200 nm beyond the distal end of a Ag NW. The radius of the NW is 60 nm, and the length is 5.0 μm. The wavelength of the incident laser light is 632.8 nm, and the polarization angle is 45° relative to the NW. The dotted black circles indicate the cross section of the NW. (c and d) C at the center of (a) on the symmetric axis of the NW as a function of (c) incident polarization angle θ and (d) vacuum wavelength λ_0. The transmission spectrum (green) is also shown in (d). Reprinted with permission from ref 70. Copyright 2011 American Physical Society.

at the origin). The polarization state of the emission depends strongly on the polarization angle of the linearly polarized incident light, since the polarization angle determines the relative intensity of the multiple plasmon modes. The value of C reaches its maximum when the polarization angle θ is 45° and 135° ($\theta = 0$ is along the NW), as shown in Figure 24c. Wavelength scanning shows that the emitted light over a wide spectral range can maintain a high C (Figure 24d), which makes
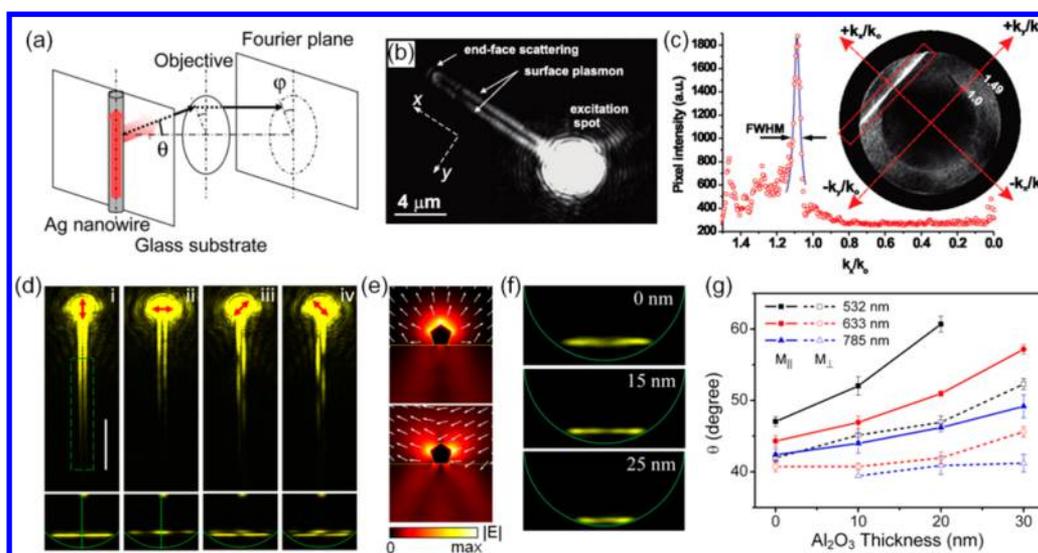
Figure 25. (a) Schematic illustration of the Fourier imaging method. (b) Intensity distribution in the image plane showing the excitation spot (saturated area), the leaky radiation of SPs along the Ag NW, and the SP scattering at the NW end. The excitation wavelength is 780 nm, and the polarization is parallel to the NW. (c) Wave vector distribution obtained by Fourier imaging. The SP mode is recognized as a bright line at a constant k_x/k_0 value, here 1.05. A cross section along the k_x/k_0 axis is also displayed (red dots). The blue solid line is a Lorentzian fit to the data. (d) Leaky radiation images (top) and corresponding Fourier images (bottom) for a Ag NW under different polarizations of excitation light. The red arrows indicate the polarization directions of the incident laser light with a 532 nm wavelength. Fourier images are obtained from the area marked by a green dashed rectangle in (i). The green circles in the Fourier images represent the maximum radiation angle that can be collected by the experimental system. The scale bar is 5 μm. (e) Calculated electric field distributions of the longitudinal mode (top) and transverse mode (bottom) of SPs on a glass-supported Ag NW. The NW radius is 170 nm. The wavelength is 532 nm. (f) Fourier images for different thicknesses of the Al_2O_3 coating layer. (g) Radiation angles of the two modes as a function of Al_2O_3 thickness for excitation wavelengths of 532, 633, and 785 nm. The solid symbols and hollow symbols are the experimental means of five NWs for longitudinal mode and transverse mode, respectively. The lines are used as guides for the eye. (a and f) Reprinted with permission from ref 48. Copyright 2014 Wiley. (b and c) Reprinted from ref 51. Copyright 2011 American Chemical Society. (d, e, and g) Reprinted with permission from ref 49. Copyright 2016 Royal Society of Chemistry.

metal NWs a good candidate for broadband nanosources of circularly polarized light. It is noted that the geometrical shapes of the NW ends influence the emission direction and polarization, due to their influence on the intensity and the phase of the different plasmon modes.[71]

5.8. Leaky Radiation

For a substrate-supported NW, when the wave vector of the SP mode is smaller than the wave vector of light in the substrate (e.g., glass), this mode is a leaky mode, which radiates power into the substrate. The wave vector of SPs on the NW $k_\parallel$ and the wave vector of leaky radiation light in the substrate k_{photon} are related by the phase matching condition

$$\text{Re}(k_\parallel) = k_{photon} \sin \theta \tag{5}$$

where θ is the angle between the radiation direction and the normal of the substrate. This equation shows that the leaky radiation is toward well-defined directions, making metal NWs optical antennas of high directionality.

This leaky radiation can be captured to image the spatial distribution of SPs on NWs. The radiation direction and the wave vector of the SP mode can be measured by Fourier space imaging technique, as schematically shown in Figure 25a.[48] Considering the beating period of a leaky mode and a bound mode (e.g., H_2 mode and H_0 mode) can be measured by QD fluorescence imaging (see section 5.1), the wave vector of the bound mode can be extracted by combining these two imaging methods. In experiments, the radiation into the glass side is collected by using an oil immersion objective with a high numerical aperture. Due to the leaky radiation of the SPs, the whole NW is bright (Figure 25b), in contrast to the end

scattering for the bound modes and the imaging from the air side.[47,51] In the Fourier image, the leaky radiation from the NW is distributed in a straight line (Figure 25c), fulfilling eq 5 along the NW axis ($\varphi = 0$). The radiation angle for a thin NW is larger than that for a thicker NW, since the wave vector of SPs on a thinner NW is larger.

The leaky radiation and corresponding Fourier image depend on the polarization of the excitation light. Figure 25d (i and ii) show the leaky radiation images and corresponding Fourier images for laser polarization parallel and perpendicular to the NW, respectively.[49] As can be seen, both the intensity distribution of the leaky light along the NW and the Fourier image pattern are different for the two polarizations. For the Fourier imaging measurement, an aperture was used to block the excitation light and select the area as outlined by the dashed rectangle in Figure 25d (i) for Fourier imaging. The parallel and perpendicular polarizations excite two leaky SP modes, with the electric field shown in Figure 25e. These two modes correspond to the H_2 mode and H_3 mode in Figure 4. For simplicity, here we call them the longitudinal mode and the transverse mode, respectively. For the longitudinal mode, the bright line in the Fourier image has a minimum intensity in the center. While for the transverse mode, the bright line intensity in the center is maximum, and there are two symmetrically distributed nodes on the two sides. When the laser polarization is 45° or −45° with respect to the NW, both modes are excited. The superposition of these two modes leads to the zigzag distribution of the leaky radiation [Figure 25d (iii, iv)] due to the different lateral symmetry of the two modes. The two modes can be resolved in the Fourier images. The radiation angle for the transverse mode is smaller than that for the

longitudinal mode because the wave vector of the longitudinal mode is larger. When the polarization is changed from 45° to −45°, the leaky radiation image is changed to the mirror image.

By using a polarizer to analyze the polarization of leaky light, it was found that the SP radiation along the NW axis ($\varphi = 0$) keeps the polarization of the excitation light, that is, the leaky radiation of the longitudinal mode and the transverse mode is polarized parallel and perpendicular to the NW, respectively.[49] This property is determined by the mirror symmetry of the NW on the substrate with respect to the vertical plane across the central axis of the NW. The electric field on the mirror plane maintains the polarization of the excitation light, resulting in the polarization-maintaining behavior.

By depositing a layer of dielectric, for example Al_2O_3, onto the NW, the radiation angle θ is increased (Figure 25f). The radiation angle θ is increased from 44° for a bare NW to 50° and 56°, by adding Al_2O_3 with a thickness of 15 and 25 nm, respectively. The increase of the radiation angle is caused by the increase of the wave vector of the SP mode due to the increase of the effective refractive index of the surrounding media. Figure 25g shows the dependences of the radiation angles for the two modes on the wavelength and Al_2O_3 thickness. Since a shorter wavelength and a thicker Al_2O_3 thickness correspond to a larger wave vector of the SPs, the corresponding radiation angle is larger according to eq 5.

The leaky radiation of SPs is determined by the phase matching condition, so it is not limited to a glass substrate. For the composite structure of a Ag NW on a Ag film with Al_2O_3 as the dielectric spacer between them, the SPs on the Ag NW can radiate to the Ag film to generate SP waves propagating on the film surface along the directions decided by $\mathrm{Re}(k_{\parallel\text{-NW}}) = \mathrm{Re}(k_{\parallel\text{-film}}) \cos \theta$, where θ is the angle between the NW and the propagation direction of the SPs on the Ag film.[144] When laser light polarized parallel to the NW is incident onto the NW end, the scattering image shows that a bright spot appears at the other end of the NW (Figure 26a), indicating the excitation of propagating SPs. The electric field distributions were imaged by the QD fluorescence imaging technique. As shown in Figure 26b, in addition to the electric field distribution on the NW, periodic collimated beams appear at the two sides of the NW. The experimental phenomenon was reproduced by the simulation (Figure 26c). These collimated beams originate from the radiation of SPs on the NW. For laser polarization parallel to the NW, two plasmon modes in the NW radiate to the Ag film (Figure 26d), generating two SP waves on the film propagating along two different directions θ_{I} and θ_{II}. The interference of the two SP waves produces periodic collimated SP beams along the direction $\theta = (\theta_{\mathrm{I}} + \theta_{\mathrm{II}})/2$, as shown in Figure 26 (panels b and c). The direction angle θ of the collimated beams increases with the increase of the dielectric spacer thickness (Figure 26e). The periodicity d of the collimated SP beams is related to the effective refractive indices of the two modes n_{I}, n_{II} by $d = \lambda \sin \theta / (n_{\mathrm{II}} - n_{\mathrm{I}})$.

6. NANOWIRE-EMITTER COUPLING

6.1. Exciton−Plasmon Interaction between Emitters and Metal Nanowires

### 6.1.1. Introduction to Exciton−Plasmon Interaction.
The generation of strong, coherent interaction between individual quantum emitters (QEs) and photons is important for the realization of quantum information processing and quantum communication tasks. However, the large size
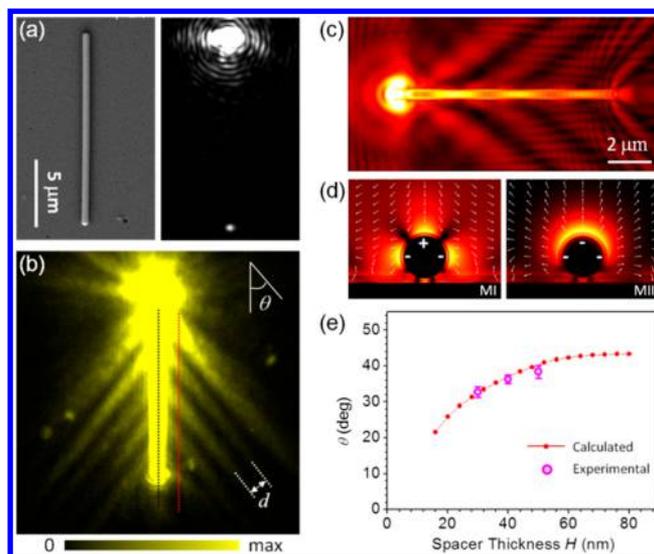
Figure 26. (a) (Left) SEM image of a Ag NW/Al_2O_3/Ag film sample with the NW radius R = 200 nm, the thickness of Al_2O_3 between the NW and the Ag film H = 40 nm, and the thickness of Al_2O_3 between the NW and the QD T = 30 nm. (Right) Optical image of the sample with laser light of 633 nm wavelength focused on the top end of the NW. (b) QD fluorescence from the sample that is excited by laser light focused on the top end of the NW. The angle relative to the NW θ and the period of the collimated SP beams d are indicated. (c) Simulated electric field |E| distribution at the surface of the top Al_2O_3 layer. (d) Simulated electric field distributions of the two leaky SP modes in the NW. Surface charges are schematically drawn. The sample parameters and wavelength in the simulations are the same as in (a). (e) Calculated and experimental values of the propagation angles of the collimated SP beams as a function of the spacer thickness. Reprinted from ref 144. Copyright 2015 American Chemical Society.

mismatch between optical wavelength and the dimension of single QEs determines that their interaction with light is typically weak. The interaction strength between QEs and photons is usually characterized by the spontaneous emission rate of the QEs that is inherently determined by the transition dipole moment and externally proportional to the surrounding optical LDOS according to Fermi's golden rule. The spontaneous emission rate of the QEs in a structured environment is enhanced due to the increased LDOS by a factor proportional to the ratio of the quality factor Q to effective volume V of the involved optical mode, which is known as the Purcell effect.[145,146] Two approaches have been proposed to enhance the interaction between an optical emitter and an optical mode by engineering high-Q and small-V cavities. One common strategy is to place the emitter inside a dielectric resonator with a high quality factor, where the interaction is strongly enhanced at the resonance frequency of the cavity due to the increased time that photons remain trapped in the corresponding optical state. However, the use of cavities places a restriction on the bandwidth and the size of the devices. Another strategy is to place the emitter at an optimal position of a plasmonic nanostructure where the strong field confinement can effectively reduce the volume of the optical mode. The broadband spectral response of the plasmonic nanostructure ensures the enhanced light-matter interaction for a wide spectral range.

The most well-known examples in plasmon-enhanced light-matter interactions are surface-enhanced Raman scattering/spectroscopy (SERS) and exciton−plasmon interaction be-
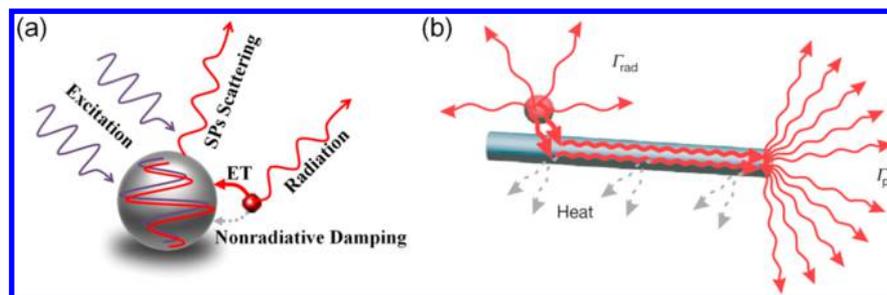
Figure 27. Schematic of exciton−plasmon interaction between single QEs and plasmonic nanostructures. (a) The interaction between a single QE and a metal nanosphere. The emitter excited by the incident light and the localized SPs can decay through nonradiative damping, direct far-field radiation, and exciting localized SPs. Here ET stands for energy transfer. (b) The coupling between a single QE and a metal NW waveguide. The excited QE can radiate into the far field or into propagating SPs followed by scattering at the NW end. It can also decay nonradiatively. Reprinted with permission from ref 20. Copyright 2007 Nature Publishing Group.
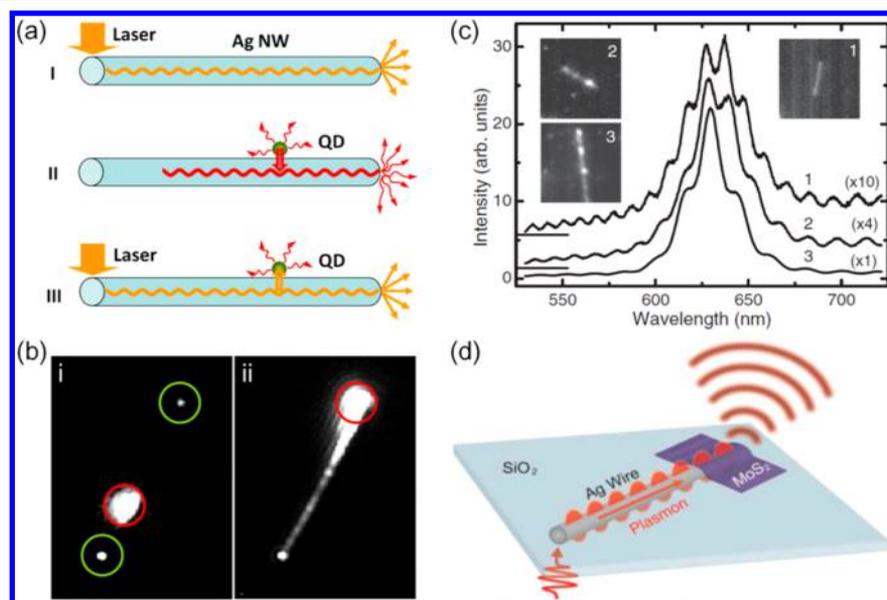

Figure 28. (a) Schematic illustration of the exciton−plasmon−photon conversion processes in a Ag NW-QD system. (b) Fluorescence images of the Ag NW covered with a film of QDs when the laser beam was focused on the midsection (left) and top end (right) of the wire. The positions of the excitation are marked by red circles. (c) QD emission spectra modulated by the Fabry−Pérot cavity modes measured for Ag NWs of different lengths. (d) Schematic of a single layer MoS₂−Ag NW coupling structure. (a and b) Reprinted from ref 160. Copyright 2009 American Chemical Society. (c) Reprinted with permission from ref 162. Copyright 2007 American Physical Society. (d) Reprinted from ref 163. Copyright 2014 Optical Society of America.

tween QEs and metal nanostructures.[147−152] Let us first give a brief overview of the interaction between a QE and a metal nanoparticle supporting localized SPs. The interaction can usually be separated into two steps, the excitation and the decay. First, the localized SPs induced by the incident light result in the enhancement of the local electromagnetic field intensity. The QE nearby the nanoparticle is excited by the incident light and by the localized SPs to generate excitons with an increased excitation rate. Second, the generated excitons can recombine through direct far-field radiative emission, the excitation of localized SPs on the nanoparticle via energy transfer, and the nonradiative damping including both the intrinsic nonradiative decay of the QE and the metal induced nonradiative damping (Figure 27a). The energy transfer from the QE to the metal nanoparticle is governed by dipole−dipole interactions, and the transfer rate is determined by the polarizations of the QE dipole and the plasmon mode, their separation distance, and the spectral overlap between the plasmon resonance and the emission of the QE.[153,154] The excited localized SPs can either decay nonradiatively owing to

internal damping of the nanoparticle or reradiate into a certain scattering SP mode. The plasmonic nanoparticle can be regarded as an optical nanoantenna, which transfers the emission from the QE to a certain far-field radiation mode.[155−157] As a result, the spontaneous emission rate of the QE is increased, and the fluorescence intensity is jointly affected by both the excitation enhancement and the emission modification.

Compared with metal nanoparticles, the plasmonic NWs enable the propagation of SPs in a well-defined direction along the NW. The transverse dimension of the propagating SPs can go below the diffraction limit, thus the emitters can interact with the propagating SPs with an extraordinary strength. Except for direct far-field radiation and nonradiative decay, the excited QE in the vicinity of the NW can recombine through the generation of SPs on the NW which propagate along the NW followed by scattering into photons at the ends of the NW (Figure 27b). QEs are excellent single-photon sources and can store quantum bits for extended periods,[158,159] making them promising interconnects between light and matter in integrated
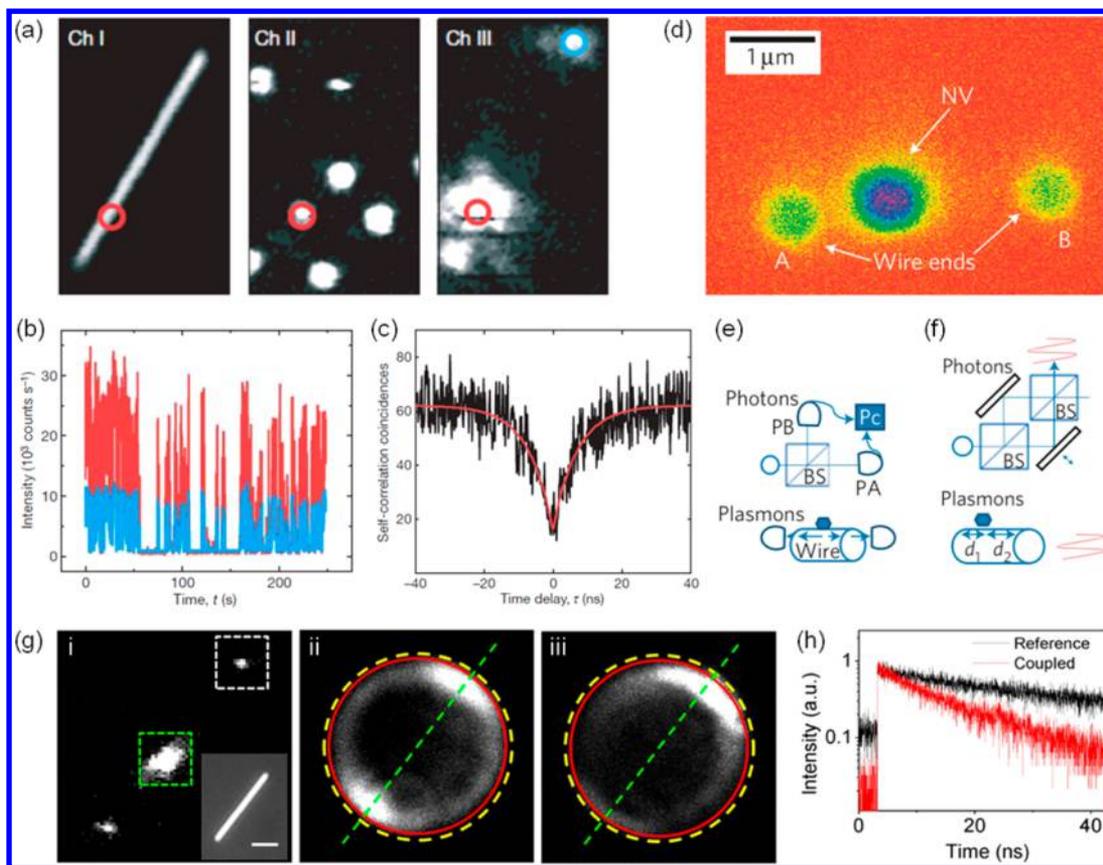
Figure 29. (a) Interaction between single QDs and a Ag NW. (Left) Optical image of a single Ag NW. (Middle) Fluorescence image of QDs. (Right) Excitation laser was focused on the QD marked by a red circle. The largest bright spot corresponds to the QD fluorescence, while two smaller spots correspond to SPs scattered at the NW ends. (b) Time traces of fluorescence counts (red curve) from the coupled QD and scattered light (blue) from the end of the coupled NW. Fluctuations are due to fluorescence blinking of single QD. (c) Second-order cross-correlation function between fluorescence of the QD and scattering from the NW end. (d) Fluorescence image of an optically excited single NV defect in a nanodiamond coupled to a Ag NW. (e) Sketch of Hanbury Brown-Twiss experiment for single photons (top) and single SPs (bottom) (particle-like). (f) Diagram showing single-photon (top) and single-plasmon self-interference (bottom) (wave-like). (g) (i) Fluorescence image showing the coupling of a single QD to a Ag NW coated with Al2O3 film of 10 nm thickness. The larger emission spot is the result of direct far-field emission from the QD near the NW, while two smaller spots correspond to the scattered SPs at the NW ends generated by the coupled QD. The inset is the bright-field optical image of the NW. The scale bar is 2 μm. (ii, iii) Fourier images obtained from the areas marked by the green and white dashed squares in (i), corresponding to the radiation from the (ii) coupled QD and the (iii) NW end scattering, respectively. The green dashed lines indicate the direction of the NW. The outer yellow dashed circle and inner red circle outline the maximum collection angle of the objective with NA = 1.49 and 1.4, respectively. (h) Fluorescence decay curves of an uncoupled reference QD (black line) and a QD coupled with a Ag NW coated with Al2O3 of 15 nm thickness (red line). (a−c) Reprinted with permission from ref 20. Copyright 2007 Nature Publishing Group. (d−f) Reprinted with permission from ref 21. Copyright 2009 Nature Publishing Group. (g and h) Reprinted from ref 88. Copyright 2015 American Chemical Society.

quantum information networks. Hybrid systems of QEs coupled to plasmonic NWs have received much attention as building blocks for future quantum plasmonic circuitry platforms.

The original framework for the interaction between a QE and a plasmonic NW was established by Chang et al.[19,39] Considering a cylindrical metal NW with a radius R, an oscillating dipole is positioned at a distance d from the center of the cylinder and the dipole moment is oriented perpendicular to the NW surface. Using the quasi-static approximation, they derived the analytical expressions for the spontaneous emission rate of the oscillating dipole into the fundamental SP mode of the cylinder Γ_{SP}, radiative emission rate into free space Γ_{rad}, and the nonradiative decay rate Γ_{nrad}, respectively. The spontaneous emission rate into plasmons can also be physically derived from Fermi's golden rule, and theoretical calculation shows that it scales as R^{-3}, where a factor of R^{-1} is due to the reduction in the plasmon group velocity and another factor R^{-2} is from the

small effective mode area. The efficiency of this dipole-plasmon coupling can be characterized by the enhancement factor of total decay rate (Purcell factor) and the SP quantum yield defined as $\xi = (\Gamma_{SP} + \Gamma_{rad} + \Gamma_{nrad})/(\Gamma_{rad,0} + \Gamma_{nrad,0})$ and $\eta = \Gamma_{SP}/(\Gamma_{SP} + \Gamma_{rad} + \Gamma_{nrad})$, respectively, where $\Gamma_{rad,0}$ and $\Gamma_{nrad,0}$ are the radiative and nonradiative decay rates of the oscillating dipole in free space. As $R \rightarrow 0$, the optimized $\Gamma_{SP}/(\Gamma_{rad} + \Gamma_{nrad})$ can exceed 10^3, indicating that the optical emission from the QE can be almost entirely converted into the plasmon mode at an optimal separation distance between the QE and the NW. However, the increase of the coupling strength achieved by letting $R \rightarrow 0$ is accompanied by a decrease in the SP propagation length. This limit can be circumvented by placing the oscillating dipole at the end of a metal NW with a nanotip having a paraboloidal profile, where the plasmon generation rate is increased due to the local field enhancement and the loss is decreased as the tip quickly expands to a larger radius. To further reduce the loss in order to meet the requirement of

transmitting quantum information over long distances, the plasmons on the NW could be out-coupled to the propagating mode of a dielectric waveguide.[78]

6.1.2. Exciton−Plasmon Interaction on NWs Covered with Emitter Films.
Compared to gold with high intrinsic loss in the visible and near-infrared spectral range, silver is a more suitable material for studying the exciton−plasmon interactions. To avoid the corrosion of silver in ambient air, the Ag NWs on the substrate can be protected by a thin layer of a dielectric film, which also functions as a spacer layer to separate the NWs from the later deposited emitters. In a hybrid system composed of a Ag NW and a film of QDs that are separated by a layer of SiO_2 of 25 nm thickness, the exciton−plasmon−photon coupling processes were systematically studied by using a focused excitation laser beam.[160] The incident light focused on the NW end can excite propagating SPs which partly couple out at the other end of the NW (process I of Figure 28a). The exciton−plasmon conversion (process II of Figure 28a) is demonstrated by the fluorescence emission at the two ends of the NW when only the QDs in the middle section of the NW are excited (Figure 28b, i). The propagating SPs generated by the incident laser beam on the NW end can excite the nearby QDs which partially convert their energy into far-field radiation (process III of Figure 28a). This process means that the near-field distribution of the propagating SPs on the NW is visible in the fluorescence image if the QD coverage is uniform (Figure 28b, ii). Using this method, Wei et al. demonstrated the polarization and environment-dependent electric field distributions of SPs on Ag NWs and the interference of SPs in branched NW networks.[17,18,70,113,161]

For the QDs coupled with chemically synthesized Ag NWs coated with a SiO_2 shell under wide field excitation, the emission intensity at the NW ends may become saturated with increasing NW length. This also indicates the existence of energy transfer from the excitons in QDs to plasmons on the NW.[162] Due to the reflections of the SPs at the NW ends, the emission spectra at the NW ends show Fabry-Pérot-type modulations (Figure 28c).

Because of the near-field enhancement effect, the fluorescence of optical emitters near the plasmonic NW shows clear enhancement. The fluorescence enhancement depends on the polarization of the excitation light for Ag NWs covered by a CdSe QD film.[164] The polarization of the fluorescence emission is also related to the NW orientation and excitation polarization.[165,166] Except for the emission intensity, the NW could also change the angular radiation patterns of the emitters.[167] From the back focal plane radiation patterns, the branching ratio of excitons decaying into propagating SPs on the NW to direct far-field emission was estimated.[168] The coupling between two-dimensional transition-metal dichalcogenide semiconductors and metal nanostructures has been studied recently. The exciton−plasmon−photon conversion processes of Figure 28a are demonstrated in a system composed of a single layer of molybdenum disulfide (MoS_2) and a Ag NW (Figure 28d).[163,169]

6.1.3. Exciton−Plasmon Coupling of Single Quantum Emitters and Metal Nanowires.
The measurements on the coupled systems of single QEs and NWs are highly desired for studying the effects of QE-NW separation and transition dipole orientation on the exciton−plasmon coupling. Moreover, the exciton−plasmon coupling at the single photon level is a very important step toward the application of quantum plasmonic devices in quantum information and quantum communication

technologies. Single QDs and single NV centers in nanodiamonds are the most popularly used QEs for studying the exciton−plasmon coupling at the single photon level. In addition to NWs, the interactions between QEs and different kinds of plasmonic waveguides, for example, metal wedge waveguides and V-groove waveguides, have also been explored.[170,171]

The first experimental demonstration of efficient exciton−plasmon coupling between single QEs and plasmonic NWs was reported by Akimov et al.[20] In their study, dispersive colloidal CdSe QDs on a glass substrate were separated from Ag NWs by a layer of poly(methyl methacrylate) (PMMA) with a thickness in the range of 30−100 nm. The single QDs randomly distributed at the near-field region of the NW were carefully selected and measured. The exciton−plasmon conversion was verified by the observation of fluorescence emission from the NW ends (Figure 29a). The high degree of correlation between the blinking curves of the fluorescence counts from the QD and the ends of the NW confirms that the QD is the source of the SPs propagating along the NW (Figure 29b). Photon coincidence measurement of the coupled QD demonstrates its single photon emission property. A clear antibunching in the cross-correlation measurement between the emissions from the QD and the end of the NW means that the single photon emission from the QD and the single plasmon generation on the NW cannot happen simultaneously (Figure 29c), indicating the generation of single quantized SPs on the NW.

Although SPs involve the collective oscillation of plenty of electrons on metal surfaces, they can be quantized and have the properties of bosons.[172,173] Experiments have confirmed that photonic entanglement could be encoded into the SPs.[174−176] Another fundamental quantum feature of a single quantum excitation is the wave−particle duality. Kolesov et al. demonstrated the wave−particle duality of single propagating SPs generated by an optically excited NV center in a diamond nanocrystal in the near-field region of a Ag NW (Figure 29d).[21] They showed the particle-like behavior by measuring the second-order correlation function of the emission at both ends of the NW (Figure 29e). Because of the reflection at the NW ends, one single SP reflected at one end of the NW will interfere with itself, which results in the Fabry-Pérot modulated fluorescence spectrum at the NW ends, clearly showing the wave-like behavior of a single SP on the Ag NW (Figure 29f).

The metal NW behaves as an optical nanoantenna to direct the radiation of the single QE in well-defined directions. Figure 29g (i) shows the fluorescence image of a coupled system of a QD and a Ag NW with a 10 nm Al_2O_3 layer as a spacer. The Fourier imaging of the fluorescence emission of this QD (Figure 29g, ii) shows two bright lobes along the NW axis direction with a small spreading angle, which is quite different from the emission of a reference QD on the glass substrate without coupling with the Ag NW. The Fourier imaging of the scattering of single plasmons at the NW end shows an arc-shaped pattern with the maximum intensity along the NW axis (Figure 29g, iii), demonstrating the unidirectional radiation of the single plasmons. The high directionality of both the direct emission of the QD and the out-coupling of the QD-generated SPs indicates that the QD-NW coupled system can be used as a directional single photon source with high light extraction efficiency. Figure 29h shows the decay curves of the fluorescence emission from a NW-coupled QD and an uncoupled QD. It is clear that the QD coupled with the Ag NW decays faster, indicating the spontaneous emission rate is
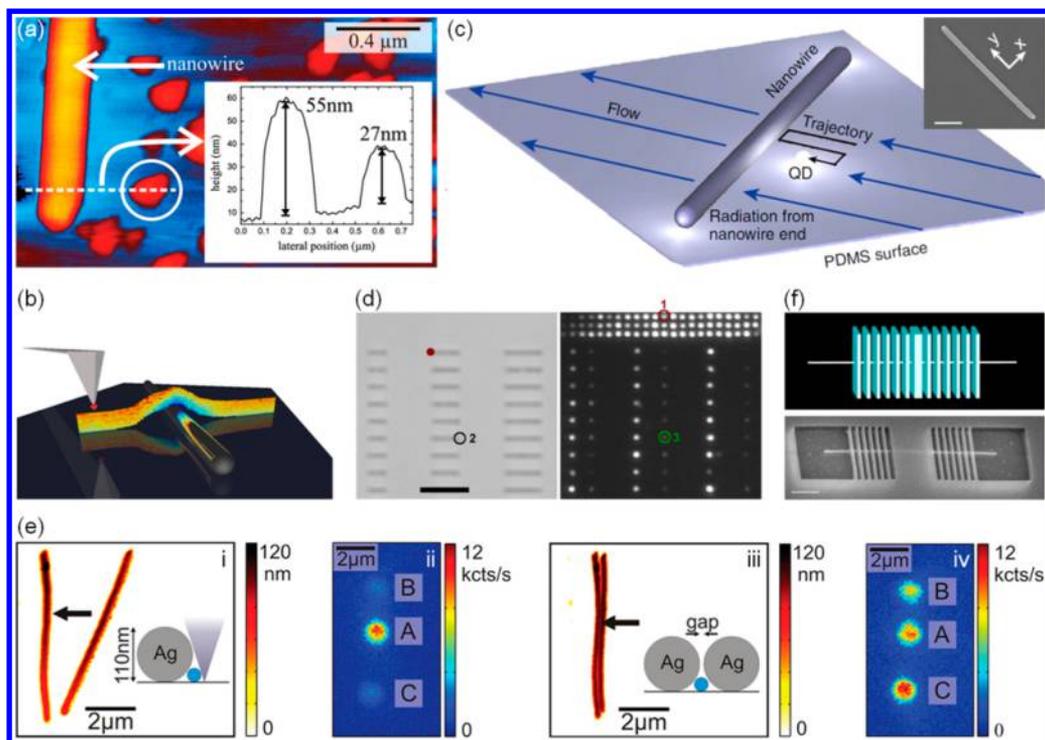
Figure 30. Different methods to control the interaction between single QEs and plasmonic NWs. (a) AFM topography of a Ag NW and a diamond nanocrystal containing the investigated NV center (white circle), which is well-separated from other diamonds and the Ag NW. The inset shows the height profile of the wire and the diamond, taken along the white dashed line. In the next step, the diamond nanocrystal will be pushed to very close proximity of the NW by operating the AFM in contact mode. Reprinted with permission from ref 178. Copyright 2011 American Physical Society. (b) Schematic of scanning a single QE using a scanning probe. The NV center in a diamond nanocrystal is attached to an AFM probe and positioned with respect to the NW of interest. Reprinted from ref 107. Copyright 2014 American Chemical Society. (c) Schematic of the positioning technique using microfluidic flow control. A single QD is driven along a trajectory close to the wire by flow control. The inset shows a SEM image of a typical Ag NW used in the experiments (scale bar, 1 μm). Reprinted with permission from ref 181. Copyright 2013 Nature Publishing Group. (d) (Left) White light transmission image of the CdSeTe/ZnS QD-Ag NW coupling structures fabricated by a two-step EBL procedure (scale bar, 5 μm). The red spot marks one QD area. (Right) The corresponding fluorescence image. The reference QDs are placed on the top area. Light due to SP scattering is seen on the right-side NW ends. Reprinted with permission from ref 183. Copyright 2012 American Institute of Physics. (e) (i, iii) AFM topography images of two Ag NWs (the black arrow indicates the location of the NV center in a nanodiamond) and sketched cross sections (i) for moving the nanodiamond close to a NW by an AFM tip and (iii) for the nanodiamond located in the nanogap between two NWs. (ii, iv) Fluorescence images of the dual wire structure when the NV center is excited. Reprinted from ref 180. Copyright 2013 American Chemical Society. (f) Schematic (top) and SEM image (bottom) of a plasmon resonator made on a Ag NW by defining distributed Bragg reflectors on the surrounding PMMA medium (scale bar, 1 μm). Reprinted with permission from ref 83. Copyright 2012 American Physical Society.

enhanced. As will be seen in section 6.3, both the enhancement of the spontaneous emission rate and the quantum efficiency of generating single SPs are strongly dependent on the separation distance between the QD and the NW.

6.2. Controlled Exciton−Plasmon Coupling between Single Quantum Emitters and Metal Nanowires

The separation distance between the QE and the plasmonic NW is a critical parameter influencing the decay of the exciton into the three different decay channels. Therefore, the most direct way to control the exciton−plasmon coupling is to manipulate the position of the QE relative to the NW surface. The methods for controlling the separation distance between the QE and the NW mainly include tuning the thickness of a spacer, nanopositioning, scanning QE, microfluidic flow control, two-step EBL, self-assembly, etc.

The most commonly used method to control the separation distance between QEs and plasmonic NWs is to separate them by a spacer layer of a certain thickness. A layer of polymer, such as PMMA or poly(vinyl alcohol) (PVA), is usually used as the spacer between the emitters and the NWs.[20,177] The spacer can also be prepared by depositing dielectric films, for example SiO$_2$

and Al$_2$O$_3$, where the thickness of the spacer can be more precisely controlled. After depositing the dielectric film onto the NW surface, the emitters (e.g., QDs) are deposited. The Al$_2$O$_3$ layer can be prepared using the atomic layer deposition technique, which produces smooth Al$_2$O$_3$ films with a precisely controlled thickness. The high quality of the Al$_2$O$_3$ film also facilitates the subsequent spin-coating of the QDs. The composite system of Ag NW-Al$_2$O$_3$-QD provides a very good platform to study the distance dependence of the exciton−plasmon coupling.[88] However, the spin-coated QDs on the sample surface are usually randomly distributed, making such an approach unsuitable for preparing samples that require the QD position to be well-controlled.

Nanopositioning techniques can assemble photonic structures with single emitters by pushing nano-objects on a substrate to selected locations. Using this method, Huck et al. controlled the tip of an AFM to push a single diamond nanocrystal to approach a nearby Ag NW (Figure 30a).[178] In the experiment, an individual diamond nanocrystal with a single NV center was first identified using optical characterization, and the sample topography was obtained by the AFM scanning in tapping mode. In the next step the manipulation of the

diamond nanocrystal was performed with an AFM tip in contact mode. They compared the photon emission properties of a NV center before and after coupling with a Ag NW, and a total decay rate enhancement by a factor of up to 4.6 was demonstrated. Similarly, single diamond nanocrystals can be placed inside the nanogaps between Ag NWs aligned end-to-end and parallel.[179,180]

The single QEs can be attached to the end of a scanning probe and move around the plasmonic NW surface, providing another method to control the QE-NW interaction. Frimmer et al. attached a fluorescent nanobead to a scanning tip and scanned the nanobead over Au and Ag NWs.[106] It was shown that the decay rate of the point-like source can be reversibly changed by a factor of 2 by coupling to the guided SPs on the NW. Schell et al. utilized the single NV center in a diamond nanocrystal attached on the tip of an AFM to perform three-dimensional fluorescence lifetime imaging measurements around a Ag NW surface (Figure 30b).[107] The mapped LDOS shows clear oscillations along the NW, which is caused by the interference of SPs reflected at the end of the NW and the ones directly launched into the NW.

The electroosmotic flow technique in a microfluidic device combined with a vision-based feedback control method was used by Ropp et al. for positioning and moving single QDs around a Ag NW (Figure 30c).[181,182] Specifically, the fluorescence image of an individual QD was continuously captured by a CCD camera. The tracking algorithm determined the position of the QD in real time by fitting the imaged diffraction spot to a Gaussian point spread function. The control algorithm then compared the current position of the QD to the desired location and calculated the required voltage to actuate the QD. By applying an appropriate voltage continuously, a single QD can be driven along a trajectory close to the NW surface. By analyzing the intensity and lifetime of the fluorescence at different positions, they mapped out the spontaneous emission modifications of the QD on the Ag NW with a spatial accuracy of about 12 nm.

Further efforts have also been made to exploit more advanced designs to realize the coupling between single QEs and metal NWs. Gruber et al. applied a two-step EBL process to fabricate the coupling structures of colloidal QDs and plasmonic NWs (Figure 30d). The first EBL step produced a PMMA mask for the NWs followed by vacuum deposition of Ag, while the second EBL step fabricated a PMMA mask with nanoholes for subsequent deposition of QDs. To prevent the quenching of the QD fluorescence, a 15 nm thick SiO_2 film was deposited on the Ag NW after the Ag deposition.[183] The order of these two steps can also be reversed (i.e., first fabricating the nanoholes for QD deposition and then fabricating Ag NWs).[184] In the experiment by Pfaff et al., they first determined the position of NV centers on a glass substrate with respect to alignment marks and afterward fabricated Ag and Al NWs by EBL.[185] Another promising approach for preparing hybrid nanostructures is self-assembly. Self-binding of single diamond nanocrystals onto the terminals of Ag NWs was demonstrated in the mixture composed of chemically synthesized Ag NWs, fluorescent diamond nanocrystals, ascorbic acid, and deionized water.[186] The advantage of the two-step EBL and self-assembly techniques is the possible fabrication of many coupled structures in parallel.

Although the controlled exciton−plasmon interaction between single QEs and plasmonic NWs has been realized experimentally, the enhancement of the decay rates, however, is modest as a result of the difficulty in accessing the strongly confined plasmon mode. It is highly desirable to design a plasmonic NW structure with much stronger field confinement to enhance the exciton−plasmon coupling strength. Liu et al. proposed that the coupling strength can be further increased by putting the dipole emitter into the nanogap between two gold NWs placed in parallel.[187] Compared with a single NW, the plasmonic gap mode shows a stronger field confinement[188] and can enhance the exciton decay rate into the plasmon mode significantly. The experiment reported by Kumar et al. demonstrated the coupling of a single NV center in a diamond nanocrystal to the propagating gap plasmon mode of two parallel placed chemically grown Ag NWs (Figure 30e).[180] The coupled structure was prepared by manipulating the diamond nanocrystal and Ag NW with an AFM tip. The measured enhancement factor of the spontaneous emission rate is 8.3, which is 2.2 times of that for the single NW case. The nanogaps between a metal NW and a metal nanorod or a metal substrate can also strongly enhance the coupling between an emitter and a metal NW.[189,190] Russell et al. reported the spontaneous emission rate enhancement of the order $\sim 10^3$ for fluorescent organic dyes coated on the dielectric spacer between a Ag NW and a Ag substrate.[190]

Besides producing nanogaps in plasmonic NW structures to decrease the mode volume, another strategy to strengthen the exciton−plasmon coupling is to enhance the quality factor of the plasmon mode by introducing resonators. A plasmon resonator composed of a Ag NW surrounded by patterned dielectric distributed Bragg reflectors was reported (Figure 30f).[83] The defect-free, highly crystalline Ag NW was embedded in PMMA, and a cavity resonance was achieved by fabricating distributed Bragg reflectors in the PMMA along the NW using EBL. The experimentally obtained highest quality factor is close to the theoretically calculated maximum value of ~ 100 (at the vacuum wavelength 650 nm for a Ag NW with a diameter 100 nm). An enhancement of the spontaneous emission rate by a factor of 75 was achieved at the cavity resonance.

6.3. Quantum Yield of Single Surface Plasmons

Except for the enhancement of the total decay rate, another important parameter quantifying the exciton−plasmon coupling between QEs and metal nanostructures is the SP quantum yield, which is the quantum efficiency of excitons in the QEs converting to SPs. The SP quantum yield strongly influences the performance of plasmon-assisted phenomena and applications, such as plasmon-enhanced fluorescence,[149,150] plasmon-mediated energy transfer,[191,192] plasmon-enhanced light-emitting diodes,[193] exciton−plasmon−photon conversion,[160,162] plasmonic amplifiers and nanolasers,[22,194−196] and so on. The SP quantum yield can be determined experimentally through distinguishing the three possible exciton recombination channels (i.e., direct free-space radiation, SP generation, and nonradiative damping) and obtaining their corresponding exciton decay rates. Since the directly emitted photons from the QEs and the scattering of exciton-generated SPs on the metal nanostructure are usually indistinguishable, it is difficult to separate the SP generation from the direct free-space radiation. This hinders the determination of the SP quantum yield.

In the coupling system composed of a single QE and a plasmonic NW, the exciton-generated propagating SPs are partially scattered as photons at the NW ends, and therefore

spatially separated from the directly emitted photons at the position of the QE. The intensities of photons at these different positions are related to the ratio of the decay rates of free-space radiation channel and SP generation channel. With the intensity information at the NW ends, the plasmon induced energy loss can be extracted by determining the propagation length of the SPs on the NW. Therefore, the coupled QE-NW system provides an ideal platform to differentiate the decay rates of the three channels to obtain the SP quantum yield.

In a coupled system composed of a single CdSe/ZnS QD and a Ag NW, the quantum yield of single SPs was experimentally obtained by determining the decay rates of all the exciton recombination channels.[88] By exciting the QD coupled to the NW using laser light polarized parallel to the NW axis, the excitation rate of the coupled QD stays the same as the uncoupled QDs on the substrate. Therefore, the fluorescence intensity difference between the coupled and uncoupled QDs is merely caused by the fluorescence quantum yield (i.e., the ratio of the radiative decay rate and total decay rate). By measuring the fluorescence quantum yield of the uncoupled QDs using a calibrated integrating sphere method, the quantum yield of the direct free-space radiation of the coupled QD is obtained. Then the decay rate of the direct free-space radiation channel Γ_{rad} can be extracted, considering the total decay rate Γ_{total} of the coupled QD can be calculated from the measured fluorescence lifetime τ ($\Gamma_{total} = 1/\tau$). The decay rate ratio of the SP generation channel and the free-space radiation channel Γ_{SP}/Γ_{rad} was obtained by using the spatially separated fluorescence intensities at the positions of the NW ends and the QD, which correspond to the scattering of the QD-excited SPs at the NW ends and the direct free-space emission from the QD, respectively. In the analysis of Γ_{SP}/Γ_{rad}, the SP propagation loss and reflections at the NW ends were considered to extract the original intensity of the QD-excited SPs. The decay rate of the nonradiative damping channel Γ_{nrad} was then calculated by subtracting the radiative decay rate Γ_{rad} and the SP generation rate Γ_{SP} from the total decay rate Γ_{total}. The SP quantum yield was finally obtained as the ratio of the SP generation rate to the total decay rate [i.e., $\eta = \Gamma_{SP}/(\Gamma_{SP} + \Gamma_{rad} + \Gamma_{nrad})$].

Using the above procedure, the distance-dependent exciton recombination dynamics in the QD-NW system was studied using a thin Al_2O_3 film as a spacer layer. Figure 31a shows the distance dependence of the decay rate ratio of the SP generation channel and the free-space radiation channel. The ratio shows an exponential decrease as the Al_2O_3 film thickness increases from 3 to 35 nm, which means that the interaction between the exciton and the plasmon is stronger for smaller separations. The measured fluorescence lifetime indicates that the total decay rate is larger for smaller QD-NW separations (Figure 31b). Figure 31c shows the decay rates of all three recombination channels. Clearly, the decay rates of all three channels increase as the spacer thickness decreases, but the increasing rates are obviously different. Compared with the moderate increase of the direct free-space radiation channel, the SP generation channel has a higher rate of increase. The decay rate of the nonradiative damping channel remains almost constant for spacer thicknesses larger than 15 nm. Therefore, the SP quantum yield keeps increasing as the spacer thickness decreases from 35 to 15 nm (Figure 31d). When the thickness is smaller than 10 nm, the decay rate of the nonradiative damping channel increases faster and becomes much larger than the decay rates of the other two channels. This results in
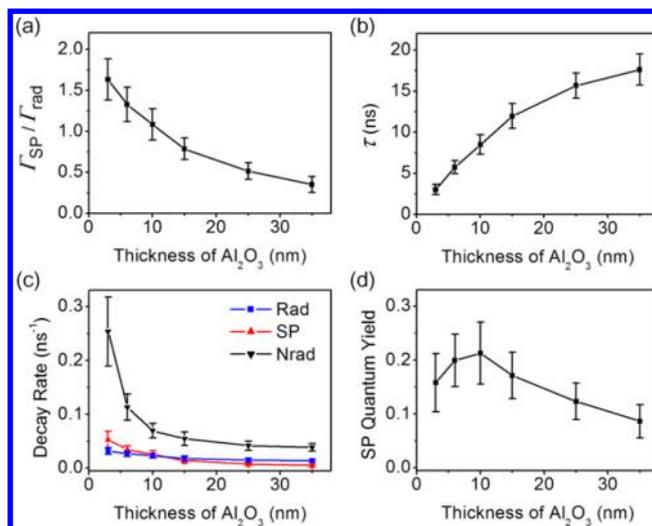

Figure 31. Distance-dependent optical properties of the QD-NW coupling system. (a) The measured decay rate ratio of the SP generation channel and free-space radiation channel, (b) fluorescence lifetime, (c) exciton decay rates of the three channels, and (d) the extracted SP quantum yield as a function of Al_2O_3 thickness. The legends "Rad", "SP", and "Nrad" in (c) correspond to the free-space radiation channel, SP generation channel, and nonradiative damping channel, respectively. The error bars represent the standard error of the measured data. Reprinted from ref 88. Copyright 2015 American Chemical Society.

the existence of an optimum QD-NW distance of about 10 nm for a maximum SP quantum yield of 21%.

The SP quantum yield is an important parameter to quantify the exciton−plasmon coupling process. The obtained distance dependence of the SP quantum yield in the QD-NW structure can be extended to the coupling systems composed of QEs and other metal nanostructures, where the enhancement factor of total decay rate (spontaneous emission rate) is usually used to quantify the exciton−plasmon coupling strength. A stronger exciton−plasmon coupling strength is usually desired in plasmon-assisted applications, corresponding to a higher total decay rate at a smaller separation between the QEs and the nanostructures. However, the dramatically increased non-radiative decay rate at smaller separation distances will decrease the SP quantum yield, which needs to be avoided in applications. Therefore, the three decay channels need to be balanced to optimize the performance of plasmonic devices.

6.4. Surface Plasmons on Nanowires Interacting with Multiple Quantum Emitters

Since photons are ideal carriers of quantum information, controlling the transport of single photons in a nonlinear system is of central importance in the realization of quantum information and quantum communication networks. One possible strategy to accomplish this goal is by using the strong coupling between excitons in single QEs and propagating SPs supported by a plasmonic NW. For a single two-level QE strongly coupled with a plasmonic NW, the incoming single SP on resonance with the energy gap of the QE can be reflected by the QE with reflectance $R \sim (1 - 1/P)^2$ near unit, where $P = \Gamma_{SP}/(\Gamma_{rad} + \Gamma_{nrad})$.[197] For a three-level QE strongly coupled with the NW, a single "gate" photon can control the propagation of subsequent "signal" pulses consisting of either individual or multiple photons, leading to the realization of a single-photon transistor.[197] If two two-level QEs are coupled to
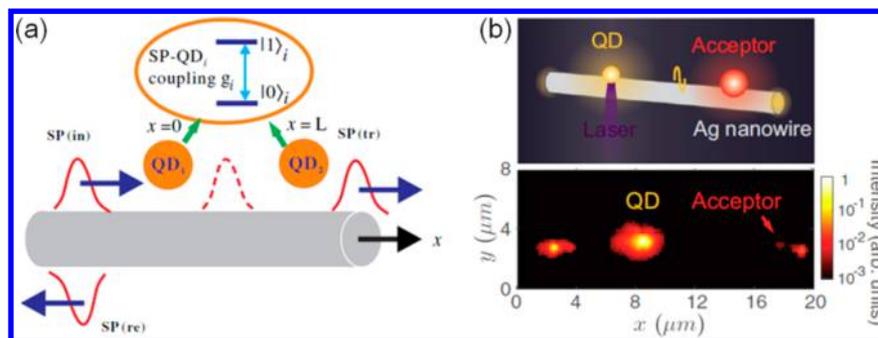
Figure 32. (a) Schematic of the system consisting of two QDs side-coupled to a plasmonic NW. The SPs are evanescently coupled to the QDs with coupling strength g_i (i = 1, 2). The QD_i is modeled as a two-level system with a vacuum state $|0\rangle_i$ and an exciton state $|1\rangle_i$. Reprinted with permission from ref 201. Copyright 2012 Optical Society of America. (b) (Top) Schematic of the energy transfer between a single QD donor and a fluorescent nanoparticle acceptor mediated by the SPs on a Ag NW. (Bottom) Fluorescence image of the energy transfer system when the laser is focused on the QD. Bright spots are detected at the positions of both emitters as well as both ends of the NW. Reprinted with permission from ref 202. Copyright 2017 American Physical Society.

the NW, the two QEs can act as two tunable mirrors (Figure 32a). A Fabry-Pérot cavity will be formed between the two QEs. The transmission of a single SP on the NW could be switched on or off by adjusting the spectral detuning and controlling the spatial separation of the two QEs.[198−200] For a large difference of the transition energies, the transmission spectrum is a simple combination of the two transmission spectra of the QEs. As the difference of the transition energies becomes smaller, a Fano-like line shape of the transmission spectrum is obtained.[201]

The propagating SPs between two QEs coupled with the plasmonic NW can be either reflected or transmitted and finally detected at the end of the NW. In principle, it is also possible that the SPs are not transmitted or reflected but trapped between the two QEs, which means that entanglement can be created between the two QEs.[203−207] González-Tudela et al. theoretically demonstrated that a plasmonic waveguide can be used to obtain a large degree of qubit−qubit entanglement between two QEs separated by distances larger than the operating wavelength.[208] They explored both the spontaneous formation of entanglement from an unentangled state and the steady-state entanglement under continuous pumping. The degree of entanglement can be modulated by changing the separation of the two QEs. Inspired by the potential applications of the coupled system of two QEs and a plasmonic NW in the field of quantum information and quantum communication, Li et al. reported the first experimental study of two QDs coupling to a Ag NW.[209] The coupled system of multiple QEs with a plasmonic waveguide provides a platform to study quantum optics phenomena at nanoscale and to construct quantum devices with different functions, deserving more experimental studies.

Since the demonstration of the long-distance plasmon-mediated resonance energy transfer using Ag films,[191] a great deal of effort has been devoted to investigating plasmon-mediated energy transfer using nanoparticles[210−212] and plasmonic waveguides.[192,213,214] The energy transfer between two fluorescent molecules mediated by plasmonic waveguides of different cross-sectional shapes has been theoretically studied by means of the finite element method. It was found that the normalized energy transfer rate strongly depends on the donor−acceptor separation distance and their positions relative to the waveguide surface. The wedge and channel waveguides present a normalized energy transfer rate 20 times larger than

that of the circular cylinder NWs.[213] Experimentally, the energy transfer between two fluorescent nanoparticles mediated by SPs on a Ag NW was investigated using a dual-beam scanning confocal imaging method, where the excitation and detection beams were scanned independently. Long-range plasmon-mediated energy transfer was demonstrated by the observation of fluorescence from the acceptor induced by the excited donor. The reported energy transfer efficiency was up to 17% for a donor−acceptor separation of 1.3 μm.[215] Very recently, the energy transfer between a single QD donor and a fluorescent nanobead acceptor was reported (Figure 32b). The measured decay histogram of the acceptor was the convolution of the decay histograms of the donor and the acceptor excited independently. The strong correlation between the fluorescence intensity of the QD and the acceptor also confirmed the occurrence of energy transfer.[202]

6.5. Remote Excitation/Detection of Quantum Emitters Coupled to Metal Nanowires

In conventional photoluminescence measurements, the fluorophore is directly excited by the incident laser light and the fluorescence is detected from the same spot. Such an excitation and detection approach can be easily accomplished and is widely used. However, it may not be feasible in some applications, especially in living systems, where the higher-power incident light may cause cell destruction or induce chemical modifications of the analytes. The exciton−plasmon−photon interconversion processes shown in Figure 28a provide another kind of fluorescence measurement prototype, remote excitation and remote detection, where the excitation beam and detection spot are away from the measured fluorophore. This technique was demonstrated in the coupled system of a single QD and a Ag NW (Figure 33, panels a and b).[216] The propagating SPs generated by focusing laser light on the end of a Ag NW can excite the single QD in the near-field region of the NW but microns away from the excitation spot. The excited QD converts part of its energy into propagating SPs by exciton−plasmon interaction, which are scattered into photons at remote sites and detected therein. The remote-excitation and remote-detection of multiple QDs were also realized. Furthermore, due to the tight confinement of propagating SPs on the NW surface, the selective excitation of QDs very close in space but at different separations from the NW is possible. This can strongly reduce the fluorescence background as compared with the large excitation spot under
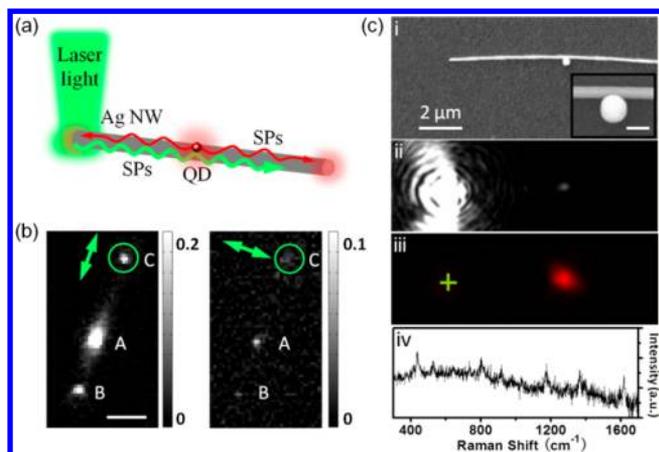
Figure 33. (a) Sketch of the remote excitation and detection of a single QD coupled to a Ag NW. (b) Fluorescence images of a QD-NW coupled system with laser polarization parallel (left) and perpendicular (right) to the NW. The green circles show the laser excitation positions. The largest bright spot A corresponds to the fluorescence from the QD, while two smaller spots B and C correspond to SPs scattered at the two ends of the NW. (c) (i) SEM image of a Ag NW-nanoparticle structure for remote SERS. (ii) Scattering image of the Ag NW-nanoparticle structure under focused laser light illumination at the end of the NW. (iii) Raman image after background subtraction. The green cross marks the position of the NW end. (iv) Remote SERS spectrum. (a and b) Reprinted with permission from ref 216. Copyright 2014 Chinese Physical Society and IOP Publishing Ltd. (c) Reprinted from ref 218. Copyright 2009 American Chemical Society.

conventional excitation conditions. The remote excitation of single fluorescent molecules labeled on Ag NWs showed that the single-molecule fluorescence point spread function depends on the NW dimensions and the position and orientation of the molecular transition dipole.[217]

Compared with the fluorescence of a single molecule, the Raman scattering is very weak because of the small scattering cross section. Usually, the SERS signal can be detected in the hot spots of plasmonic nanostructures, such as the nanogap of a nanoparticle dimer. Because of the modest near-field enhancement around the plasmonic NW, it is difficult to directly generate a SERS signal by using propagating SPs on the NW. One solution is to introduce some junctions between plasmonic NWs and some nanoparticles to form hot spots, where the electromagnetic field is strongly enhanced.[219] For the molecules located in the junctions, their Raman scattering is enhanced enough to become detectable. A Ag NW-nanoparticle system was first adopted to achieve the remote SERS.[218,220] The propagating SPs on the NW excited by laser light focused on the end of the NW induce a strong localized electromagnetic field in the nanogap between the NW and the nanoparticle, and the Raman scattering of the molecules in the nanogap is excited remotely (Figure 33c). The large field enhancement in the nanogap enables single molecule sensitivity of this remote excitation SERS technique.[218] Remote SERS has also been achieved in different kinds of plasmonic NW systems, such as crossed Ag NWs[218,221] and Ag NW bundles.[222] By using the remote excitation, the SERS signal inside a living cell was detected without inducing any noticeable damage.[223] A Ag NW with a Ag nanoparticle attached was fixed upon a pre-etched tungsten tip. The NW was then inserted into a living cell, and finally a remote-SERS signal from the NW apex was measured by focusing laser light onto the position of the nanoparticle.

7. HYBRID NANOWIRE WAVEGUIDES AND PLASMONIC GAIN

7.1. Hybrid Nanowire Waveguides

The losses limit the propagation length of the SPs on metal NW waveguides, as discussed in section 5.5. In order to maintain the deep subwavelength confinement offered by the metal NWs, and simultaneously decrease the propagation loss of the SP modes, a hybrid plasmonic mode was proposed theoretically, which exists at the interfaces of a semiconductor−insulator−metal waveguide.[15] This hybrid plasmonic mode was later demonstrated experimentally, showing a mode area as small as $\lambda^2/400$.[224]

To understand this hybrid plasmonic mode, we can look at a four-layered planar structure of dielectric−semiconductor−
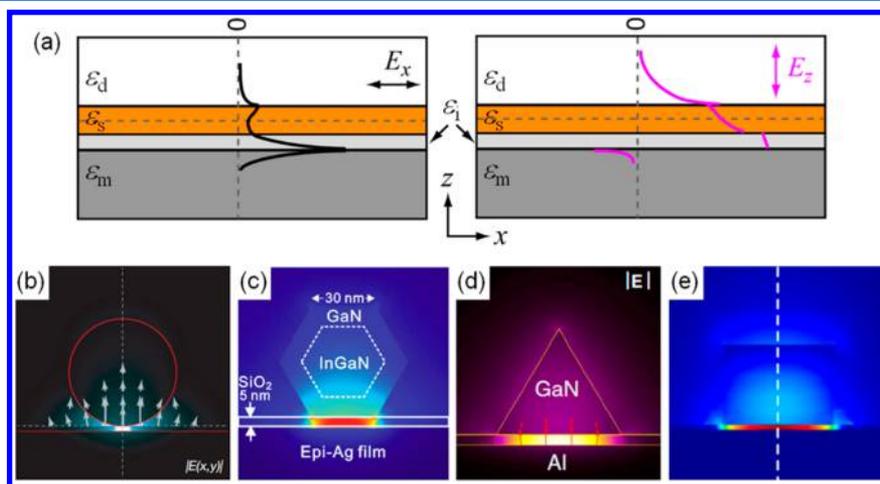
Figure 34. (a) Schematics describing the electric field distributions of a plasmonic-like hybrid TM mode within the four-layered planar structure for the E_x (left panel) and E_z (right panel) components, respectively. (b−e) Cross-sectional views of the TM mode distributions in semiconductor NW−insulator−metal structures. (b) Reprinted with permission from ref 224. Copyright 2009 Nature Publishing Group. (c) Reprinted with permission from ref 195. Copyright 2012 American Association for the Advancement of Science. (d) Reprinted with permission from ref 226. Copyright 2014 Nature Publishing Group. (e) Reprinted from ref 196. Copyright 2016 American Chemical Society.
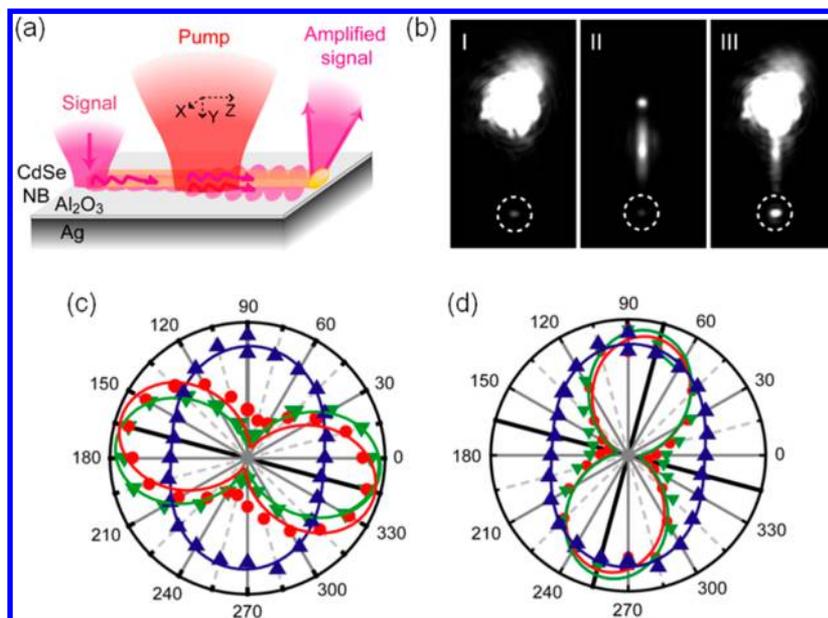
Figure 35. (a) Diagram of a CdSe NB/Al$_2$O$_3$/Ag hybrid plasmonic waveguide and the excitation and amplification of the input probe signal when operated in a pump−probe setup. (b) Optical images, obtained with a 730 ± 5 nm band-pass filter, corresponding to a probe signal launched from the top end of the hybrid plasmonic waveguide (NB 177 nm × 140 nm × 8.6 μm) and emitted from the bottom end, highlighted by the dashed circle (I), photoluminescence with the pump only (II), and the amplification of the probe signal when both pump and probe are present (III). The two ends of the waveguide are clearly visible as the top and bottom bright spots in (II). (c and d) Plots of the emission polarization with the input laser beam polarized along and perpendicular to the CdSe NB, respectively, and the pump beam polarized along the NB. Red, blue, and green symbols describe the polarization of the emitted probe signal, scattered photons from the SPs excited by the pump, and total amplified signal, respectively. The curves are normalized to the maximum intensity. Red and green curves are fits to linearly polarized lights. Blue curve is the fit to a linear combination of two noncoherent light beams with orthogonal linear polarizations. Reprinted with permission from ref 22. Copyright 2013 Nature Publishing Group.

insulator−metal, as shown in Figure 34a. For simplicity, we assume that the light propagates in the x direction only and there is no spatial variation in the y direction. The z axis is perpendicular to the interfaces of the different media. The TM mode existing in this structure can be considered as the hybridization of the guided photonic TM mode in the top three layers with the plasmonic TM mode at the interface of the bottom two layers. This TM mode is called a hybrid plasmonic mode as its dispersion curve closely resembles that of the SPs propagating at a single dielectric−metal interface. This mode has electric field components in both the x and z directions, with the field distributions shown in Figure 34a. The hybridization leads to the electric field of the mode peaking in the region of the ultrathin insulator and effectively decreases the electric field within the metal. As a result, the propagation loss of this hybrid TM mode is significantly smaller than that of a TM mode at the single metal−insulator interface. In particular, the application of epitaxially grown plasmonic metal films such as Ag, Au, and Al further reduces the propagation loss of the hybrid plasmonic mode.[195,225]

The hybridization of the photonic and the plasmonic modes can be described by the coupled mode theory.[15,227,228] In three dimensions, the semiconductor layer usually adopts a form of NW, with spatial confinement in width and in height within the range of a few tens to a few hundreds of nanometers, as shown in Figure 34 (panels b−e). The "character" of the hybrid mode, describing the degree to which the guided mode is more plasmonic-like (or photonic-like), depends on the separation distance between the semiconductor NW and the metal film.[15] Using these hybrid plasmonic waveguides, researchers can achieve extreme mode confinement as well as longer propagation distances (from a few tens to a few hundreds of micrometers) from the visible to THz spectral range.[229−231] The low propagation loss of hybrid plasmonic waveguides can go beyond the "good" plasmonic metals (Ag and Au) and be achieved with industry relevant metals such as Cu.[230] The strong electric field confinement in the hybrid plasmonic waveguides has been utilized for molecular fluorescence enhancement,[232] second harmonic generation,[233] and strengthening the optical force within the insulator gap.[234] There are also interesting applications using these hybrid plasmonic waveguides for on-chip broadband couplers,[235] polarization dependent beam splitters,[236,237] all-optical logic gates,[238] and optical waveplates.[239] More applications can be found in other comprehensive reviews.[2,240]

7.2. Loss Compensation

Despite the substantially decreased propagation loss offered by hybrid plasmonic waveguides, a successful signal transport within a plasmonic waveguide based circuit still requires a loss compensation mechanism so that the information carried by a plasmonic signal can be transferred from one part of the circuit to another without being misinterpreted. This requirement is crucial to the scalability and cascadability of plasmonic circuits. The loss compensation in various plasmonic structures was discussed in detail in refs 194, 241, and 242. Here we focus our attention to the loss compensation in a hybrid plasmonic waveguide.

We can estimate the upper limit of the optical gain required for the full compensation of the propagation loss of a hybrid plasmonic waveguide using the theory developed by Avrutsky for the SP propagation at a single metal−dielectric interface. It was predicted that the effective refractive index of the SPs can
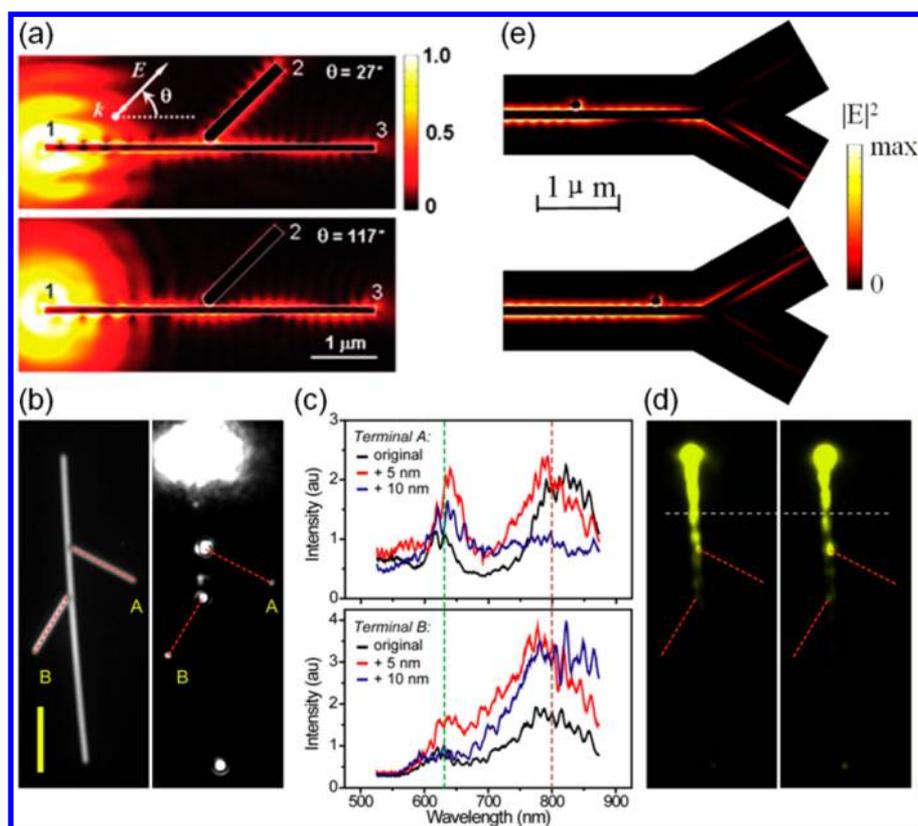
Figure 36. (a) Simulated electric field distributions in a branched Ag NW structure for different polarization directions of the incident light. (b) A structure composed of three Ag NWs was illuminated by supercontinuum light with incident polarization parallel to the main NW. The scale bar is 5 μm. (c) Emission spectra at terminal A from the right branch (top) and terminal B from the left branch (bottom) for the original structure (black) and for 5 nm (red) and 10 nm (blue) Al_2O_3 layer deposited, respectively. (d) QD fluorescence images for the original structure (left) and after 5 nm of Al_2O_3 was deposited (right). The wavelength of the laser is 633 nm. The red dashed lines in (b and d) show the positions of two branch wires. The white dashed line in (d) is a visual guide to show the shift of the near-field nodes and antinodes due to the addition of 5 nm-thick Al_2O_3. (e) Simulated electric field distributions of a plasmonic switch constructed by a branched Ag NW with a nearby Ag nanoparticle. (a) Reprinted from ref 16. Copyright 2010 American Chemical Society. (b−d) Reprinted with permission from ref 113. Copyright 2013 National Academy of Sciences of the USA. (e) Reprinted with permission from ref 40. Copyright 2014 Nature Publishing Group.

go to infinity at resonance conditions. This is only limited by the gain saturation and results in strong localization of the surface wave at the interface.[243] This effect can be simply demonstrated with the dispersion relation of SPs existing at the metal−dielectric interface $n_{eff} = \sqrt{\frac{\varepsilon_m \varepsilon_d}{\varepsilon_m + \varepsilon_d}}$, where ε_m and ε_d are the relative permittivities of the metal and dielectric, respectively. If the dielectric is carefully chosen so that the resonance condition is fulfilled ($|Re(\varepsilon_d)| = |Re(\varepsilon_m)|$) and the optical gain in the dielectric can compensate the loss of the metal ($|Im(\varepsilon_d)| = |Im(\varepsilon_m)|$), n_{eff} becomes infinitely large, making the SP mode extremely localized at the interface. For materials not satisfying the resonance condition, a lossless propagation requires $|Im(\varepsilon_d)| \cong (Re(\varepsilon_d))^2/(|Im(\varepsilon_m)|+(Re(\varepsilon_m))^2/|Im(\varepsilon_m)|)$. We can estimate the gain coefficient g of the gain material by using $g = k_0|Im(\varepsilon_d)|/\sqrt{Re(\varepsilon_d)}$, where k_0 is the wave vector of light in vacuum. For semiconductor materials with $Re(\varepsilon_d) = 11.6$, g is expected to be ∼7 × 10³ cm⁻¹ in order to achieve a lossless propagation at the semiconductor−Ag interface with a wavelength of 600 nm.

In the case of hybrid plasmon propagation, this gain coefficient can be significantly decreased. Still, the critical gain coefficient (lasing threshold) is estimated to be in the range of 1000 cm⁻¹, a number at the upper limit of what dye molecules or conjugated polymer materials can offer and more achievable

with semiconductor materials. Therefore, researchers have utilized optically active semiconductors as the high refractive index waveguide materials to compensate for the ohmic loss caused by the metal substrate. The realization of selected signal amplification by the resonant cavity through feedback mechanism (the hybrid plasmonic laser) was first achieved in 2009 by Oulton et al. by using the Fabry-Pérot cavity modes in a hybrid plasmonic NW where the two end facets of the semiconductor NW served as the partially reflective mirrors.[224] This nanometer-scale plasmonic laser is composed of a single crystal CdS NW on a silver film, separated by a gap layer of MgF_2. Using this configuration, the authors achieved lasing from a hybrid plasmonic NW at 489 nm at low temperature (<10 K). Since the publication of this work, hybrid plasmonic waveguides with modes concentrated at the semiconductor−insulator−metal interfaces have become a popular configuration to achieve plasmonic lasers with deep subwavelength mode areas, for different wavelengths, low lasing thresholds, and higher operating temperatures.[195,196,226,244−247]

The demonstration of signal amplification in a nonresonant configuration is critical for the further development of integrated hybrid plasmon based circuits. In situ amplification of weak signals without feedback can be achieved by a pump−probe configuration. The signal that needs to be amplified and the population inversion condition of the gain medium are

overlapped in both time and spatial domains.[248] The first experimental demonstration of a hybrid plasmonic waveguide amplifier was reported by Liu et al. on a hybrid plasmonic waveguide, consisting of a CdSe nanobelt (NB) separated from a Ag surface by a thin Al_2O_3 layer, using the pump–probe technique (Figure 35).[22] It was demonstrated that a weak hybrid plasmonic signal can be amplified by the hybrid plasmonic waveguide with an ultrahigh optical gain coefficient exceeding 6755 cm^{-1}. Figure 35b shows the amplification of the probe signal through stimulated emission when the pump light is on. It is quite clear that the probe signal is significantly amplified. More importantly, it was shown that the loss compensation works in a relatively broad spectral band and for input signals of tunable polarizations. Similar to the 1D metal NW case discussed in section 3, the fundamental TM_0 mode and the higher-order mode were selectively excited in the hybrid plasmonic waveguide by different polarizations of the input laser beam that was focused by an objective onto one end of the CdSe NB. The polarizations were conserved through the signal amplification process (Figure 35, panels c and d), and similar amplification coefficients were achieved for two orthogonal polarizations.

Interestingly, the experiments also showed a 35-fold decrease [compared to the photonic case (i.e., a CdSe NB on a glass substrate)] in the transparency threshold, at which the population inversion starts. This means that the gain material in the hybrid plasmonic configuration reaches population inversion at a very low pump intensity. This is attributed to the "hot" carrier transfer at the metal–insulator–semiconductor interfaces upon the illumination of pump light. Population inversion facilitated by "hot" carrier transfer in combination with the enhanced stimulated emission cross section[196] due to the strong field confinement in the hybrid plasmonic modes indicates the possibility of high gain, low threshold plasmonic amplifiers, and promises a significant increase of the signal propagation length extending to hundreds of micrometers.

8. NANOWIRE PHOTONIC DEVICES

8.1. Router, Wavelength Splitter, and Switch

The various propagation behaviors of plasmons on metal NWs, including zigzag and chiral field distributions, and mode conversion, due to multimode superposition as discussed in section 5 can be utilized to realize photonic devices of different functions. By changing the polarizations of excitation light, the mode components and the field distributions on the NW can be manipulated as shown in Figure 13c, which provides a method to control the routing of plasmons in NW networks. A branched NW structure shown in Figure 36a is the simplest example of a NW network, where the plasmons generated at port 1 can propagate to both NW branches and finally radiate at port 2 and port 3. As discussed in Figure 13c, the polarization of the incident light can control the field distributions on the NW. In Figure 36a, by changing the polarization from 27° to 117°, the zigzag distribution is shifted, which alters the field intensity at the node of the branched NW structure, and directly determines the flow direction of the plasmon energy. In experiments, this routing function has been proved by optical scattering measurements[16] and QD fluorescence imaging.[41]

Since the routing function depends on the near-field distribution, changing the wavelength of the incident light can also change the period of the field pattern and influence the power routing between the two output branches. Under illumination of two wavelengths with the same polarization, the light components of different colors were separated to different ports, realizing the function of a wavelength splitter or demultiplexer.[16] The wavelength splitting was clearly demonstrated by exciting the SPs in a NW network using a white light source. Figure 36b shows a structure composed of three Ag NWs excited by supercontinuum light. The emissions at the NW ends A and B show clear wavelength dependence. For example, for the structure with an added Al_2O_3 film of 10 nm thickness (blue curves in Figure 36c), the NW end A mainly emits light of short wavelengths around 630 nm, while the end B mainly emits light of long wavelengths around 800 nm. The wavelength splitting behavior can be tuned by changing the thickness of the Al_2O_3 because the Al_2O_3 thickness influences the period of the electric field distribution, as shown in Figure 36d by the QD fluorescence images excited by laser light of 633 nm. For the original structure, the right branch junction is at a node of the plasmon field pattern, where the near-field intensity is low (left panel of Figure 36d). By adding 5 nm of Al_2O_3, the near-field antinode is shifted to the right junction, so more power is diverted to end A (right panel of Figure 36d), agreeing with the increased emission intensity of the 633 nm wavelength at end A in the spectra in Figure 36c. The routing behavior of plasmons of different wavelengths can be controlled separately by tuning the incident polarizations without interfering with other wavelengths. Therefore, the NW structure can be used for routing plasmons of multiple wavelengths simultaneously. Spectral splitting in Ag NW structures was also reported by designing gratings on the NWs to modulate the plasmon propagation.[81]

The electric field distribution on which the routing function depends can also be locally modulated on the NW, such as by exploring the mode conversion process discussed in section 5.4. An example of controlling the plasmon routing by mode conversion is shown in Figure 36e, which is formed by a branched NW with a nearby nanoparticle. The control of the routing is demonstrated by the simulation, where the TM_0 mode is used as input and a zigzag field distribution is produced by the mode conversion process induced by the nanoparticle. By tuning the position of the nanoparticle, the zigzag field distribution also shifts along the NW, which changes the distribution of the electric field at the junctions and switches the power between the two output branches. In the scheme of using a nanofiber to excite the plasmons on the NW, the electric field at the junction of the NW branch depends on the position of the nanofiber tip on the NW,[249] which can also be used to control the plasmon routing. Apart from the dynamic tuning of the structure and the excitation position, the active control of the power flow routes in the NW network can also be realized by tuning the refractive index of the environment or the dielectric coatings on the NWs.

8.2. Spin Sorter

As discussed in section 5.3, the circularly polarized light can be used to generate spin-dependent plasmons with zigzag distributions on the NW, by exploring the SOI of light. Similar to the routing of light with different linear polarizations shown in section 8.1, in the branched NW structure, the spin-dependent propagation of plasmons can be further sorted to separated branches, which offers an ideal platform for binary information encoding.

The enhanced optical SOI in the metal structure, as discussed in section 5.3, can result in transverse orbital
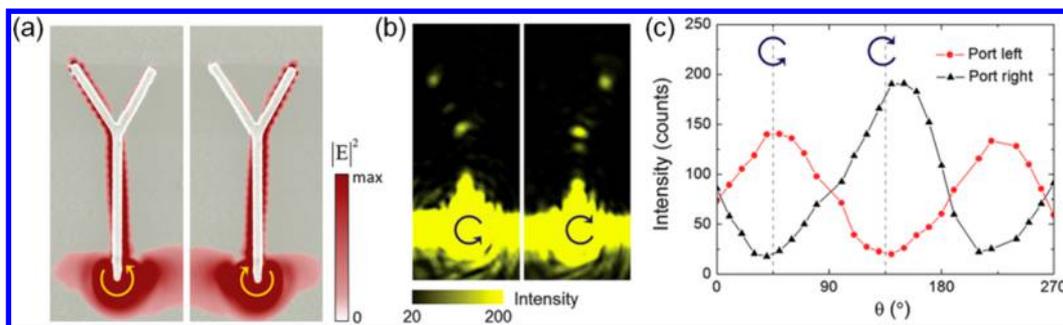
Figure 37. Spin-dependent directional propagation of SPs in a Au branched NW. (a) Simulated electric field distributions for excitation of 785 nm wavelength with different circular polarizations indicated by the circular arrows overlaid on the SEM image of the fabricated Au branched-NW structure. The Au NW is about 260 nm wide and 150 nm thick. The length of the main wire is about 3.7 μm. A uniform dielectric environment ($n = 1.5$) is used for the simulation. (b) Experimental scattering images for excitation by focused laser beams of 785 nm wavelength with opposite circular polarizations indicated by the circular arrows. (c) Measured intensities from the two output ports of the branched-NW structure for varying the angle θ between the optical axis of the quarter-wave plate and the linear polarization of the laser beam. $\theta = 0°$, $90°$, $180°$, and $270°$ in (c) correspond to linear polarization parallel to the main NW of the Y-branch structure, while $\theta = 45°$ and $135°$ correspond to circularly polarized light with opposite spins as indicated by the circular arrows. Reprinted with permission from ref 120. Copyright 2016 American Physical Society.
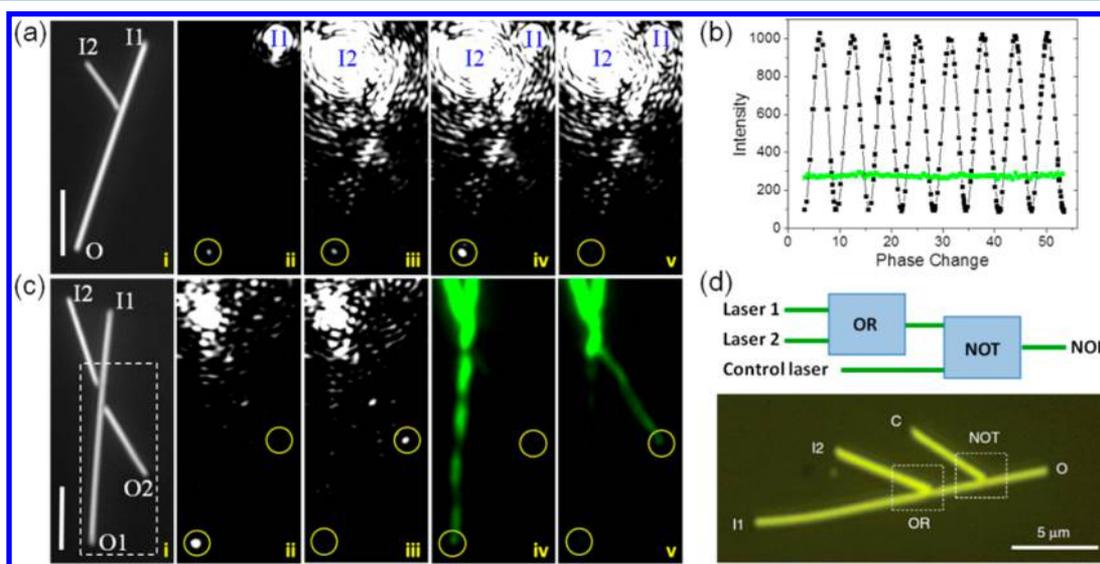
Figure 38. (a) (i) Optical image of a Ag NW structure with two input terminals (I1 and I2) and one output terminal (O). (ii, iii) Scattering images for the case of one input I1 or I2. (iv, v) Scattering images for the case of two inputs I1 and I2 with a varied phase difference. The scale bar is 5 μm. (b) Scattering intensity at output O as a function of optical phase delay for both I1 and I2 inputs (black) or for either I1 or I2 input (green). (c) (i) Optical image of a Ag NW structure with two input terminals (I1 and I2) and two output terminals (O1 and O2). (ii, iii) Scattering images for two phase differences corresponding to the strongest output at terminal O1 and O2, respectively. (iv, v) QD fluorescence images corresponding to ii and iii, respectively. (d) Schematic illustration of a NOR logic gate built by cascaded OR and NOT gates (top) and optical image of the designed Ag NW structure (bottom). (a−c) Reprinted from ref 17. Copyright 2011 American Chemical Society. (d) Reprinted with permission from ref 18. Copyright 2011 Nature Publishing Group.

momentum flows at the NW tip, which couple directionally to the propagating plasmons on the NW and lead to a spin-dependent zigzag distribution on the metal NW. This spin-dependent zigzag distribution can also lead to plasmon routing in a branched NW, realizing the sorting of circularly polarized light in plasmonic circuits.[120] Figure 37a shows the simulated electric field distributions for an experimentally fabricated branched gold NW, excited using light beams with opposite circular polarizations. The simulation results are overlaid on the SEM image of the experimental sample, which clearly show the different circularly polarized photons are routed to separate branches, realizing the function of a spin sorter. The spin-sorting function of the simulated sample was experimentally proved, as shown in Figure 37b. The fabricated Y-branch structure was immersed into index-matching oil to get a

homogeneous dielectric environment. The polarization state of the excitation light was controlled by rotating a quarter-wave plate inserted into the path of the laser light. The SPs excited by circularly polarized light with opposite spins ($\theta = 45°$ and $135°$ in Figure 37c) were directed to different branches with the intensity ratio between the two output ports higher than 6:1. These results demonstrate a novel approach to loading and sorting optical information, encoded in the spin degree of freedom of photons, in plasmonic nanocircuits.

8.3. Logic Gates

The SPs propagating on plasmonic NWs preserve the coherence of the excitation light. When multiple mutually coherent laser beams are coupled to metal NWs, the multiple plasmon waves will interfere and modulate both the near-field distribution and the far-field output at the NW ends.[17,18,161,250]
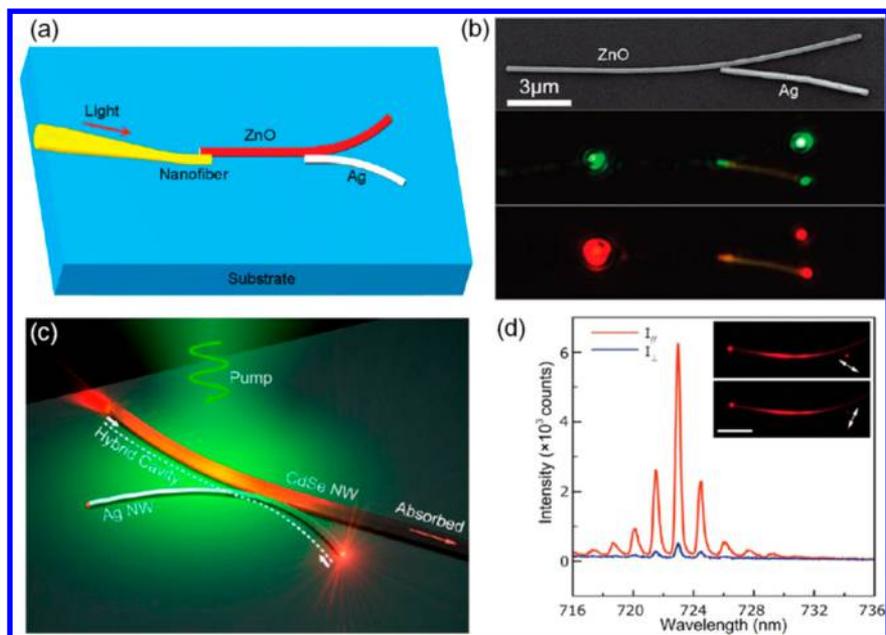
Figure 39. (a) Schematic of a hybrid coupler composed of coupled Ag and ZnO NWs. (b) (Top) SEM image of a hybrid coupler assembled from a 270 nm diameter ZnO NW and a 240 nm diameter Ag NW. (Middle and bottom) Optical micrographs of the hybrid coupler taken with the polarization parallel to the Ag NW when monochromatic lasers of wavelengths 532 and 650 nm are used as light sources. (c) Schematic illustration of a hybrid photon−plasmon NW laser composed of a Ag NW and an ultralong CdSe NW coupled into an X-shape. The right segment of the CdSe NW serves as a distributed absorber without reflection. (d) Polarization-sensitive lasing spectra from the Ag NW end-facet with the emission polarization oriented parallel (red line) and perpendicular (blue line) to the Ag NW. (Inset) Optical images showing the polarization-dependent lasing outputs. The scale bar is 10 μm. The white arrows indicate the directions of the polarization. (a and b) Reprinted from ref 75. Copyright 2009 American Chemical Society. (c and d) Reprinted from ref 253. Copyright 2013 American Chemical Society.

By controlling the interference of SPs in NW networks, interferometric logic gates can be realized.

For a branched NW structure shown in Figure 38a, two plasmon waves can be launched independently from terminals I1 and I2 in the system, with the remaining terminal O as output for the signal. The output results from coherent interference of SPs from the two input terminals, and the intensity depends on the phase difference of the two input beams [Figure 38a (iv, v)]. When the phase difference between input I1 and I2 increases monotonically, the output intensity at terminal O varies in an oscillating manner, as shown in Figure 38b. The strength of the plasmon interference can be described by visibility, defined as $(I_{max} - I_{min})/(I_{max} + I_{min})$, where I_{max} and I_{min} are the maximum and minimum values of the output intensity, respectively. The visibility depends on the polarization of the input light at terminal I1 and can be close to 1 under optimal polarization.[161]

The difference of the maximum and minimum output intensities is so large that they can be assigned as ON and OFF states, or 1 (true) and 0 (false) states for binary encoding, respectively. For the simple NW network shown in Figure 38a, either I1 or I2 input results in a "1" output, while both I1 and I2 inputs result in a "1" output for constructive interference. Hence, this three-terminal NW structure works as an OR gate. By setting a threshold intensity larger than the output intensity with only one input, this structure can work as an AND gate for constructive interference. For example, if the threshold intensity is set to 600, the output state is "0" for input at either I1 or I2, and the output state is "1" for inputs at both I1 and I2, which corresponds to the AND operation. For destructive interference, either I1 or I2 input results in a "1" output, while both I1 and I2 inputs result in a "0" output. This corresponds to an XOR gate. If one of the inputs is used as the

control signal, the input "0" is inverted to "1" and "1" is inverted to "0", so the structure realizes the function of the NOT gate. In such simple three-terminal NW network, a complete set of Boolean logic gates can be realized.[251]

For a more complex NW network with two input ends and two output ends, shown in Figure 38c, the plasmon interference with a varied phase difference can determine the plasmon routing between two output ends. The plasmon energy can be routed to the O1 terminal for certain input phases [Figure 38c (ii, iv)]. When the phase difference is increased, part of the energy is transferred to the O2 terminal. Further increasing the phase difference routes the plasmons to the O2 terminal [Figure 38c (iii, v)]. The QD fluorescence images show that the general intensity of the electric field on the two branches of the outputs switches between strong and weak in an alternating way, determining the switching of the output intensity at the two output terminals O1 and O2. Similar to the three-terminal structure in Figure 38a, by defining a threshold intensity for "1" and "0" states, this simple four-terminal NW network can function as a binary half adder. Inputs at both I1 and I2 result in output "1" at O2 and output "0" at O1: 1 + 1 = 10, while an input at only I1 or I2 results in "0" at O2 and "1" at O1: 1 + 0 = 0 + 1 = 01. This half adder function is realized because of the multiple plasmon modes in the NWs which enable destructive interference at O1 and constructive interference at O2.

To realize more complex logic functions, the elementary logic gates need to be cascaded. The cascade of plasmon-based interferometric logic gates was investigated by examining one of the universal logic gates, the NOR gate. A structure composed of three NWs was designed for the cascaded NOR gate, as shown in Figure 38d. The ends labeled I1 and I2 are the two input terminals, and the end labeled C is for the control signal,

that is, one of the inputs of the NOT gate. When the control signal is enabled, the NOT operation inverts the results of the OR operation, realizing the NOR function. These results show the potential of using plasmonic waveguide based structures for information processing in nanophotonic circuits.

8.4. Plasmonic-Photonic Hybrid Nanowire Devices

Plasmonic NW waveguides can support light propagation with tight field confinements, but the SPs suffer high energy losses. It is challenging to build on-chip integrated nanophotonic circuits with only metal nanowaveguides. This trade-off between mode size and propagation loss must be considered carefully. Hybridizing with photonic (dielectric or semiconductor) NWs is a possible strategy to decrease the energy losses during propagation, since the photonic waveguides have much lower losses in optical frequencies.

The hybrid structures consisting of Ag NWs and ZnO NWs or SnO$_2$ nanoribbons were experimentally investigated.[75,252] For a hybrid ZnO NW-Ag NW structure (Figure 9b), the light from a nanofiber can couple into the ZnO NW and then excite propagating SPs on the Ag NW connected to the ZnO NW. In a reverse process, the SPs on the Ag NW launched directly by the nanofiber can also couple to the ZnO NW. Figure 39a shows the schematic of a hybrid coupler composed of coupled Ag and ZnO NWs, which can be readily assembled in experiments by micromanipulation. The optical images in Figure 39b show that the light of 532 and 650 nm wavelength can efficiently couple from the ZnO NW to the Ag NW, as evidenced by the green and red light emission at the right end of the Ag NW. The coupling efficiency of light from the ZnO NW to the Ag NW at a 650 nm wavelength is about 82% after the propagation loss of the Ag NW is calibrated. By using coupled Ag and ZnO NWs, a Mach−Zehnder interferometer and a microring cavity were also demonstrated.

By coupling a Ag NW with a high-gain CdSe NW, a hybrid photon−plasmon NW laser was realized.[253] As schematically shown in Figure 39c, a Ag NW is side-coupled to a CdSe NW to form an X-shaped structure, and pumping light of 532 nm wavelength is loosely focused on the left part of the CdSe NW. The photoluminescence is guided along the CdSe NW until reaching the coupling region, where the photon modes of the CdSe NW are converted into plasmon modes of the Ag NW. The plasmon modes reflected at the right end of the Ag NW are then converted to photon modes of the CdSe NW at the coupling region. The left segment of the CdSe NW and the right segment of the Ag NW form a longitudinal hybrid cavity supporting interconvertible photon modes and plasmon modes. In the experiment, a hybrid cavity was assembled from a Ag NW of 100 nm diameter and a CdSe NW of 390 nm diameter on a MgF$_2$ substrate. With the increase of the pumping fluence, lasing emission was detected at both the right Ag NW end and the left CdSe NW end (inset of Figure 39d). The plasmon lasing output from the Ag NW end shows a high ratio of two orthogonal polarization components, as shown in Figure 39d. The output for polarization parallel to the Ag NW section is much stronger than that for the perpendicular polarization, consistent with the electromagnetic feature of the plasmon mode in a Ag NW of 100 nm diameter. The mode area of the Ag NW at the lasing wavelength of 723 nm is calculated to be 0.004 μm^2 (0.008λ^2), corresponding to a mode size of 70 nm, well below the optical diffraction limit.

9. CONCLUSIONS AND OUTLOOK

In this paper, we reviewed the developments of plasmon waveguiding in NWs, mainly metal NWs, and the coupling between plasmonic NWs and emitters. In addition, the hybrid plasmonic NW waveguide, composed of a semiconductor NW and a metal film with a thin insulator between them is also briefly discussed.

Metal NW supporting propagating SPs is a fundamental building block for plasmonic integrated circuits. The dispersion relations of plasmon modes in metal NWs reflect their larger wave vector and smaller group velocity compared with light in vacuum at the same frequency. The tight field confinement of SPs on the NW, manifested by the large wave vector, is also associated with high ohmic loss that limits the propagation distance. The SPs on the NWs can be excited and detected by optical and electrical means. The superposition of multiple plasmon modes in the NWs determines their particular propagation and emission behaviors. The periodic distributions of the electric field on the NWs originating from the excitation of multiple modes lead to zigzag or chiral propagation routes. The electric field distributions can be tuned by controlling the incident polarization, the dielectric environment, or the structural symmetry, providing methods to conveniently manipulate the plasmon guiding in NW networks. The interference of SPs generated by coherent light can also be used to modulate the SP propagation and emission. On the basis of the manipulations of SPs in NW structures, plasmonic nanophotonic devices can be realized. By coupling metal NWs with dielectric or semiconductor NWs, hybrid NW devices can also be developed.

Metal NWs can couple with QEs, providing a promising platform for quantum information processing. The exciton− plasmon interactions between single QEs and single plasmonic NWs have been demonstrated in different systems using various methods. As a result of the potentially large Purcell effect, photons spontaneously emitted from the QEs can be efficiently harvested by the plasmons on the NW and directed into a well-defined spatial mode, which can be exploited as efficient single photon sources. The exciton−plasmon coupling can provide a giant nonlinearity which may lead to the realization of optical switches, transistors, and entanglement of two qubits. The exciton−plasmon−photon interconversion in the NW-emitter hybrid structure also provides a new kind of remote excitation and remote detection technique, which is useful for optical imaging and sensing in chemical and biological systems.

The plasmons on metal NWs suffer high ohmic loss due to the concentration of electric field in the metal. To decrease the plasmon propagation loss while maintaining the tight field confinement, a hybrid plasmonic waveguide configuration was proposed, which consists of a semiconductor NW, a metal film, and an intervening ultrathin insulator. In this structure, the electric fields of hybrid plasmon modes are largely located in the insulator, thus the metal-induced ohmic loss is decreased, resulting in a longer propagation distance. By using a gain material for the semiconductor NW, this hybrid NW waveguide can be exploited for developing plasmonic lasers and amplifiers.

The strong dependence of the NW plasmons on the dielectric surroundings indicates that the properties of NW plasmons can be tailored by engineering the dielectric constants of the surrounding media. Active and reversible tuning of the refractive indices of the surrounding media is highly desired for

modulating the plasmon waveguiding and realizing plasmonic devices of different functions with high performance. Composite structures incorporating materials with special properties can certainly benefit the control of the NW plasmons. Schemes combining gain materials and metal NWs can be explored to compensate for the plasmon propagation loss. The development of advanced techniques for fabricating metal NWs of high crystalline quality and well-defined geometries will promote the progress of plasmon waveguiding in NW networks and related nanophotonic devices. Integrating plasmonic NWs with nanophotonic and nanoelectronic devices is promising for achieving high-performance nanophotonic devices and circuits.

The coupling between plasmonic NWs and emitters requires more precise engineering to achieve a higher coupling strength. NW-QE coupling structures with a strong Purcell effect, a high plasmon quantum yield, and a reasonable propagation length need to be carefully designed. To study the coupling of multiple QEs mediated by the plasmons on the NW, novel methods need to be explored to precisely position the QEs and controllably excite them. For hybrid NW waveguides, some fundamental questions regarding charge transport through the semiconductor–insulator–metal interfaces and enhanced stimulated emission cross section due to the strong mode confinement have been raised. The research on these issues may open new possibilities for the development of plasmonic devices and circuits.

AUTHOR INFORMATION

Corresponding Author
*E-mail: hxxu@whu.edu.cn.
ORCID
Shunping Zhang: 0000-0002-8491-0903
Ning Liu: 0000-0003-1164-6387
Hongxing Xu: 0000-0002-1718-8834

Notes
The authors declare no competing financial interest.

Biographies

Hong Wei is an associate professor at Institute of Physics, Chinese Academy of Sciences. She received her B.S. in physics from Shandong University, China, in 2004, and her Ph.D. from Institute of Physics, Chinese Academy of Sciences, in 2009. Her research interests include plasmonic waveguides and circuits, interactions of surface plasmons and excitons, surface-enhanced spectroscopy, and related applications in nano-optical devices.

Deng Pan received his B.S. from Northwest University, China, in 2009, and his M.S. from Nankai University, China, in 2012. After graduation with a Ph.D. degree from Institute of Physics, Chinese Academy of Sciences, in 2015, he joined Wuhan University as a research assistant, and he is currently working as a visiting scholar in ICFO-The Institute of Photonic Science, Barcelona. His research is centered on theory of nanophotonics, involving waveguiding optics, topological photonics, light-matter interaction on the quantum level, Casimir effect, near-field heat transfers, and optical excitations by electron beams.

Shunping Zhang received his B.S. degree in optics from Sun Yat-Sen University, China, in 2008 and obtained his Ph.D. degree from Institute of Physics, Chinese Academy of Sciences, in January 2013. After that, he continued to work in the Hongxing Xu group as a postdoc during 2013–2015. In April 2015, he got promoted to associate professor in School of Physics and Technology, Wuhan

University, China. His research interests include plasmonics and nanophotonics. Particularly, he focuses on light-matter interaction in nanocavities, plasmonic waveguiding, and ultrasensitive nanosensors.

Zhipeng Li received a B.S. degree in physics from Jilin University, China, in 2003, and a Ph.D. degree from Institute of Physics, Chinese Academy of Sciences, in 2008. After a research position at the Nanoscale Physics and Devices Laboratory of Institute of Physics, Chinese Academy of Sciences, he now works at Capital Normal University, China, as a professor in the Beijing Key Laboratory of Nano-Photonics and Nano-Structure. His current research interests include the quantum effect on plasmonic nanoantennas and ultrasensitive spectroscopy. He is a member of the international editorial board of Journal of Physics Communications.

Qiang Li received his B.S. in physics from Hebei Normal University, China, in 2008, his M.S. in optics from South China Normal University in 2011, and his Ph.D. in condensed matter physics from Institute of Physics, Chinese Academy of Science, in 2014. His doctoral work focused on the exciton–plasmon interaction between single quantum dots and silver nanowires. He became a postdoctoral fellow at the Department of Physics, Hong Kong University of Science and Technology, in 2015, where he studied the exciton–plasmon coupling using broadband ultrafast pump–probe spectroscopy. Since 2017, he has been a lecturer at South China Normal University. His current research is related to the anti-Brownian electrokinetic trapping technique and the exciton–plasmon interaction at single molecule level.

Ning Liu is currently a lecturer in nanophysics in the Department of Physics at the University of Limerick, Ireland. She received her B.S. degree in physics from Peking University, China, in 1999 and a Ph.D. degree in condensed matter physics from the University of California at Irvine in 2005 under the supervision of Prof Wilson Ho. Prior to joining the University of Limerick, Ireland, as a junior lecturer in 2013, she worked as postdoctoral research fellow in the UK, Canada, China, and Ireland. Her specialties are in scanning probe spectroscopy/microscopy and ultrafast spectroscopy/microscopy. Her current research interests focus on nanoplasmonics and nanophotonics, including gain-assisted surface plasmon propagation and electrically pumped nanocrystal light-emitting diodes.

Wenhui Wang is an assistant professor of physics at Xi'an Jiaotong University, China. She received her B.S. in physics from Northwestern Polytechnical University in 2006. She obtained her Ph.D. in condensed matter physics from the Institute of Physics, Chinese Academy of Sciences, in 2011. Her current research focuses on the optical and electronic properties of metal nanostructures and two-dimensional materials.

Hongxing Xu is a professor of physics and dean of School of Physics and Technology at Wuhan University, China. He is a member of Chinese Academy of Sciences. He received his B.S. from Peking University, China, in 1992, and his Ph.D. from Chalmers University of Technology, Sweden, in 2002, both in physics. He then joined the Division of Solid State Physics at Lund University, Sweden, as an assistant professor until December 2004. From 2005 to 2014, he was a professor at the Institute of Physics, Chinese Academy of Sciences. He is known for the discovery of nanogap effect for huge electromagnetic enhancement, the invention of plasmonic logic gates, and the development of plasmonic nanowire waveguides and circuits. His research interests include plasmonics, nanophotonics, surface-/tip-enhanced spectroscopy, and single molecule spectroscopy.

REFERENCES

(1) Ozbay, E. Plasmonics: Merging photonics and electronics at nanoscale dimensions. *Science* **2006**, *311*, 189−193.

(2) Sorger, V. J.; Oulton, R. F.; Ma, R. M.; Zhang, X. Toward integrated plasmonic circuits. *MRS Bull.* **2012**, *37*, 728−738.

(3) Maier, S. A. *Plasmonics: Fundamentals and Applications*; Springer, 2006.

(4) Wei, H.; Xu, H. X. Nanowire-based plasmonic waveguides and devices for integrated nanophotonic circuits. *Nanophotonics* **2012**, *1*, 155−169.

(5) Guo, X.; Ma, Y. G.; Wang, Y. P.; Tong, L. M. Nanowire plasmonic waveguides, circuits and devices. *Laser Photonics Rev.* **2013**, *7*, 855−881.

(6) Xiong, X.; Zou, C. L.; Ren, X. F.; Liu, A. P.; Ye, Y. X.; Sun, F. W.; Guo, G. C. Silver nanowires for photonics applications. *Laser Photonics Rev.* **2013**, *7*, 901−919.

(7) Takahara, J.; Yamagishi, S.; Taki, H.; Morimoto, A.; Kobayashi, T. Guiding of a one-dimensional optical beam with nanometer diameter. *Opt. Lett.* **1997**, *22*, 475−477.

(8) Novotny, L.; Hafner, C. Light-Propagation in a Cylindrical Wave-Guide with a Complex, Metallic, Dielectric Function. *Phys. Rev. E: Stat. Phys., Plasmas, Fluids, Relat. Interdiscip. Top.* **1994**, *50*, 4094−4106.

(9) Weeber, J. C.; Krenn, J. R.; Dereux, A.; Lamprecht, B.; Lacroute, Y.; Goudonnet, J. P. Near-field observation of surface plasmon polariton propagation on thin metal stripes. *Phys. Rev. B: Condens. Matter Mater. Phys.* **2001**, *64*, 045411.

(10) Zia, R.; Schuller, J. A.; Brongersma, M. L. Near-field characterization of guided polariton propagation and cutoff in surface plasmon waveguides. *Phys. Rev. B: Condens. Matter Mater. Phys.* **2006**, *74*, 165415.

(11) Pile, D. F. P.; Gramotnev, D. K. Channel plasmon-polariton in a triangular groove on a metal surface. *Opt. Lett.* **2004**, *29*, 1069−1071.

(12) Bozhevolnyi, S. I.; Volkov, V. S.; Devaux, E.; Laluet, J. Y.; Ebbesen, T. W. Channel plasmon subwavelength waveguide components including interferometers and ring resonators. *Nature* **2006**, *440*, 508−511.

(13) Cai, W. S.; Shin, W.; Fan, S. H.; Brongersma, M. L. Elements for Plasmonic Nanocircuits with Three-Dimensional Slot Waveguides. *Adv. Mater.* **2010**, *22*, 5120−5124.

(14) Steinberger, B.; Hohenau, A.; Ditlbacher, H.; Stepanov, A. L.; Drezet, A.; Aussenegg, F. R.; Leitner, A.; Krenn, J. R. Dielectric stripes on gold as surface plasmon waveguides. *Appl. Phys. Lett.* **2006**, *88*, 094104.

(15) Oulton, R. F.; Sorger, V. J.; Genov, D. A.; Pile, D. F. P.; Zhang, X. A hybrid plasmonic waveguide for subwavelength confinement and long-range propagation. *Nat. Photonics* **2008**, *2*, 496−500.

(16) Fang, Y. R.; Li, Z. P.; Huang, Y. Z.; Zhang, S. P.; Nordlander, P.; Halas, N. J.; Xu, H. X. Branched Silver Nanowires as Controllable Plasmon Routers. *Nano Lett.* **2010**, *10*, 1950−1954.

(17) Wei, H.; Li, Z. P.; Tian, X. R.; Wang, Z. X.; Cong, F. Z.; Liu, N.; Zhang, S. P.; Nordlander, P.; Halas, N. J.; Xu, H. X. Quantum Dot-Based Local Field Imaging Reveals Plasmon-Based Interferometric Logic in Silver Nanowire Networks. *Nano Lett.* **2011**, *11*, 471−475.

(18) Wei, H.; Wang, Z. X.; Tian, X. R.; Kall, M.; Xu, H. X. Cascaded logic gates in nanophotonic plasmon networks. *Nat. Commun.* **2011**, *2*, 387.

(19) Chang, D. E.; Sørensen, A. S.; Hemmer, P. R.; Lukin, M. D. Quantum optics with surface plasmons. *Phys. Rev. Lett.* **2006**, *97*, 053002.

(20) Akimov, A. V.; Mukherjee, A.; Yu, C. L.; Chang, D. E.; Zibrov, A. S.; Hemmer, P. R.; Park, H.; Lukin, M. D. Generation of single optical plasmons in metallic nanowires coupled to quantum dots. *Nature* **2007**, *450*, 402−406.

(21) Kolesov, R.; Grotz, B.; Balasubramanian, G.; Stohr, R. J.; Nicolet, A. A. L.; Hemmer, P. R.; Jelezko, F.; Wrachtrup, J. Wave-particle duality of single surface plasmon polaritons. *Nat. Phys.* **2009**, *5*, 470−474.

(22) Liu, N.; Wei, H.; Li, J.; Wang, Z. X.; Tian, X. R.; Pan, A. L.; Xu, H. X. Plasmonic Amplification with Ultra-High Optical Gain at Room Temperature. *Sci. Rep.* **2013**, *3*, 1967.

(23) Sun, Y. G.; Xia, Y. N. Large-scale synthesis of uniform silver nanowires through a soft, self-seeding, polyol process. *Adv. Mater.* **2002**, *14*, 833−837.

(24) Tao, A.; Kim, F.; Hess, C.; Goldberger, J.; He, R. R.; Sun, Y. G.; Xia, Y. N.; Yang, P. D. Langmuir-Blodgett silver nanowire monolayers for molecular sensing using surface-enhanced Raman spectroscopy. *Nano Lett.* **2003**, *3*, 1229−1233.

(25) Huang, Y. Z.; Wang, W. Z.; Liang, H. Y.; Wei, H.; Xu, H. X. Ultrasonic-Assisted Synthesis of Au Nanobelts and Nanowires. *J. Nanosci. Nanotechnol.* **2010**, *10*, 7515−7518.

(26) Kim, F.; Sohn, K.; Wu, J.; Huang, J. Chemical Synthesis of Gold Nanowires in Acidic Solutions. *J. Am. Chem. Soc.* **2008**, *130*, 14442−14443.

(27) Mohanty, P.; Yoon, I.; Kang, T.; Seo, K.; Varadwaj, K. S. K.; Choi, W.; Park, Q. H.; Ahn, J. P.; Suh, Y. D.; Ihee, H.; et al. Simple vapor-phase synthesis of single-crystalline Ag nanowires and single-nanowire surface-enhanced raman scattering. *J. Am. Chem. Soc.* **2007**, *129*, 9576−9577.

(28) Yoo, Y.; Seo, K.; Han, S.; Varadwaj, K. S. K.; Kim, H. Y.; Ryu, J. H.; Lee, H. M.; Ahn, J. P.; Ihee, H.; Kim, B. Steering Epitaxial Alignment of Au, Pd, and AuPd Nanowire Arrays by Atom Flux Change. *Nano Lett.* **2010**, *10*, 432−438.

(29) Kusar, P.; Gruber, C.; Hohenau, A.; Krenn, J. R. Measurement and Reduction of Damping in Plasmonic Nanowires. *Nano Lett.* **2012**, *12*, 661−665.

(30) Huang, J. S.; Callegari, V.; Geisler, P.; Bruning, C.; Kern, J.; Prangsma, J. C.; Wu, X. F.; Feichtner, T.; Ziegler, J.; Weinmann, P.; et al. Atomically flat single-crystalline gold nanostructures for plasmonic nanocircuitry. *Nat. Commun.* **2010**, *1*, 150.

(31) Geisler, P.; Krauss, E.; Razinskas, G.; Hecht, B. Transmission of Plasmons through a Nanowire. *ACS Photonics* **2017**, *4*, 1615−1620.

(32) Wiley, B. J.; Lipomi, D. J.; Bao, J. M.; Capasso, F.; Whitesides, G. M. Fabrication of surface plasmon resonators by nanoskiving single-crystalline gold microplates. *Nano Lett.* **2008**, *8*, 3023−3028.

(33) Jeong, D. H.; Zhang, Y. X.; Moskovits, M. Polarized surface enhanced Raman scattering from aligned silver nanowire rafts. *J. Phys. Chem. B* **2004**, *108*, 12724−12728.

(34) Martin, B. R.; Dermody, D. J.; Reiss, B. D.; Fang, M. M.; Lyon, L. A.; Natan, M. J.; Mallouk, T. E. Orthogonal self-assembly on colloidal gold-platinum nanorods. *Adv. Mater.* **1999**, *11*, 1021−1025.

(35) Mock, J. J.; Oldenburg, S. J.; Smith, D. R.; Schultz, D. A.; Schultz, S. Composite plasmon resonant nanowires. *Nano Lett.* **2002**, *2*, 465−469.

(36) Ditlbacher, H.; Hohenau, A.; Wagner, D.; Kreibig, U.; Rogers, M.; Hofer, F.; Aussenegg, F. R.; Krenn, J. R. Silver nanowires as surface plasmon resonators. *Phys. Rev. Lett.* **2005**, *95*, 257403.

(37) Laroche, T.; Vial, A.; Roussey, M. Crystalline structure's influence on the near-field optical properties of single plasmonic nanowires. *Appl. Phys. Lett.* **2007**, *91*, 123101.

(38) Oulton, R. F.; Bartal, G.; Pile, D. F. P.; Zhang, X. Confinement and propagation characteristics of subwavelength plasmonic modes. *New J. Phys.* **2008**, *10*, 105018.

(39) Chang, D. E.; Sørensen, A. S.; Hemmer, P. R.; Lukin, M. D. Strong coupling of single emitters to surface plasmons. *Phys. Rev. B: Condens. Matter Mater. Phys.* **2007**, *76*, 035420.

(40) Pan, D.; Wei, H.; Jia, Z. L.; Xu, H. X. Mode Conversion of Propagating Surface Plasmons in Nanophotonic Networks Induced by Structural Symmetry Breaking. *Sci. Rep.* **2014**, *4*, 4993.

(41) Wei, H.; Pan, D.; Xu, H. X. Routing of surface plasmons in silver nanowire networks controlled by polarization and coating. *Nanoscale* **2015**, *7*, 19053−19059.

(42) Shi, Z. W.; Hong, X. P.; Bechtel, H. A.; Zeng, B.; Martin, M. C.; Watanabe, K.; Taniguchi, T.; Shen, Y. R.; Wang, F. Observation of a Luttinger-liquid plasmon in metallic single-walled carbon nanotubes. *Nat. Photonics* **2015**, *9*, 515−519.

(43) Martin-Moreno, L.; García de Abajo, F. J.; Garcia-Vidal, F. J. Ultraefficient Coupling of a Quantum Emitter to the Tunable Guided Plasmons of a Carbon Nanotube. *Phys. Rev. Lett.* **2015**, *115*, 173601.

(44) Zhang, S. P.; Xu, H. X. Optimizing Substrate-Mediated Plasmon Coupling toward High-Performance Plasmonic Nanowire Waveguides. *ACS Nano* **2012**, *6*, 8128−8135.

(45) Li, Z. P.; Bao, K.; Fang, Y. R.; Guan, Z. Q.; Halas, N. J.; Nordlander, P.; Xu, H. X. Effect of a proximal substrate on plasmon propagation in silver nanowires. *Phys. Rev. B: Condens. Matter Mater. Phys.* **2010**, *82*, 241402.

(46) Zou, C. L.; Sun, F. W.; Xiao, Y. F.; Dong, C. H.; Chen, X. D.; Cui, J. M.; Gong, Q.; Han, Z. F.; Guo, G. C. Plasmon modes of silver nanowire on a silica substrate. *Appl. Phys. Lett.* **2010**, *97*, 183102.

(47) Shegai, T.; Miljkovic, V. D.; Bao, K.; Xu, H. X.; Nordlander, P.; Johansson, P.; Kall, M. Unidirectional Broadband Light Emission from Supported Plasmonic Nanowires. *Nano Lett.* **2011**, *11*, 706−711.

(48) Wang, Z. X.; Wei, H.; Pan, D.; Xu, H. X. Controlling the radiation direction of propagating surface plasmons on silver nanowires. *Laser Photonics Rev.* **2014**, *8*, 596−601.

(49) Jia, Z. L.; Wei, H.; Pan, D.; Xu, H. X. Direction-resolved radiation from polarization-controlled surface plasmon modes on silver nanowire antennas. *Nanoscale* **2016**, *8*, 20118−20124.

(50) Anderson, L. J. E.; Zhen, Y. R.; Payne, C. M.; Nordlander, P.; Hafner, J. H. Gold Nanobelts as High Confinement Plasmonic Waveguides. *Nano Lett.* **2013**, *13*, 6256−6261.

(51) Song, M. X.; Bouhelier, A.; Bramant, P.; Sharma, J.; Dujardin, E.; Zhang, D. G.; Colas-des-Francs, G. Imaging Symmetry-Selected Corner Plasmon Modes in Penta-Twinned Crystalline Ag Nanowires. *ACS Nano* **2011**, *5*, 5874−5880.

(52) Nauert, S.; Paul, A.; Zhen, Y. R.; Solis, D.; Vigderman, L.; Chang, W. S.; Zubarev, E. R.; Nordlander, P.; Link, S. Influence of Cross Sectional Geometry on Surface Plasmon Polariton Propagation in Gold Nanowires. *ACS Nano* **2014**, *8*, 572−580.

(53) Heeres, R. W.; Kouwenhoven, L. P.; Zwiller, V. Quantum interference in plasmonic circuits. *Nat. Nanotechnol.* **2013**, *8*, 719−722.

(54) García de Abajo, F. J. Optical excitations in electron microscopy. *Rev. Mod. Phys.* **2010**, *82*, 209−275.

(55) Nelayah, J.; Kociak, M.; Stephan, O.; García de Abajo, F. J.; Tence, M.; Henrard, L.; Taverna, D.; Pastoriza-Santos, I.; Liz-Marzan, L. M.; Colliex, C. Mapping surface plasmons on a single metallic nanoparticle. *Nat. Phys.* **2007**, *3*, 348−353.

(56) Rossouw, D.; Botton, G. A. Plasmonic Response of Bent Silver Nanowires for Nanophotonic Subwavelength Waveguiding. *Phys. Rev. Lett.* **2013**, *110*, 066801.

(57) Cai, W.; Sainidou, R.; Xu, J. J.; Polman, A.; García de Abajo, F. J. Efficient Generation of Propagating Plasmons by Electron Beams. *Nano Lett.* **2009**, *9*, 1176−1181.

(58) Bharadwaj, P.; Bouhelier, A.; Novotny, L. Electrical Excitation of Surface Plasmons. *Phys. Rev. Lett.* **2011**, *106*, 226802.

(59) Lambe, J.; McCarthy, S. L. Light-Emission from Inelastic Electron-Tunneling. *Phys. Rev. Lett.* **1976**, *37*, 923−925.

(60) Gimzewski, J. K.; Sass, J. K.; Schlitter, R. R.; Schott, J. Enhanced Photon-Emission in Scanning Tunnelling Microscopy. *Europhys. Lett.* **1989**, *8*, 435−440.

(61) Berndt, R.; Gimzewski, J. K.; Johansson, P. Inelastic Tunneling Excitation of Tip-Induced Plasmon Modes on Noble-Metal Surfaces. *Phys. Rev. Lett.* **1991**, *67*, 3796−3799.

(62) Weeber, J. C.; Dereux, A.; Girard, C.; Krenn, J. R.; Goudonnet, J. P. Plasmon polaritons of metallic nanowires for controlling

submicron propagation of light. *Phys. Rev. B: Condens. Matter Mater. Phys.* **1999**, *60*, 9061−9068.

(63) Sanders, A. W.; Routenberg, D. A.; Wiley, B. J.; Xia, Y. N.; Dufresne, E. R.; Reed, M. A. Observation of plasmon propagation, redirection, and fan-out in silver nanowires. *Nano Lett.* **2006**, *6*, 1822−1826.

(64) Knight, M. W.; Grady, N. K.; Bardhan, R.; Hao, F.; Nordlander, P.; Halas, N. J. Nanoparticle-mediated coupling of light into a nanowire. *Nano Lett.* **2007**, *7*, 2346−2350.

(65) Yang, C.; Pan, D.; Tong, L. M.; Xu, H. X. Guided transport of nanoparticles by plasmonic nanowires. *Nanoscale* **2016**, *8*, 19195−19199.

(66) Zhu, Y.; Wei, H.; Yang, P. F.; Xu, H. X. Controllable Excitation of Surface Plasmons in End-to-Trunk Coupled Silver Nanowire Structures. *Chin. Phys. Lett.* **2012**, *29*, 077302.

(67) Liu, N.; Li, Z. P.; Xu, H. X. Polarization-Dependent Study on Propagating Surface Plasmons in Silver Nanowires Launched by a Near-Field Scanning Optical Fiber Tip. *Small* **2012**, *8*, 2641−2646.

(68) Pyayt, A. L.; Wiley, B.; Xia, Y. N.; Chen, A.; Dalton, L. Integration of photonic and silver nanowire plasmonic waveguides. *Nat. Nanotechnol.* **2008**, *3*, 660−665.

(69) Dickson, R. M.; Lyon, L. A. Unidirectional plasmon propagation in metallic nanowires. *J. Phys. Chem. B* **2000**, *104*, 6095−6098.

(70) Zhang, S. P.; Wei, H.; Bao, K.; Hakanson, U.; Halas, N. J.; Nordlander, P.; Xu, H. X. Chiral Surface Plasmon Polaritons on Metallic Nanowires. *Phys. Rev. Lett.* **2011**, *107*, 096801.

(71) Li, Z. P.; Bao, K.; Fang, Y. R.; Huang, Y. Z.; Nordlander, P.; Xu, H. X. Correlation between Incident and Emission Polarization in Nanowire Surface Plasmon Waveguides. *Nano Lett.* **2010**, *10*, 1831−1835.

(72) Huang, J. S.; Feichtner, T.; Biagioni, P.; Hecht, B. Impedance Matching and Emission Properties of Nanoantennas in an Optical Nanocircuit. *Nano Lett.* **2009**, *9*, 1897−1902.

(73) Fang, Z. Y.; Fan, L. R.; Lin, C. F.; Zhang, D.; Meixner, A. J.; Zhu, X. Plasmonic Coupling of Bow Tie Antennas with Ag Nanowire. *Nano Lett.* **2011**, *11*, 1676−1680.

(74) Zhang, S. P.; Gu, C. Z.; Xu, H. X. Single Nanoparticle Couplers for Plasmonic Waveguides. *Small* **2014**, *10*, 4264−4269.

(75) Guo, X.; Qiu, M.; Bao, J. M.; Wiley, B. J.; Yang, Q.; Zhang, X. N.; Ma, Y. G.; Yu, H. K.; Tong, L. M. Direct Coupling of Plasmonic and Photonic Nanowires for Hybrid Nanophotonic Components and Circuits. *Nano Lett.* **2009**, *9*, 4515−4519.

(76) Dong, C. H.; Ren, X. F.; Yang, R.; Duan, J. Y.; Guan, J. G.; Guo, G. C.; Guo, G. P. Coupling of light from an optical fiber taper into silver nanowires. *Appl. Phys. Lett.* **2009**, *95*, 221109.

(77) Li, X. Y.; Li, W.; Guo, X.; Lou, J. Y.; Tong, L. M. All-fiber hybrid photon-plasmon circuits: integrating nanowire plasmonics with fiber optics. *Opt. Express* **2013**, *21*, 15698−15705.

(78) Chen, X. W.; Sandoghdar, V.; Agio, M. Highly Efficient Interfacing of Guided Plasmons and Photons in Nanowires. *Nano Lett.* **2009**, *9*, 3756−3761.

(79) Chen, X. W.; Sandoghdar, V.; Agio, M. Nanofocusing radially-polarized beams for high-throughput funneling of optical energy to the near field. *Opt. Express* **2010**, *18*, 10878−10887.

(80) Verhagen, E.; Spasenovic, M.; Polman, A.; Kuipers, L. Nanowire Plasmon Excitation by Adiabatic Mode Transformation. *Phys. Rev. Lett.* **2009**, *102*, 203904.

(81) Hu, Q.; Xu, D. H.; Zhou, Y.; Peng, R. W.; Fan, R. H.; Fang, N. X.; Wang, Q. J.; Huang, X. R.; Wang, M. Position-sensitive spectral splitting with a plasmonic nanowire on silicon chip. *Sci. Rep.* **2013**, *3*, 3095.

(82) Zhang, X. N.; Ma, Z.; Luo, R.; Gu, Y.; Meng, C.; Wu, X. Q.; Gong, Q. H.; Tong, L. M. Single-nanowire surface plasmon gratings. *Nanotechnology* **2012**, *23*, 225202.

(83) de Leon, N. P.; Shields, B. J.; Yu, C. L.; Englund, D. E.; Akimov, A. V.; Lukin, M. D.; Park, H. Tailoring Light-Matter Interaction with a Nanoscale Plasmon Resonator. *Phys. Rev. Lett.* **2012**, *108*, 226803.

(84) Cao, H.; Nahata, A. Coupling of terahertz pulses onto a single metal wire waveguide using milled grooves. *Opt. Express* **2005**, *13*, 7028−7034.

(85) Wang, K. L.; Mittleman, D. M. Dispersion of surface plasmon polaritons on metal wires in the terahertz frequency range. *Phys. Rev. Lett.* **2006**, *96*, 157401.

(86) Fan, P. Y.; Colombo, C.; Huang, K. C. Y.; Krogstrup, P.; Nygard, J.; Fontcuberta i Morral, A.; Brongersma, M. L. An Electrically-Driven GaAs Nanowire Surface Plasmon Source. *Nano Lett.* **2012**, *12*, 4943−4947.

(87) Rai, P.; Hartmann, N.; Berthelot, J.; Arocas, J.; Colas des Francs, G.; Hartschuh, A.; Bouhelier, A. Electrical Excitation of Surface Plasmons by an Individual Carbon Nanotube Transistor. *Phys. Rev. Lett.* **2013**, *111*, 026804.

(88) Li, Q.; Wei, H.; Xu, H. X. Quantum Yield of Single Surface Plasmons Generated by a Quantum Dot Coupled with a Silver Nanowire. *Nano Lett.* **2015**, *15*, 8181−8187.

(89) García de Abajo, F. J.; Kociak, M. Probing the photonic local density of states with electron energy loss spectroscopy. *Phys. Rev. Lett.* **2008**, *100*, 106804.

(90) Schoen, D. T.; Atre, A. C.; Garcia-Etxarri, A.; Dionne, J. A.; Brongersma, M. L. Probing Complex Reflection Coefficients in One-Dimensional Surface Plasmon Polariton Waveguides and Cavities Using STEM EELS. *Nano Lett.* **2015**, *15*, 120−126.

(91) Rossouw, D.; Couillard, M.; Vickery, J.; Kumacheva, E.; Botton, G. A. Multipolar Plasmonic Resonances in Silver Nanowire Antennas Imaged with a Subnanometer Electron Probe. *Nano Lett.* **2011**, *11*, 1499−1504.

(92) Guiton, B. S.; Iberi, V.; Li, S. Z.; Leonard, D. N.; Parish, C. M.; Kotula, P. G.; Varela, M.; Schatz, G. C.; Pennycook, S. J.; Camden, J. P. Correlated Optical Measurements and Plasmon Mapping of Silver Nanorods. *Nano Lett.* **2011**, *11*, 3482−3488.

(93) Nicoletti, O.; Wubs, M.; Mortensen, N. A.; Sigle, W.; van Aken, P. A.; Midgley, P. A. Surface plasmon modes of a single silver nanorod: an electron energy loss study. *Opt. Express* **2011**, *19*, 15371−15379.

(94) Vesseur, E. J. R.; de Waele, R.; Kuttge, M.; Polman, A. Direct observation of plasmonic modes in Au nanowires using high-resolution cathodoluminescence Spectroscopy. *Nano Lett.* **2007**, *7*, 2843−2846.

(95) Douillard, L.; Charra, F.; Korczak, Z.; Bachelot, R.; Kostcheev, S.; Lerondel, G.; Adam, P. M.; Royer, P. Short range plasmon resonators probed by photoemission electron microscopy. *Nano Lett.* **2008**, *8*, 935−940.

(96) Razinskas, G.; Kilbane, D.; Melchior, P.; Geisler, P.; Krauss, E.; Mathias, S.; Hecht, B.; Aeschlimann, M. Normal-Incidence PEEM Imaging of Propagating Modes in a Plasmonic Nanocircuit. *Nano Lett.* **2016**, *16*, 6832−6837.

(97) Piazza, L.; Lummen, T. T. A.; Quinonez, E.; Murooka, Y.; Reed, B. W.; Barwick, B.; Carbone, F. Simultaneous observation of the quantization and the interference pattern of a plasmonic near-field. *Nat. Commun.* **2015**, *6*, 6407.

(98) Zhang, S. P.; Chen, L.; Huang, Y. Z.; Xu, H. X. Reduced linewidth multipolar plasmon resonances in metal nanorods and related applications. *Nanoscale* **2013**, *5*, 6985−6991.

(99) Schider, G.; Krenn, J. R.; Hohenau, A.; Ditlbacher, H.; Leitner, A.; Aussenegg, F. R.; Schaich, W. L.; Puscasu, I.; Monacelli, B.; Boreman, G. Plasmon dispersion relation of Au and Ag nanowires. *Phys. Rev. B: Condens. Matter Mater. Phys.* **2003**, *68*, 155427.

(100) Allione, M.; Temnov, V. V.; Fedutik, Y.; Woggon, U.; Artemyev, M. V. Surface plasmon mediated interference phenomena in low-Q silver nanowire cavities. *Nano Lett.* **2008**, *8*, 31−35.

(101) Krenn, J. R.; Lamprecht, B.; Ditlbacher, H.; Schider, G.; Salerno, M.; Leitner, A.; Aussenegg, F. R. Non diffraction-limited light transport by gold nanowires. *Europhys. Lett.* **2002**, *60*, 663−669.

(102) Jones, A. C.; Olmon, R. L.; Skrabalak, S. E.; Wiley, B. J.; Xia, Y. N. N.; Raschke, M. B. Mid-IR Plasmonics: Near-Field Imaging of Coherent Plasmon Modes of Silver Nanowires. *Nano Lett.* **2009**, *9*, 2553−2558.

(103) Dorfmuller, J.; Vogelgesang, R.; Weitz, R. T.; Rockstuhl, C.; Etrich, C.; Pertsch, T.; Lederer, F.; Kern, K. Fabry-Perot Resonances in One-Dimensional Plasmonic Nanostructures. *Nano Lett.* **2009**, *9*, 2372−2377.

(104) Lim, J. K.; Imura, K.; Nagahara, T.; Kim, S. K.; Okamoto, H. Imaging and dispersion relations of surface plasmon modes in silver nanorods by near-field spectroscopy. *Chem. Phys. Lett.* **2005**, *412*, 41−45.

(105) Imura, K.; Nagahara, T.; Okamoto, H. Plasmon mode imaging of single gold nanorods. *J. Am. Chem. Soc.* **2004**, *126*, 12730−12731.

(106) Frimmer, M.; Chen, Y. T.; Koenderink, A. F. Scanning Emitter Lifetime Imaging Microscopy for Spontaneous Emission Control. *Phys. Rev. Lett.* **2011**, *107*, 123602.

(107) Schell, A. W.; Engel, P.; Werra, J. F. M.; Wolff, C.; Busch, K.; Benson, O. Scanning Single Quantum Emitter Fluorescence Lifetime Imaging: Quantitative Analysis of the Local Density of Photonic States. *Nano Lett.* **2014**, *14*, 2623−2627.

(108) Falk, A. L.; Koppens, F. H. L.; Yu, C. L.; Kang, K.; de Leon Snapp, N.; Akimov, A. V.; Jo, M. H.; Lukin, M. D.; Park, H. Near-field electrical detection of optical plasmons and single-plasmon sources. *Nat. Phys.* **2009**, *5*, 475−479.

(109) Goodfellow, K. M.; Chakraborty, C.; Beams, R.; Novotny, L.; Vamivakas, A. N. Direct On-Chip Optical Plasmon Detection with an Atomically Thin Semiconductor. *Nano Lett.* **2015**, *15*, 5477−5481.

(110) Lee, H. S.; Luong, D. H.; Kim, M. S.; Jin, Y.; Kim, H.; Yun, S.; Lee, Y. H. Reconfigurable exciton-plasmon interconversion for nanophotonic circuits. *Nat. Commun.* **2016**, *7*, 13663.

(111) Heeres, R. W.; Dorenbos, S. N.; Koene, B.; Solomon, G. S.; Kouwenhoven, L. P.; Zwiller, V. On-Chip Single Plasmon Detection. *Nano Lett.* **2010**, *10*, 661−664.

(112) Ittah, N.; Selzer, Y. Electrical Detection of Surface Plasmon Polaritons by 1G(0) Gold Quantum Point Contacts. *Nano Lett.* **2011**, *11*, 529−534.

(113) Wei, H.; Zhang, S. P.; Tian, X. R.; Xu, H. X. Highly tunable propagating surface plasmons on supported silver nanowires. *Proc. Natl. Acad. Sci. U. S. A.* **2013**, *110*, 4494−4499.

(114) Chen, C. M.; Young, C. K.; Chen, K. R.; Lan, Y. C. Spiral surface plasmon modes on uniform and tapered metallic nanorods. *J. Opt. Soc. Am. B* **2013**, *30*, 2529−2534.

(115) Rodriguez-Fortuno, F. J.; Marino, G.; Ginzburg, P.; O'Connor, D.; Martinez, A.; Wurtz, G. A.; Zayats, A. V. Near-Field Interference for the Unidirectional Excitation of Electromagnetic Guided Modes. *Science* **2013**, *340*, 328−330.

(116) Lin, J.; Mueller, J. P. B.; Wang, Q.; Yuan, G. H.; Antoniou, N.; Yuan, X. C.; Capasso, F. Polarization-Controlled Tunable Directional Coupling of Surface Plasmon Polaritons. *Science* **2013**, *340*, 331−334.

(117) Yin, X. B.; Ye, Z. L.; Rho, J.; Wang, Y.; Zhang, X. Photonic Spin Hall Effect at Metasurfaces. *Science* **2013**, *339*, 1405−1407.

(118) Shitrit, N.; Yulevich, I.; Maguid, E.; Ozeri, D.; Veksler, D.; Kleiner, V.; Hasman, E. Spin-Optical Metamaterial Route to Spin-Controlled Photonics. *Science* **2013**, *340*, 724−726.

(119) Petersen, J.; Volz, J.; Rauschenbeutel, A. Chiral nanophotonic waveguide interface based on spin-orbit interaction of light. *Science* **2014**, *346*, 67−71.

(120) Pan, D.; Wei, H.; Gao, L.; Xu, H. X. Strong Spin-Orbit Interaction of Light in Plasmonic Nanostructures and Nanocircuits. *Phys. Rev. Lett.* **2016**, *117*, 166803.

(121) Dai, W. H.; Lin, F. C.; Huang, C. B.; Huang, J. S. Mode Conversion in High-Definition Plasmonic Optical Nanocircuits. *Nano Lett.* **2014**, *14*, 3881−3886.

(122) Liu, M. Z.; Pelton, M.; Guyot-Sionnest, P. Reduced damping of surface plasmons at low temperatures. *Phys. Rev. B: Condens. Matter Mater. Phys.* **2009**, *79*, 035418.

(123) Bouillard, J. S. G.; Dickson, W.; O'Connor, D. P.; Wurtz, G. A.; Zayats, A. V. Low-Temperature Plasmonics of Metallic Nanostructures. *Nano Lett.* **2012**, *12*, 1561−1565.

(124) Wang, Y. P.; Ma, Y. G.; Guo, X.; Tong, L. M. Single-mode plasmonic waveguiding properties of metal nanowires with dielectric substrates. *Opt. Express* **2012**, *20*, 19006−19015.

(125) Li, Q.; Qiu, M. Plasmonic wave propagation in silver nanowires: guiding modes or not? *Opt. Express* **2013**, *21*, 8587−8595.

(126) Bian, Y. S.; Gong, Q. H. Metallic-nanowire-loaded silicon-on-insulator structures: a route to low-loss plasmon waveguiding on the nanoscale. *Nanoscale* **2015**, 7, 4415−4422.

(127) Wang, W. H.; Yang, Q.; Fan, F. R.; Xu, H. X.; Wang, Z. L. Light Propagation in Curved Silver Nanowire Plasmonic Waveguides. *Nano Lett.* **2011**, 11, 1603−1608.

(128) Yang, H. B.; Qiu, M.; Li, Q. Identification and control of multiple leaky plasmon modes in silver nanowires. *Laser Photonics Rev.* **2016**, 10, 278−286.

(129) Yu, K.; Devadas, M. S.; Major, T. A.; Lo, S. S.; Hartland, G. V. Surface Plasmon Polariton Propagation and Coupling in Gold Nanostructures. *J. Phys. Chem. C* **2014**, 118, 8603−8609.

(130) Lo, S. S.; Shi, H. Y.; Huang, L. B.; Hartland, G. V. Imaging the extent of plasmon excitation in Au nanowires using pump-probe microscopy. *Opt. Lett.* **2013**, 38, 1265−1267.

(131) Wild, B.; Cao, L. N.; Sun, Y. G.; Khanal, B. P.; Zubarev, E. R.; Gray, S. K.; Scherer, N. F.; Pelton, M. Propagation Lengths and Group Velocities of Plasmons in Chemically Synthesized Gold and Silver Nanowires. *ACS Nano* **2012**, 6, 472−482.

(132) Solis, D.; Chang, W. S.; Khanal, B. P.; Bao, K.; Nordlander, P.; Zubarev, E. R.; Link, S. Bleach-Imaged Plasmon Propagation (BlIPP) in Single Gold Nanowires. *Nano Lett.* **2010**, 10, 3482−3485.

(133) Ma, Y. G.; Li, X. Y.; Yu, H. K.; Tong, L. M.; Gu, Y.; Gong, Q. H. Direct measurement of propagation losses in silver nanowires. *Opt. Lett.* **2010**, 35, 1160−1162.

(134) Li, X. Y.; Guo, X.; Wang, D. L.; Tong, L. M. Propagation losses in gold nanowires. *Opt. Commun.* **2014**, 323, 119−122.

(135) Kim, S.; Bailey, S.; Liu, M.; Yan, R. X. Decoupling co-existing surface plasmon polariton (SPP) modes in a nanowire plasmonic waveguide for quantitative mode analysis. *Nano Res.* **2017**, 10, 2395−2404.

(136) Shegai, T.; Huang, Y. Z.; Xu, H. X.; Kall, M. Coloring fluorescence emission with silver nanowires. *Appl. Phys. Lett.* **2010**, 96, 103114.

(137) Hofstetter, D.; Thornton, R. L. Theory of loss measurements of Fabry-Perot resonators by Fourier analysis of the transmission spectra. *Opt. Lett.* **1997**, 22, 1831−1833.

(138) Notomi, M.; Yamada, K.; Shinya, A.; Takahashi, J.; Takahashi, C.; Yokohama, I. Extremely large group-velocity dispersion of line-defect waveguides in photonic crystal slabs. *Phys. Rev. Lett.* **2001**, 87, 253902.

(139) Temnov, V. V.; Woggon, U.; Dintinger, J.; Devaux, E.; Ebbesen, T. W. Surface plasmon interferometry: measuring group velocity of surface plasmons. *Opt. Lett.* **2007**, 32, 1235−1237.

(140) Rewitz, C.; Keitzl, T.; Tuchscherer, P.; Huang, J.; Geisler, P.; Razinskas, G.; Hecht, B.; Brixner, T. Ultrafast Plasmon Propagation in Nanowires Characterized by Far-Field Spectral Interferometry. *Nano Lett.* **2012**, 12, 45.

(141) Lepetit, L.; Cheriaux, G.; Joffre, M. Linear techniques of phase measurement by femtosecond spectral interferometry for applications in spectroscopy. *J. Opt. Soc. Am. B* **1995**, 12, 2467−2474.

(142) Pan, D.; Wei, H.; Xu, H. X. Metallic nanowires for subwavelength waveguiding and nanophotonic devices. *Chin. Phys. B* **2013**, 22, 097305.

(143) Li, Z. P.; Hao, F.; Huang, Y. Z.; Fang, Y. R.; Nordlander, P.; Xu, H. X. Directional Light Emission from Propagating Surface Plasmons of Silver Nanowires. *Nano Lett.* **2009**, 9, 4383−4386.

(144) Wei, H.; Tian, X. R.; Pan, D.; Chen, L.; Jia, Z. L.; Xu, H. X. Directionally-Controlled Periodic Collimated Beams of Surface Plasmon Polaritons on Metal Film in Ag Nanowire/Al₂O₃/Ag Film Composite Structure. *Nano Lett.* **2015**, 15, 560−564.

(145) Purcell, E. M. Spontaneous Emission Probabilities at Radio Frequencies. *Phys. Rev.* **1946**, 69, 681.

(146) Pelton, M. Modified spontaneous emission in nanophotonic structures. *Nat. Photonics* **2015**, 9, 427−435.

(147) Xu, H. X.; Bjerneld, E. J.; Kall, M.; Borjesson, L. Spectroscopy of single hemoglobin molecules by surface enhanced Raman scattering. *Phys. Rev. Lett.* **1999**, 83, 4357−4360.

(148) Xu, H. X.; Aizpurua, J.; Kall, M.; Apell, P. Electromagnetic contributions to single-molecule sensitivity in surface-enhanced Raman scattering. *Phys. Rev. E: Stat. Phys., Plasmas, Fluids, Relat. Interdiscip. Top.* **2000**, 62, 4318−4324.

(149) Kühn, S.; Håkanson, U.; Rogobete, L.; Sandoghdar, V. Enhancement of single-molecule fluorescence using a gold nano-particle as an optical nanoantenna. *Phys. Rev. Lett.* **2006**, 97, 017402.

(150) Anger, P.; Bharadwaj, P.; Novotny, L. Enhancement and quenching of single-molecule fluorescence. *Phys. Rev. Lett.* **2006**, 96, 113002.

(151) Kulakovich, O.; Strekal, N.; Yaroshevich, A.; Maskevich, S.; Gaponenko, S.; Nabiev, I.; Woggon, U.; Artemyev, M. Enhanced luminescence of CdSe quantum dots on gold colloids. *Nano Lett.* **2002**, 2, 1449−1452.

(152) Pompa, P. P.; Martiradonna, L.; Torre, A. D.; Sala, F. D.; Manna, L.; De Vittorio, M.; Calabi, F.; Cingolani, R.; Rinaldi, R. Metal-enhanced fluorescence of colloidal nanocrystals with nanoscale control. *Nat. Nanotechnol.* **2006**, 1, 126−130.

(153) Ming, T.; Chen, H. J.; Jiang, R. B.; Li, Q.; Wang, J. F. Plasmon-Controlled Fluorescence: Beyond the Intensity Enhancement. *J. Phys. Chem. Lett.* **2012**, 3, 191−202.

(154) Munechika, K.; Chen, Y.; Tillack, A. F.; Kulkarni, A. P.; Plante, I. J. L.; Munro, A. M.; Ginger, D. S. Spectral Control of Plasmonic Emission Enhancement from Quantum Dots near Single Silver Nanoprisms. *Nano Lett.* **2010**, 10, 2598−2603.

(155) Taminiau, T. H.; Stefani, F. D.; Segerink, F. B.; Van Hulst, N. F. Optical antennas direct single-molecule emission. *Nat. Photonics* **2008**, 2, 234−237.

(156) Curto, A. G.; Volpe, G.; Taminiau, T. H.; Kreuzer, M. P.; Quidant, R.; van Hulst, N. F. Unidirectional Emission of a Quantum Dot Coupled to a Nanoantenna. *Science* **2010**, 329, 930−933.

(157) Novotny, L.; van Hulst, N. Antennas for light. *Nat. Photonics* **2011**, 5, 83−90.

(158) Michler, P.; Kiraz, A.; Becher, C.; Schoenfeld, W. V.; Petroff, P. M.; Zhang, L. D.; Hu, E.; Imamoglu, A. A quantum dot single-photon turnstile device. *Science* **2000**, 290, 2282−2285.

(159) Taylor, J. M.; Marcus, C. M.; Lukin, M. D. Long-lived memory for mesoscopic quantum bits. *Phys. Rev. Lett.* **2003**, 90, 206803.

(160) Wei, H.; Ratchford, D.; Li, X. Q.; Xu, H. X.; Shih, C. K. Propagating Surface Plasmon Induced Photon Emission from Quantum Dots. *Nano Lett.* **2009**, 9, 4168−4171.

(161) Wei, H.; Xu, H. X. Controlling surface plasmon interference in branched silver nanowire structures. *Nanoscale* **2012**, 4, 7149−7154.

(162) Fedutik, Y.; Temnov, V. V.; Schops, O.; Woggon, U.; Artemyev, M. V. Exciton-plasmon-photon conversion in plasmonic nanostructures. *Phys. Rev. Lett.* **2007**, 99, 136802.

(163) Goodfellow, K. M.; Beams, R.; Chakraborty, C.; Novotny, L.; Vamivakas, A. N. Integrated nanophotonics based on nanowire plasmons and atomically thin material. *Optica* **2014**, 1, 149−152.

(164) Wang, L.-L.; Zou, C.-L.; Ren, X.-F.; Liu, A.-P.; Lv, L.; Cai, Y.-J.; Sun, F.-W.; Guo, G.-C.; Guo, G.-P. Exciton-plasmon-photon conversion in silver nanowire: Polarization dependence. *Appl. Phys. Lett.* **2011**, 99, 061103.

(165) Fu, M.; Qian, L. H.; Long, H.; Wang, K.; Lu, P. X.; Rakovich, Y. P.; Hetsch, F.; Susha, A. S.; Rogach, A. L. Tunable plasmon modes in single silver nanowire optical antennas characterized by far-field microscope polarization spectroscopy. *Nanoscale* **2014**, 6, 9192−9197.

(166) Lu, L.; Wang, L. L.; Zou, C. L.; Ren, X. F.; Dong, C. H.; Sun, F. W.; Yu, S. H.; Guo, G. C. Doubly and Triply Coupled Nanowire Antennas. *J. Phys. Chem. C* **2012**, 116, 23779−23784.

(167) Dasgupta, A.; Singh, D.; Tripathi, R. P. N.; Kumar, G. V. P. Directional Fluorescence Emission Mediated by Chemically-Prepared Plasmonic Nanowire Junctions. *J. Phys. Chem. C* **2016**, 120, 17692−17698.

(168) Hartmann, N.; Piatkowski, D.; Ciesielski, R.; Mackowski, S.; Hartschuh, A. Radiation Channels Close to a Plasmonic Nanowire Visualized by Back Focal Plane Imaging. *ACS Nano* **2013**, 7, 10257−10262.

(169) Lee, H. S.; Kim, M. S.; Jin, Y.; Han, G. H.; Lee, Y. H.; Kim, J. Selective Amplification of the Primary Exciton in a MoS_2 Monolayer. *Phys. Rev. Lett.* **2015**, *115*, 226801.

(170) Kress, S. J. P.; Antolinez, F. V.; Richner, P.; Jayanti, S. V.; Kim, D. K.; Prins, F.; Riedinger, A.; Fischer, M. P. C.; Meyer, S.; McPeak, K. M.; et al. Wedge Waveguides and Resonators for Quantum Plasmonics. *Nano Lett.* **2015**, *15*, 6267−6275.

(171) Bermudez-Urena, E.; Gonzalez-Ballestero, C.; Geiselmann, M.; Marty, R.; Radko, I. P.; Holmgaard, T.; Alaverdyan, Y.; Moreno, E.; Garcia-Vidal, F. J.; Bozhevolnyi, S. I.; et al. Coupling of individual quantum emitters to channel plasmons. *Nat. Commun.* **2015**, *6*, 7883.

(172) Pines, D. A Collective Description of Electron Interactions: IV. Electron Interaction in Metals. *Phys. Rev.* **1953**, *92*, 626−636.

(173) Tame, M. S.; McEnery, K. R.; Ozdemir, S. K.; Lee, J.; Maier, S. A.; Kim, M. S. Quantum plasmonics. *Nat. Phys.* **2013**, *9*, 329−340.

(174) Altewischer, E.; van Exter, M. P.; Woerdman, J. P. Plasmon-assisted transmission of entangled photons. *Nature* **2002**, *418*, 304−306.

(175) Fasel, S.; Robin, F.; Moreno, E.; Erni, D.; Gisin, N.; Zbinden, H. Energy-time entanglement preservation in plasmon-assisted light transmission. *Phys. Rev. Lett.* **2005**, *94*, 110501.

(176) Li, M.; Zou, C. L.; Ren, X. F.; Xiong, X.; Cai, Y. J.; Guo, G. P.; Tong, L. M.; Guo, G. C. Transmission of Photonic Quantum Polarization Entanglement in a Nanoscale Hybrid Plasmonic Waveguide. *Nano Lett.* **2015**, *15*, 2380−2384.

(177) Zhang, W. K.; Chen, Y. J.; Hu, C. L.; Zhang, Y. F.; Chen, X. D.; Zhang, M. Q. Effective excitation and control of guided surface plasmon polaritons in a conjugated polymer-silver nanowire composite system. *J. Mater. Chem. C* **2013**, *1*, 1265−1271.

(178) Huck, A.; Kumar, S.; Shakoor, A.; Andersen, U. L. Controlled Coupling of a Single Nitrogen-Vacancy Center to a Silver Nanowire. *Phys. Rev. Lett.* **2011**, *106*, 096801.

(179) Kumar, S.; Huck, A.; Chen, Y. T.; Andersen, U. L. Coupling of a single quantum emitter to end-to-end aligned silver nanowires. *Appl. Phys. Lett.* **2013**, *102*, 103106.

(180) Kumar, S.; Huck, A.; Andersen, U. L. Efficient Coupling of a Single Diamond Color Center to Propagating Plasmonic Gap Modes. *Nano Lett.* **2013**, *13*, 1221−1225.

(181) Ropp, C.; Cummins, Z.; Nah, S.; Fourkas, J. T.; Shapiro, B.; Waks, E. Nanoscale imaging and spontaneous emission control with a single nano-positioned quantum dot. *Nat. Commun.* **2013**, *4*, 1447.

(182) Ropp, C.; Cummins, Z.; Nah, S.; Fourkas, J. T.; Shapiro, B.; Waks, E. Nanoscale probing of image-dipole interactions in a metallic nanostructure. *Nat. Commun.* **2015**, *6*, 6558.

(183) Gruber, C.; Kusar, P.; Hohenau, A.; Krenn, J. R. Controlled addressing of quantum dots by nanowire plasmons. *Appl. Phys. Lett.* **2012**, *100*, 231102.

(184) Gruber, C.; Trugler, A.; Hohenau, A.; Hohenester, U.; Krenn, J. R. Spectral Modifications and Polarization Dependent Coupling in Tailored Assemblies of Quantum Dots and Plasmonic Nanowires. *Nano Lett.* **2013**, *13*, 4257−4262.

(185) Pfaff, W.; Vos, A.; Hanson, R. Top-down fabrication of plasmonic nanostructures for deterministic coupling to single quantum emitters. *J. Appl. Phys.* **2013**, *113*, 024310.

(186) Tran, T. T.; Fang, J. H.; Zhang, H.; Rath, P.; Bray, K.; Sandstrom, R. G.; Shimoni, O.; Toth, M.; Aharonovich, I. Facile Self-Assembly of Quantum Plasmonic Circuit Components. *Adv. Mater.* **2015**, *27*, 4048−4053.

(187) Liu, S. D.; Cheng, M. T.; Yang, Z. J.; Wang, Q. Q. Surface plasmon propagation in a pair of metal nanowires coupled to a nanosized optical emitter. *Opt. Lett.* **2008**, *33*, 851−853.

(188) Manjavacas, A.; García de Abajo, F. J. Robust Plasmon Waveguides in Strongly Interacting Nanowire Arrays. *Nano Lett.* **2009**, *9*, 1285−1289.

(189) Ren, J. J.; Gu, Y.; Zhao, D. X.; Zhang, F.; Zhang, T. C.; Gong, Q. H. Evanescent-Vacuum-Enhanced Photon-Exciton Coupling and Fluorescence Collection. *Phys. Rev. Lett.* **2017**, *118*, 073604.

(190) Russell, K. J.; Liu, T. L.; Cui, S. Y.; Hu, E. L. Large spontaneous emission enhancement in plasmonic nanocavities. *Nat. Photonics* **2012**, *6*, 459−462.

(191) Andrew, P.; Barnes, W. L. Energy transfer across a metal film mediated by surface plasmon polaritons. *Science* **2004**, *306*, 1002−1005.

(192) Zhou, Z. K.; Li, M.; Yang, Z. J.; Peng, X. N.; Su, X. R.; Zhang, Z. S.; Li, J. B.; Kim, N. C.; Yu, X. F.; Zhou, L.; et al. Plasmon-Mediated Radiative Energy Transfer across a Silver Nanowire Array via Resonant Transmission and Subwavelength Imaging. *ACS Nano* **2010**, *4*, 5003−5010.

(193) Kwon, M. K.; Kim, J. Y.; Kim, B. H.; Park, I. K.; Cho, C. Y.; Byeon, C. C.; Park, S. J. Surface-plasmon-enhanced light-emitting diodes. *Adv. Mater.* **2008**, *20*, 1253−1257.

(194) Berini, P.; De Leon, I. Surface plasmon-polariton amplifiers and lasers. *Nat. Photonics* **2012**, *6*, 16−24.

(195) Lu, Y. J.; Kim, J.; Chen, H. Y.; Wu, C. H.; Dabidian, N.; Sanders, C. E.; Wang, C. Y.; Lu, M. Y.; Li, B. H.; Qiu, X. G.; et al. Plasmonic Nanolaser Using Epitaxially Grown Silver Film. *Science* **2012**, *337*, 450−453.

(196) Liu, N.; Gocalinska, A.; Justice, J.; Gity, F.; Povey, I.; McCarthy, B.; Pemble, M.; Pelucchi, E.; Wei, H.; Silien, C.; et al. Lithographically Defined, Room Temperature Low Threshold Subwavelength Red-Emitting Hybrid Plasmonic Lasers. *Nano Lett.* **2016**, *16*, 7822−7828.

(197) Chang, D. E.; Sorensen, A. S.; Demler, E. A.; Lukin, M. D. A single-photon transistor using nanoscale surface plasmons. *Nat. Phys.* **2007**, *3*, 807−812.

(198) Kim, N. C.; Li, J. B.; Yang, Z. J.; Hao, Z. H.; Wang, Q. Q. Switching of a single propagating plasmon by two quantum dots system. *Appl. Phys. Lett.* **2010**, *97*, 061110.

(199) Chen, W.; Chen, G. Y.; Chen, Y. N. Coherent transport of nanowire surface plasmons coupled to quantum dots. *Opt. Express* **2010**, *18*, 10360−10368.

(200) Li, J. B.; He, M. D.; Wang, X. J.; Peng, X. F.; Chen, L. Q. Switching and Fano resonance via exciton-plasmon interaction. *Chin. Phys. B* **2014**, *23*, 067302.

(201) Cheng, M. T.; Song, Y. Y. Fano resonance analysis in a pair of semiconductor quantum dots coupling to a metal nanowire. *Opt. Lett.* **2012**, *37*, 978−980.

(202) Bouchet, D.; Lhuillier, E.; Ithurria, S.; Gulinatti, A.; Rech, I.; Carminati, R.; De Wilde, Y.; Krachmalnicoff, V. Correlated blinking of fluorescent emitters mediated by single plasmons. *Phys. Rev. A: At., Mol., Opt. Phys.* **2017**, *95*, 033828.

(203) Chen, G. Y.; Lambert, N.; Chou, C. H.; Chen, Y. N.; Nori, F. Surface plasmons in a metal nanowire coupled to colloidal quantum dots: Scattering properties and quantum entanglement. *Phys. Rev. B: Condens. Matter Mater. Phys.* **2011**, *84*, 045310.

(204) Chen, G. Y.; Chen, Y. N. Correspondence between entanglement and Fano resonance of surface plasmons. *Opt. Lett.* **2012**, *37*, 4023−4025.

(205) Gonzalez-Ballestero, C.; Garcia-Vidal, F. J.; Moreno, E. Non-Markovian effects in waveguide-mediated entanglement. *New J. Phys.* **2013**, *15*, 073015.

(206) Martín-Cano, D.; González-Tudela, A.; Martín-Moreno, L.; García-Vidal, F. J.; Tejedor, C.; Moreno, E. Dissipation-driven generation of two-qubit entanglement mediated by plasmonic waveguides. *Phys. Rev. B: Condens. Matter Mater. Phys.* **2011**, *84*, 235306.

(207) Zheng, H. X.; Baranger, H. U. Persistent Quantum Beats and Long-Distance Entanglement from Waveguide-Mediated Interactions. *Phys. Rev. Lett.* **2013**, *110*, 113601.

(208) González-Tudela, A.; Martín-Cano, D.; Moreno, E.; Martín-Moreno, L.; Tejedor, C.; García-Vidal, F. J. Entanglement of Two Qubits Mediated by One-Dimensional Plasmonic Waveguides. *Phys. Rev. Lett.* **2011**, *106*, 020501.

(209) Li, Q.; Wei, H.; Xu, H. X. Resolving Single Plasmons Generated by Multiquantum-Emitters on a Silver Nanowire. *Nano Lett.* **2014**, *14*, 3358−3363.

(210) Ozel, T.; Hernandez-Martinez, P. L.; Mutlugun, E.; Akin, O.; Nizamoglu, S.; Ozel, I. O.; Zhang, Q.; Xiong, Q. H.; Demir, H. V. Observation of Selective Plasmon-Exciton Coupling in Nonradiative Energy Transfer: Donor-Selective versus Acceptor-Selective Plexcitons. *Nano Lett.* **2013**, *13*, 3065−3072.

(211) Lunz, M.; Gerard, V. A.; Gun'ko, Y. K.; Lesnyak, V.; Gaponik, N.; Susha, A. S.; Rogach, A. L.; Bradley, A. L. Surface Plasmon Enhanced Energy Transfer between Donor and Acceptor CdTe Nanocrystal Quantum Dot Monolayers. *Nano Lett.* **2011**, *11*, 3341−3345.

(212) Zhang, X.; Marocico, C. A.; Lunz, M.; Gerard, V. A.; Gun'ko, Y. K.; Lesnyak, V.; Gaponik, N.; Susha, A. S.; Rogach, A. L.; Bradley, A. L. Experimental and Theoretical Investigation of the Distance Dependence of Localized Surface Plasmon Coupled Forster Resonance Energy Transfer. *ACS Nano* **2014**, *8*, 1273−1283.

(213) Martin-Cano, D.; Martin-Moreno, L.; Garcia-Vidal, F. J.; Moreno, E. Resonance Energy Transfer and Superradiance Mediated by Plasmonic Nanowaveguides. *Nano Lett.* **2010**, *10*, 3129−3134.

(214) Yu, Y. C.; Liu, J. M.; Jin, C. J.; Wang, X. H. Plasmon-mediated resonance energy transfer by metallic nanorods. *Nanoscale Res. Lett.* **2013**, *8*, 209.

(215) de Torres, J.; Ferrand, P.; Colas des Francs, G.; Wenger, J. Coupling Emitters and Silver Nanowires to Achieve Long-Range Plasmon-Mediated Fluorescence Energy Transfer. *ACS Nano* **2016**, *10*, 3968−3976.

(216) Li, Q.; Wei, H.; Xu, H. X. Remote excitation and remote detection of single quantum dot using propagating surface plasmons on silver nanowire. *Chin. Phys. B* **2014**, *23*, 097302.

(217) Su, L.; Lu, G.; Kenens, B.; Rocha, S.; Fron, E.; Yuan, H. F.; Chen, C.; Van Dorpe, P.; Roeffaers, M. B. J.; Mizuno, H.; et al. Visualization of molecular fluorescence point spread functions via remote excitation switching fluorescence microscopy. *Nat. Commun.* **2015**, *6*, 6287.

(218) Fang, Y. R.; Wei, H.; Hao, F.; Nordlander, P.; Xu, H. X. Remote-Excitation Surface-Enhanced Raman Scattering Using Propagating Ag Nanowire Plasmons. *Nano Lett.* **2009**, *9*, 2049−2053.

(219) Wei, H.; Hao, F.; Huang, Y. Z.; Wang, W. Z.; Nordlander, P.; Xu, H. X. Polarization dependence of surface-enhanced Raman scattering in gold nanoparticle-nanowire systems. *Nano Lett.* **2008**, *8*, 2497−2502.

(220) Hutchison, J. A.; Centeno, S. P.; Odaka, H.; Fukumura, H.; Hofkens, J.; Uji-i, H. Subdiffraction Limited, Remote Excitation of Surface Enhanced Raman Scattering. *Nano Lett.* **2009**, *9*, 995−1001.

(221) Dasgupta, A.; Singh, D.; Pavan Kumar, G. V. Dual-path remote-excitation surface enhanced Raman microscopy with plasmonic nanowire dimer. *Appl. Phys. Lett.* **2013**, *103*, 151114.

(222) Lee, S. J.; Moskovits, M. Remote Sensing by Plasmonic Transport. *J. Am. Chem. Soc.* **2012**, *134*, 11384−11387.

(223) Lu, G.; De Keersmaecker, H.; Su, L.; Kenens, B.; Rocha, S.; Fron, E.; Chen, C.; Van Dorpe, P.; Mizuno, H.; Hofkens, J.; et al. Live-Cell SERS Endoscopy Using Plasmonic Nanowire Waveguides. *Adv. Mater.* **2014**, *26*, 5124−5128.

(224) Oulton, R. F.; Sorger, V. J.; Zentgraf, T.; Ma, R. M.; Gladden, C.; Dai, L.; Bartal, G.; Zhang, X. Plasmon lasers at deep subwavelength scale. *Nature* **2009**, *461*, 629−632.

(225) Chou, Y. H.; Wu, Y. M.; Hong, K. B.; Chou, B. T.; Shih, J. H.; Chung, Y. C.; Chen, P. Y.; Lin, T. R.; Lin, C. C.; Lin, S. D.; et al. High-Operation-Temperature Plasmonic Nanolasers on Single-Crystalline Aluminum. *Nano Lett.* **2016**, *16*, 3179−3186.

(226) Zhang, Q.; Li, G. Y.; Liu, X. F.; Qian, F.; Li, Y.; Sum, T. C.; Lieber, C. M.; Xiong, Q. H. A room temperature low-threshold ultraviolet plasmonic nanolaser. *Nat. Commun.* **2014**, *5*, 4953.

(227) Costantini, D.; Greusard, L.; Bousseksou, A.; De Wilde, Y.; Habert, B.; Marquier, F.; Greffet, J. J.; Lelarge, F.; Decobert, J.; Duan, G. H.; et al. A hybrid plasmonic semiconductor laser. *Appl. Phys. Lett.* **2013**, *102*, 101106.

(228) Alam, M. Z.; Aitchison, J. S.; Mojahedi, M. Theoretical Analysis of Hybrid Plasmonic Waveguide. *IEEE J. Sel. Top. Quantum Electron.* **2013**, *19*, 4602008.

(229) Sorger, V. J.; Ye, Z.; Oulton, R. F.; Wang, Y.; Bartal, G.; Yin, X.; Zhang, X. Experimental demonstration of low-loss optical waveguiding at deep sub-wavelength scales. *Nat. Commun.* **2011**, *2*, 331.

(230) Fedyanin, D. Y.; Yakubovsky, D. I.; Kirtaev, R. V.; Volkov, V. S. Ultralow-Loss CMOS Copper Plasmonic Waveguides. *Nano Lett.* **2016**, *16*, 362−366.

(231) He, X. Y.; Wang, Q. J.; Yu, S. F. Numerical Study of Gain-Assisted Terahertz Hybrid Plasmonic Waveguide. *Plasmonics* **2012**, *7*, 571−577.

(232) Sorger, V. J.; Pholchai, N.; Cubukcu, E.; Oulton, R. F.; Kolchin, P.; Borschel, C.; Gnauck, M.; Ronning, C.; Zhang, X. Strongly Enhanced Molecular Fluorescence inside a Nanoscale Waveguide Gap. *Nano Lett.* **2011**, *11*, 4907−4911.

(233) Lu, F. F.; Li, T.; Hu, X. P.; Cheng, Q. Q.; Zhu, S. N.; Zhu, Y. Y. Efficient second-harmonic generation in nonlinear plasmonic waveguide. *Opt. Lett.* **2011**, *36*, 3371−3373.

(234) Yang, X. D.; Liu, Y. M.; Oulton, R. F.; Yin, X. B.; Zhang, X. Optical Forces in Hybrid Plasmonic Waveguides. *Nano Lett.* **2011**, *11*, 321−328.

(235) Song, Y.; Wang, J.; Li, Q. A.; Yan, M.; Qiu, M. Broadband coupler between silicon waveguide and hybrid plasmonic waveguide. *Opt. Express* **2010**, *18*, 13173−13179.

(236) Hu, T.; Qiu, H. D.; Zhang, Z. C.; Guo, X.; Liu, C. Y.; Rouifed, M. S.; Littlejohns, C. G.; Reed, G. T.; Wang, H. A Compact Ultrabroadband Polarization Beam Splitter Utilizing a Hybrid Plasmonic Y-Branch. *IEEE Photonics J.* **2016**, *8*, 4802209.

(237) Lou, F.; Dai, D. X.; Wosinski, L. Ultracompact polarization beam splitter based on a dielectric-hybrid plasmonic-dielectric coupler. *Opt. Lett.* **2012**, *37*, 3372−3374.

(238) Lu, C. C.; Hu, X. Y.; Yue, S.; Fu, Y. L.; Yang, H.; Gong, Q. H. Ferroelectric Hybrid Plasmonic Waveguide for All-Optical Logic Gate Applications. *Plasmonics* **2013**, *8*, 749−754.

(239) Gao, L. F.; Huo, Y. J.; Zang, K.; Paik, S.; Chen, Y. S.; Harris, J. S.; Zhou, Z. P. On-chip plasmonic waveguide optical waveplate. *Sci. Rep.* **2015**, *5*, 15794.

(240) Alam, M. Z.; Aitchison, J. S.; Mojahedi, M. A marriage of convenience: Hybridization of surface plasmon and dielectric waveguide modes. *Laser Photonics Rev.* **2014**, *8*, 394−408.

(241) Oulton, R. F. Surface plasmon lasers: sources of nanoscopic light. *Mater. Today* **2012**, *15*, 26−34.

(242) Gwo, S.; Shih, C. K. Semiconductor plasmonic nanolasers: current status and perspectives. *Rep. Prog. Phys.* **2016**, *79*, 086501.

(243) Avrutsky, I. Surface plasmons at nanoscale relief gratings between a metal and a dielectric medium with optical gain. *Phys. Rev. B: Condens. Matter Mater. Phys.* **2004**, *70*, 155416.

(244) Lakhani, A. M.; Kim, M. K.; Lau, E. K.; Wu, M. C. Plasmonic crystal defect nanolaser. *Opt. Express* **2011**, *19*, 18237−18245.

(245) Wu, C. Y.; Kuo, C. T.; Wang, C. Y.; He, C. L.; Lin, M. H.; Ahn, H.; Gwo, S. Plasmonic Green Nanolaser Based on a Metal-Oxide-Semiconductor Structure. *Nano Lett.* **2011**, *11*, 4256−4260.

(246) Lu, Y. J.; Wang, C. Y.; Kim, J.; Chen, H. Y.; Lu, M. Y.; Chen, Y. C.; Chang, W. H.; Chen, L. J.; Stockman, M. I.; Shih, C. K.; et al. All-Color Plasmonic Nanolasers with Ultralow Thresholds: Autotuning Mechanism for Single-Mode Lasing. *Nano Lett.* **2014**, *14*, 4381−4388.

(247) Sidiropoulos, T. P. H.; Roder, R.; Geburt, S.; Hess, O.; Maier, S. A.; Ronning, C.; Oulton, R. F. Ultrafast plasmonic nanowire lasers near the surface plasmon frequency. *Nat. Phys.* **2014**, *10*, 870−876.

(248) Huang, Z. X.; Koschny, T.; Soukoulis, C. M. Theory of Pump-Probe Experiments of Metallic Metamaterials Coupled to a Gain Medium. *Phys. Rev. Lett.* **2012**, *108*, 187402.

(249) Hua, J. J.; Wu, F.; Xu, Z. F.; Wang, W. H. Influence of symmetry breaking degrees on surface plasmon polaritons propagation in branched silver nanowire waveguides. *Sci. Rep.* **2016**, *6*, 34418.

(250) Li, Z. P.; Zhang, S. P.; Halas, N. J.; Nordlander, P.; Xu, H. X. Coherent Modulation of Propagating Plasmons in Silver-Nanowire-Based Structures. *Small* **2011**, *7*, 593−596.

(251) Pan, D.; Wei, H.; Xu, H. X. Optical interferometric logic gates based on metal slot waveguide network realizing whole fundamental logic operations. *Opt. Express* **2013**, *21*, 9556−9562.

(252) Yan, R. X.; Pausauskie, P.; Huang, J. X.; Yang, P. D. Direct photonic-plasmonic coupling and routing in single nanowires. *Proc. Natl. Acad. Sci. U. S. A.* **2009**, *106*, 21045−21050.

(253) Wu, X. Q.; Xiao, Y.; Meng, C.; Zhang, X. N.; Yu, S. L.; Wang, Y. P.; Yang, C. X.; Guo, X.; Ning, C. Z.; Tong, L. M. Hybrid Photon-Plasmon Nanowire Lasers. *Nano Lett.* **2013**, *13*, 5654−5659.